Technische Universität München
Physik Department
Lehrstuhl für Oberflächen- und Grenzflächenphysik E20

Dissertation

Single-Molecule-Junction Raman Spectroscopy on Distinct Metal-Molecule-Metal Systems

Peter Emanuel Hasch

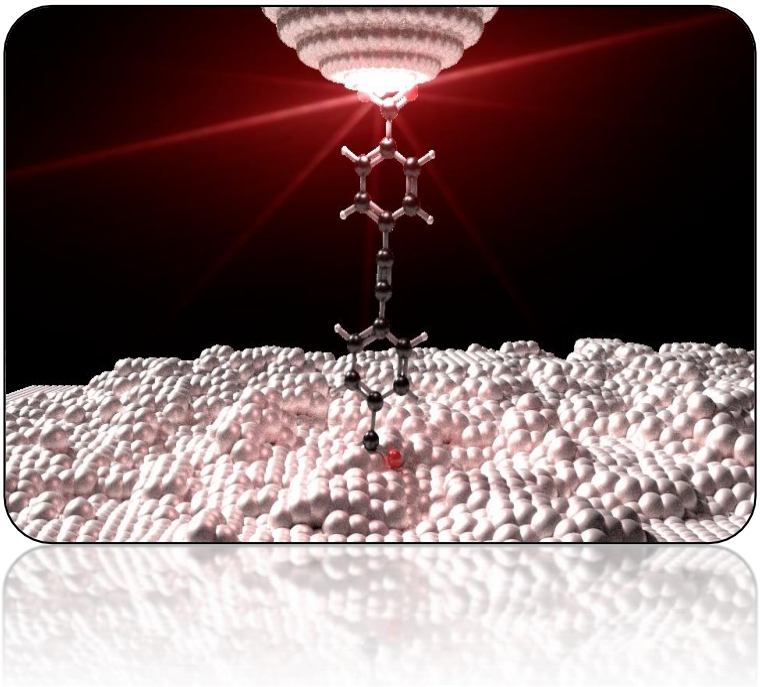

9st of November 2017

Technische Universität München
Physik Department E20
Molecular Nanosciece and Chemical Physics of Interfaces

Single-Molecule Junction Raman Spectroscopy on Distinct Metal-Molecule-Metal Systems

Peter Emanuel Hasch

Vollständiger Abdruck der von der Fakultät Physik der Technischen Universität München zur Erlangung des akademischen Grades des Doktors der Naturwissenschaften (Dr. rer. nat.) genehmigten Dissertation

Vorsitzender: Prof. Dr. Martin Zacharias

Prüfende der Dissertation:

1. Prof. Dr. Johannes Barth
2. Prof. Dr. Alexander Holleitner

Die Dissertation wurde am 24.10.2017 bei der Technischen Universität München eingereicht und durch die Fakultät für Physik am 09.11.2017 angenommen.

Abstract

The understanding of electron transport through individual molecule species is fundamental in the field of molecular electronics. For example, molecular rectifiers, transistors, switches and amplifiers have been demonstrated. Herein the reliable control of electron transfer rates and loss mechanisms is highly important. In most cases, however, the detected parameter set is limited to the current-voltage (I-V) characteristic of single-molecule junctions.

This thesis reports the combination of vibrational and electrical spectroscopy, employing a molecule junction spectroscopy (MJS) technique. For this purpose, a tetrahedral metal-coated glass tip was used as apertureless nearfield optics for Raman spectroscopy and simultaneously as counter electrode to a surface-anchored molecule. This allows recording Raman spectra concomitantly with the junction current as a function of the applied bias voltage.
The first large part of this thesis was rebuilding and improving the MJS setup. Thereby, a higher stability, a significantly lower base pressure as well as a lower electric noise level was achieved. The optical investigation methods were upgraded by designing and implementing powerful routines. All experimental routines were implemented in LabVIEW.

First, the feasibility of investigating a single-molecule at temperatures down to 77 K, using a gold-molecule-gold configuration, was demonstrated. Then the strain-induced change of the vibrational spectrum of a dithiol helicene molecule was investigated, revealing a red shift of the vibrational energy of a certain mode with increasing mechanical stress on the molecule. Finally, a ferromagnet-molecule-ferromagnet geometry was employed to observe the influence of the magnetic properties of the leads. These experiments show a negative differential conductance at a certain threshold voltage, which was accompanied by a change of the Raman signal. This effect was only observed in ferromagnetic junctions and could be explained by the formation of a spin valve.

Zusammenfassung

Das Verständnis des Elektronentransportes durch Einzelmolekülkontakte ist einer der grundlegenden Pfeiler der molekularen Elektronik. Die eingesetzten Moleküle fungieren hierbei zum Beispiel als Diode, Schalter, Verstärker oder als Transistor. Das zuverlässige Steuern und Kontrollieren des Elektronentransfers, sowie das Verstehen von Verlustmechanismen ist hierfür wesentlich. Meistens ist der aufgenommene Parameterraum jedoch auf die Strom-Spannungs-Kennlinien der einzelnen Moleküle begrenzt.

Im Zuge dieser Arbeit wird eine Messmethode (Moleculear Junction Spectroscopy, MJS), welche die elektrische Spektroskopie mit Ramanspektroskopie (Vibrationsspektroskopie) vereint, verwendet. Zu diesem Zweck wird eine metallbedampfte tetraedrische Glasspitze als aperturlose Nahfeldoptik sowie als zweite Elektrode um die Moleküle zu kontaktieren, genutzt. Dadurch ist es möglich, gleichzeitig Ramanspektren und den Strom in Abhängigkeit von der angelegten Spannung am Molekül zu messen.
Das verwendete MJS Setup wurde zu diesem Zwecke neu aufgebaut und runderneuert. Dabei konnte eine signifikant erhöhte mechanische Stabilität, ein wesentlich verringertes elektrisches Rauschniveau sowie ein besserer Basisdruck erzielt werden. Weiterhin wurde die Software des Systems komplett auf LabVIEW umgestellt, wobei viele neu entwickelte Routinen das Akquirieren von Messdaten wesentlich erleichterten.

Im ersten Schritt wurde gezeigt, dass die MJS Methode in der Lage ist, einzelne Moleküle bis zu Temperaturen von 77 K zu untersuchen. Die dafür genutzte Konfiguration bestand aus einer mit Gold beschichteten Nahfeldspitze und geeigneten Molekülen, welche auf einem Goldsubstrat aufgebracht wurden.
Weiterhin wurde der Einfluss von mechanischer Verspannung auf die Frequenzen der intramolekularen Schwingungen untersucht. Es wurde das chirale Molekül 7-Helizen-Dithiol verwendet. Hierbei konnte eine Verringerung der Schwingungsenergie mit zunehmender Verspannung beobachtet werden.

Der letzte Bereich befasst sich mit den Beobachtungen an Nickel-Molekül-Nickel Heterostrukturen. In dieser Konfiguration wurde der Effekt der negativen differentiellen Leitfähigkeit beobachtet. Dieser trat bei einer definierten Schwellenspannung auf, einhergehend mit einer Änderung im Ramanspektrum. Um den Einfluss der ferromagnetischen Elektroden zu untersuchen wurden diese durch Silberelektroden ersetzt, womit auch die negative differentielle Leitfähigkeit verschwand. Somit kann gefolgert werden, dass dieser Effekt auf den magnetischen Einfluss der Elektroden zurückgeht und könnte durch die spannungsinduzierte Bildung einer Spin-Ventil Konfiguration erklärt werden.

Contents

CHAPTER 1

Introduction

The research on the miniaturization of electronic circuits has been an ongoing effort for several decades. The invention of the transistor [1] was the first large step in scaling down logic operations, followed by the development of integrated circuitry [2]. Over time, the size of circuits was reduced by developing smaller device elements. Today state of the art of standard semiconductor structures is a feature size of 10 nm or below [3, 4]. Further decrease of the structure size implies the occurrence of quantum effects. Therefore, the controllability of the fabrication as well as the electronic properties of the devices becomes more challenging.

Another approach to build active devices with nanometer size is to employ single molecules as functional parts. Following this route, the electrical and optical properties of molecules can be exploited to construct single-molecule transistors [5–9], single-molecule switches [10–14], single-molecule amplifiers [15, 16], single-molecule logics [17–21] and single-molecule rectifiers [22–25].
Metal-molecule-metal heterostructure junctions are used to realize these devices. Addressing, manipulating and reading single charge states or single spin states on the molecule in the junction opens up the ability to perform logical operations. Molecular electronics is a promising candidate to build electronic devices, being faster and cheaper than conventional logic circuits. On top of that, single-molecule electronic devices represent the ultimate limit of miniaturization.

The crucial factor to realize molecular electronics is the understanding of charge transport [22, 26, 27] as well as the dissipation of energy in a junction [28–30]. The systematic investigation of charge transport necessitates the understanding of charged states of molecules, electron-electron scattering as well as the electronic coupling with vibrational states. The challenges

in this field attracted massive research efforts. Consequently, many theories [31–40] were developed and experiments [10–14, 17–19, 22–25, 41–45] have been performed.

The commonly used characterization methods are limited to either electrical or optical spectroscopy of single molecules. A possibility to refine the measurement method as well as gaining more detailed information is offered by the hybrid approach. By combining complementary methods (optical and electrical) a multitechnique was developed [46, 47], allowing the simultaneous acquisition of a wide parameter range. Optical spectroscopy is employed to acquire vibrational properties of single-molecule junctions [43].

The used setup allows for transport characterization and vibrational spectroscopy of a single molecule at the same time. This enables us to acquire a parameter set for a single-molecule junction, which can be influenced electrically (voltage) or mechanically (stress).
The following chapters will introduce the fundamentals about single-molecule junctions, Raman spectroscopy and the sample preparation. Afterwards, the home-built setup and the experimental investigation procedures will be described in detail.

Chapter 4.1 demonstrates the acquisition of a single molecule at low temperatures, using two different geometries. The next part reveals the stress-induced shifting of vibrational modes of a 7-helicene molecule (4.2). As last part, the influence of ferromagnetic electrodes on the DHE molecule was examined (4.3). A negative differential conductance at a certain voltage in case of using ferromagnetic electrodes was observed.
In Conclusion, the findings of the thesis will be summarized (5).

The data shown in this thesis are partially contained in several publications. The voltage dependent switching at low temperatures contribute to the publication: *Voltage-Driven Conformational Switching in a Single-Molecule Junction*, which is submitted to JACS [48]. The second publication is ready for submission to Review of Scientific Instruments and is named *Single Molecules in Strong Optical Fields: A Variable Temperature Molecular Junction Spectroscopy Set-Up*, containing basics about the setup as well as benchmark measurements [49]. The data about the NDC device are the basis for a publication, which is in preparation: *Negative Differential Conductance in Single-Molecule Junctions with Ferromagnetic Electrodes* [50]. The results of the stretching of helicene molecules will be presented in a further publication [51].

CHAPTER 2

Theoretical and Experimental Foundations

The following chapter gives an overview of the used techniques and the involved mechanisms, including brief theoretical explanations on electron transport in junctions as well as Raman spectroscopy.

2.1. Single-Molecule Junctions

In order to systematically investigate and understand the charge transport in nanoscale devices, being important for many applications, it is necessary to control and probe the current through a single-molecule.
In the last decades, single-molecule-devices have been investigated in a variety of different geometries [25, 30, 52, 53], mostly in order to determine the electric and conductive behavior.

The concept of investigating single-molecules is depicted in Figure 2.1a. The molecule of interest, frequently an organic species is anchored to the metal electrodes by terminal groups on both sides, which are in our case thiols [54–60] or carboxyls [58–62]. These anchor groups favor a covalent and symmetric coupling of the molecule to both electrodes. It is possible to apply a voltage across the electrodes and record the current through the molecule simultaneously.

The most common methods to achieve single-molecule junctions can be separated into two main strategies, the on-chip techniques and the scanning probe microscopy approach. The on-chip molecule junction approach incorporates all techniques, which form the junction on-

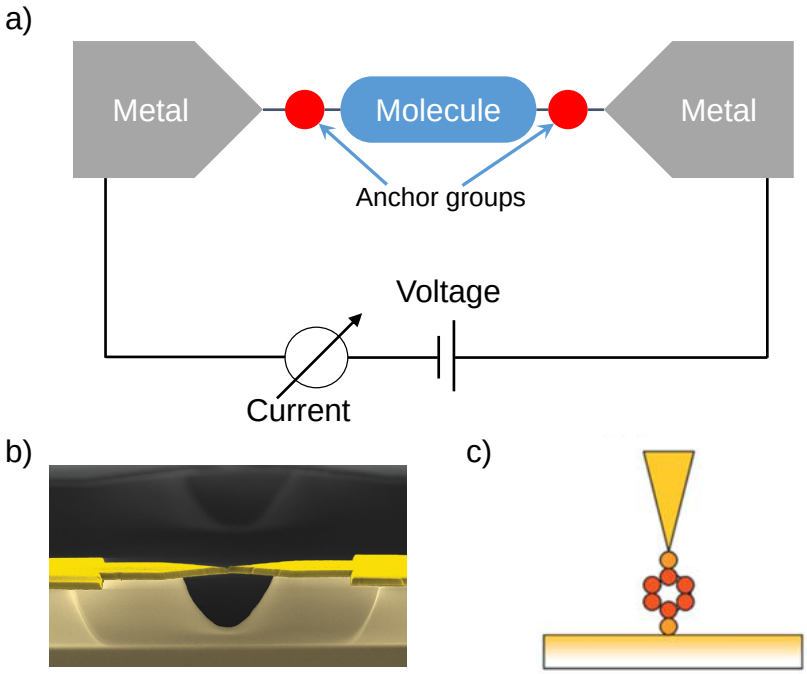

Figure 2.1.: Techniques to realize single-molecule junctions. a) illustrates the concept of measurement for single-molecule junctions. b) and c) depict two exemplary geometries, experimentally realizing single-molecule junctions. Adopted from [63, 64].

chip but without the possibility to vary or adjust the electrode distance during the experiment [41, 65, 66], e.g. electro migration technique [67–69]. The off-chip approach is represented by the techniques shown in Figure 2.1b and c. The sketch in Figure 2.1b illustrates a mechanically controlled break junction (MCBJ). A metallic wire becomes mechanically stressed, until it opens up a small gap. The molecules are deposited in this gap and may form a covalently bound bridge between the electrodes [57, 70–73]. Figure 2.1c describes the scanning probe microscopy method to build a single-molecule junction. Here, a (sub-)monolayer of molecules is deposited on a substrate. The yellow triangle represents a scanning probe tip, which is used as counter electrode, in order to form the junction [54, 74–78]. In this approach, the junction formation is a spontaneous random process.

Electron transport through a single-molecule cannot be described by the Drude model [79]. Currently, there are several different models to describe the transport through a single-molecule junction, which strongly depends on the contact to the leads as well as the bridging molecule itself [26, 33, 78].
First, we have to consider what happens, when the length L of the conductor is smaller than the scatter length of electrons in the conductor. At this point the electron transport is ballistic. If the conduction channel is smaller (width W) than the wavelength of the electrons at the Fermi niveau of the electrodes a one-dimensional conduction channel is formed and quantum effects occur (cf. [80–82]). The transport through a one-dimensional conductor is also described by ballistic electron transport. A transport channel with width W and length

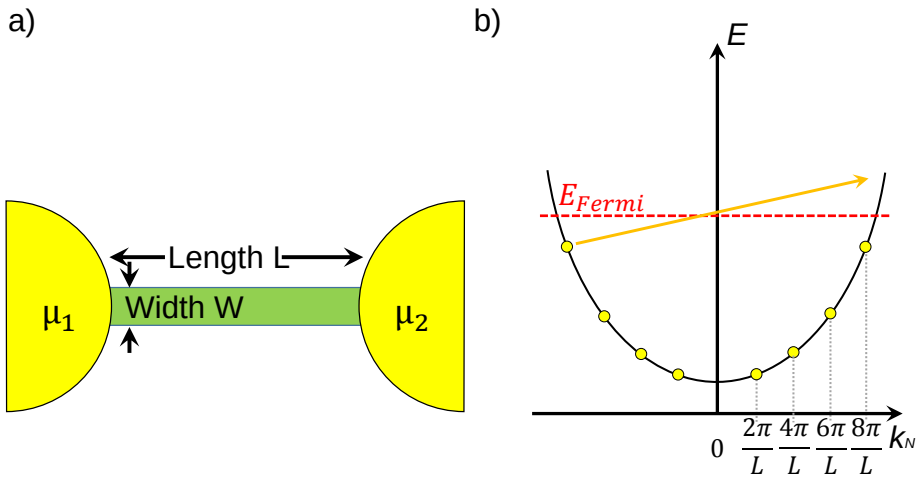

Figure 2.2.: Ballistic transport mechanism. a) illustrates the ballistic transport through a channel with a length L and a width W. b) shows the quadratic dispersion of a one-dimensional conductor.

L between two electrodes is depicted in Figure 2.2a. The current through this channel is given by:

$$I = envv \tag{2.1}$$

Here, I represents the current through the channel, e is the electron charge. The number of flowing electrons is represented by n in equation 2.1. Here, a one-dimensional conductor with a quadratic dispersion is considered [83, 84], where N electrons are filled up to the Fermi level. The number of electrons n, contributing to the current can be calculated by counting the electrons, which are redistributed from below to above the Fermi level, as illustrated by the green arrow in Figure 2.2b. The last item of equation 2.1 is v, standing for the group velocity of the electrons.
The number of electrons n can be expressed by $n{=}\frac{1}{L}\sum_k$ as sum over all contributing electrons. Consequently, the current is calculated to:

$$I = \frac{e}{L}\sum_k v[f_{\mu_1}(E) - f_{\mu_2}(E)] \tag{2.2}$$

$f_{\mu_{1,2}}\ (E)$ is the Fermi distribution of the two electrodes. Considering an infinite length L of the conduction channel, the group velocity can be replaced by the dispersion relation $v{=}\frac{1}{\hbar}\frac{\partial E}{\partial k}$, which allows the change from the sum over the k vectors of the electrons to an integral over dk.

$$\begin{aligned} I = \frac{e}{L}\sum_k \frac{1}{\hbar}\frac{\partial E}{\partial k}[f_{\mu_1}(E) - f_{\mu_2}(E)] = \frac{e}{L}\int \frac{1}{\hbar}\frac{\partial E}{\partial k}[f_{\mu_1}(E) - f_{\mu_2}(E)]dk = \\ = \frac{e}{L}\frac{L}{2\pi\hbar}2\int [f_{\mu_1}(E) - f_{\mu_2}(E)]dE \end{aligned} \tag{2.3}$$

At a temperature of 0 K is the integral of the difference of f_{μ_1} *(E)* - f_{μ_2} *(E)* the difference of the electrochemical potential μ_1 - μ_2. Consequently, the current is expressed by:

$$I = \frac{2e}{h}(\mu_1 - \mu_2) = \frac{2e}{h} e \frac{(\mu_1 - \mu_2)}{e} = \frac{2e^2}{h} U \tag{2.4}$$

This leads to the conductance quantum G_0 of a one-dimensional conductor, which is independent of the length L:

$$G_0 = \frac{I}{U} = \frac{2e^2}{h} = \frac{1}{12.9}(\mathrm{k\Omega})^{-1} \tag{2.5}$$

In case of more than one contributing eigenchannel, the total conductance is expressed by:

$$G_{tot} = G_0 \sum_{i=1}^{n} T_i \tag{2.6}$$

In equation 2.6, T_i represents the transmission probability of the eigenchannel i between the electrodes. A metal-metal point contact is a ballistic conductor, where conductance quantization is often observed [85]. The formation of such a mechanically highly fragile point contact is shown later, in order to test the stability of the setup (cf. 3.2). Ballistic transport is the fundamental base for most transport models at nanoscale.

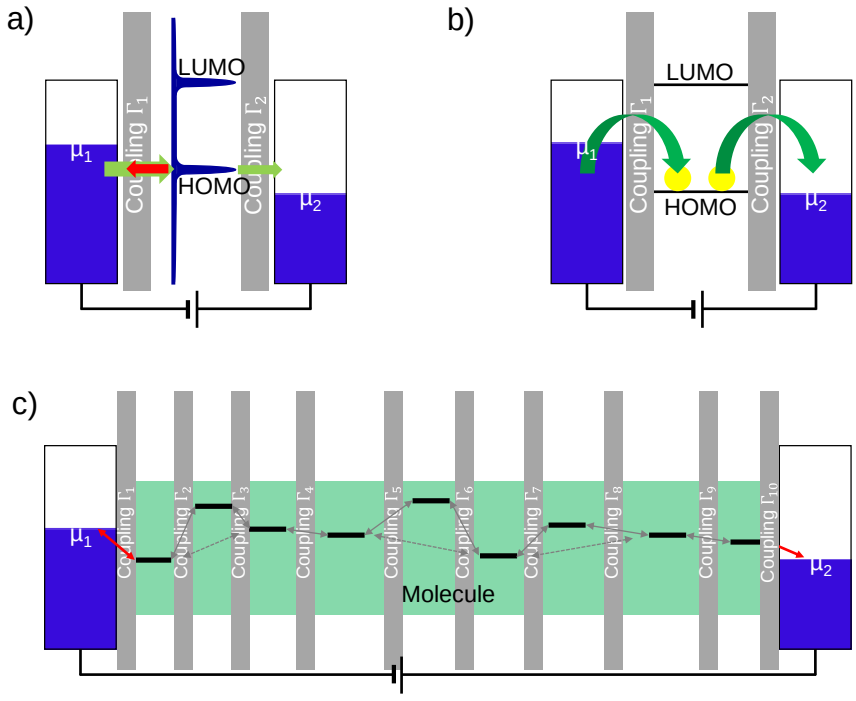

Figure 2.3.: Different transport models. a) sketches the coherent transport. b) shows hopping through the HOMO of the molecule. c) depicts the process of sequential hoping.

Three different transport regimes are distinguished here, the coherent transport regime, the hopping as well as the coulomb blockade regime. The parameters, deciding which model describes the system best are the coupling strength Γ between the electrodes and the molecule,

the size of the HOMO (Highest Occupied Molecular Orbital) - LUMO (Lowest Unoccupied Molecular Orbital) gap Δ as well as the Coulomb energy E_C. $E_C = \frac{e^2}{2C}$ is the energy needed to charge the molecule, where C is the capacity of the molecule [33, 86].
The mechanism of coherent transport can be described as a scattering mechanism. Here, the phase of the electron is conserved, which means the scattering process is coherent.
The scheme for coherent transport is sketched in Figure 2.3a. This regime is often observed if the coupling strength Γ is larger than E_C but smaller than Δ. A large Γ causes that the transmission time of the electron passing through the junction is smaller than the time needed to interact with other electrons. The transport through the junction can be described by elastic scattering of the electrons on the molecular density of states [70, 71, 87]. Figure 2.3a sketches the elastic scattering of electrons passing the junction from the left electrode to the right one. The green arrows illustrate the transmitted electrons, whereas the red arrow represents the back scattered electrons. In case of a symmetrically coupled molecule (Γ_1 equal to Γ_2), the resistance is inversion symmetric, resulting in symmetric current-voltage characteristics [70, 88]. The transport is described by the so-called generalized Landauer formalism:

$$I = \frac{e}{\pi\hbar} \int T(E)[f_{\mu_1}(E) - f_{\mu_2}(E)]dE \tag{2.7}$$

Equation 2.7 bases on the Landauer formalism (equation 2.3) but introduces the energy dependent transmission probability *T(E)*, which is related to the molecular density of states.

The second transport regime is called hopping. The dominant time constants of hopping are larger, resulting in a dephasing of the electron. Consequently, this transport regime is not coherent. The model of hopping can be observed if Γ is smaller than E_C and Δ but E_C is smaller than Δ [89]. This happens in the case of a large HOMO-LUMO gap and/or a weak coupling to the electrodes. The process of hopping is depicted in Figure 2.3b. The electrons are hopping on and off the HOMO, but the residence time of an electron or hole on the molecule is larger than the de- or repopulation time. In this case, the electrons need to tunnel on and off the molecule through a barrier.
The sequential hopping represents a special case of the hopping regime, having spatially distributed energy levels, in a junction. The molecule can be modeled by n locally separated states, as sketched in Figure 2.3c. Here, the electrons need to tunnel between the spatially distributed local states by overcoming a tunneling barrier. This incoherent process can be thermally activated and the conductance strongly depends on the number of states and therefore on the length of the molecule [90]. The conductance of a system of n spatially separated states decreases exponentially with the number of the states, accompanied by an increase of the electron transfer time, as tunneling between the increasingly separated localized states is suppressed [91]. The transport through non-conjugated electron systems, e.g. C-C σ-bonds, is often described by this model [92].

The Coulomb blockade regime is reached if the Coulomb energy E_C is much larger than the gap Δ of the molecule and the coupling Γ to the electrodes [33]. This model again describes the transport mechanism of hopping. The energy needed to add or remove an electron from

the molecule is large with respect to the other parameters, resulting in the occurrence of quantum effects, like coulomb staircases [93].

Figure 2.4 illustrates the idealized current-voltage characteristics (red curve), in case of a symmetrically anchored molecule. The transport behavior looks similar for the coherent as well as the hopping transport regime. The arising steps at voltage of ± 0.6 stem from the current contribution of a molecular orbital, being aligned with one of the electrode levels. The corresponding differential conductance (dI/dU) reveals a peak at each of the current steps.

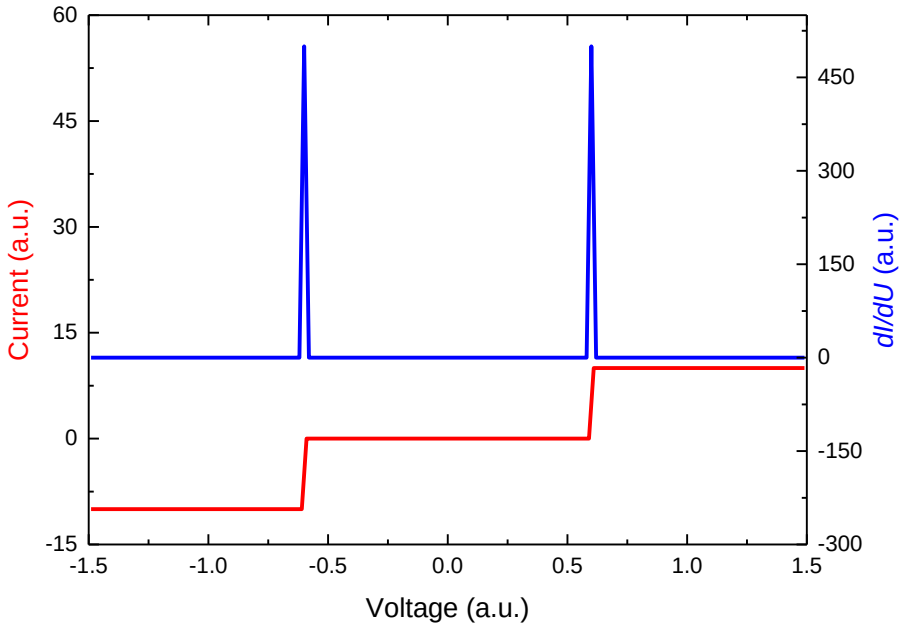

Figure 2.4.: Idealized current-voltage curve for the coherent or hopping transport model (red). The differential conductance is depicted in blue.

In case of the thiol-anchored molecules on gold electrodes, the molecule is strongly coupled to the leads. Consequently, the coherent transport model was reported to be the most accurate one [33]. The data acquired on single-molecule junctions in this thesis shows charged states of the molecules (see chapter 4). The occurrence of discrete charge states, which are hard to explain with coherent transport, indicate that our investigated systems are rather located in the hopping regime or a mix between the coherent transport and the hopping regime.

2.2. Raman Spectroscopy

The mechanism of Raman scattering is exploited in the presented investigations, using the opto-electrical molecular junction spectroscopy setup and will be described in the following. In 1928, the phenomenon of Raman scattering was reported for the first time [95]. It turned out

to be one of the most powerful tools to investigate vibrational modes of a (molecular) system. It can be exploited to determine the chemical structure, nature of bonds, intramolecular vibrations and electronic states [96].
The Raman intensity I of a vibrational mode can be expressed by:

$$I = K\alpha^2 P\omega^4 \tag{2.8}$$

Here, α is the polarizability tensor of the molecule, K consist of constants, e.g. the speed of light. The remaining two variables are the ones that can be influenced by the experimental setup, such as P (power) and the excitation frequency of the laser ω [96]. From equation 2.8, it can be recognized that only vibrational modes, which reveal a polarizability can observed by Raman spectroscopy. Additionally, the intramolecular atomic movement of a Raman active mode needs to be symmetric with respect to a center point (Raman selection rules) [96].

A complementary method, investigating the chemical and vibrational properties of matter is infrared absorption spectroscopy, which depends on the oscillating dipole moment of a vibrational mode [97]. Additionally, the intramolecular movement of an infrared active vibration needs to be asymmetric with respect to a center point [98]. This necessitates that vibrations are either observable by Raman spectroscopy or infrared spectroscopy [99].

By illuminating matter with coherent light, several scattering mechanisms occur. Either the light is elastically scattered, absorbed or inelastically scattered. Raman scattering is inelastic scattering with vibrational excitations in the matter.
The scattering process is described by the absorption of an incident photon, exciting the molecule to a virtual state, which decays with a short lifetime irradiating a secondary photon. As depicted in Figure 2.5 on the left side, the excited virtual state can decay directly to the initial state, named Rayleigh scattering. In this case, the secondary photon has the same energy as the incident one. The second process (Raman scattering) is shown in the center and at the right side of Figure 2.5. The excited virtual state decays in a radiative way to a different state than the initial one. In this particular case, the emitted photon reveals a wavelength λ, which is different from the one of the incident photon λ_0. The energy difference $\Delta\omega$ between the incident and secondary photon is the energy of the vibrational mode and can be calculated to:

$$\Delta\omega = {\lambda_0}^{-1} - \lambda^{-1} \tag{2.9}$$

$\Delta\omega$ is typically expressed in the inverse of wavelength, called wavenumbers (cm^{-1}). As indicated by the red and blue arrows in Figure 2.5, the virtual state can decay to different states, which means that the Raman scattered light consist of several discrete spectral lines, having different energy shifts $\Delta\omega$. These energies are characteristic for the vibrational modes. $\Delta\omega$ is the vibrational energy of this particular intramolecular vibration.
The Rayleigh scattering case reveals an energy shift of $\Delta\omega = 0\ cm^{-1}$. In this case, no information about the investigated matter is acquired. The cases of $\Delta\omega \neq 0\ cm^{-1}$ are called Raman scattering.
Raman scattering is divided into two segments. The first one is called Stokes scattering, where the incident photon has a higher energy than the secondary one ($\Delta\omega > 0\ cm^{-1}$). The second

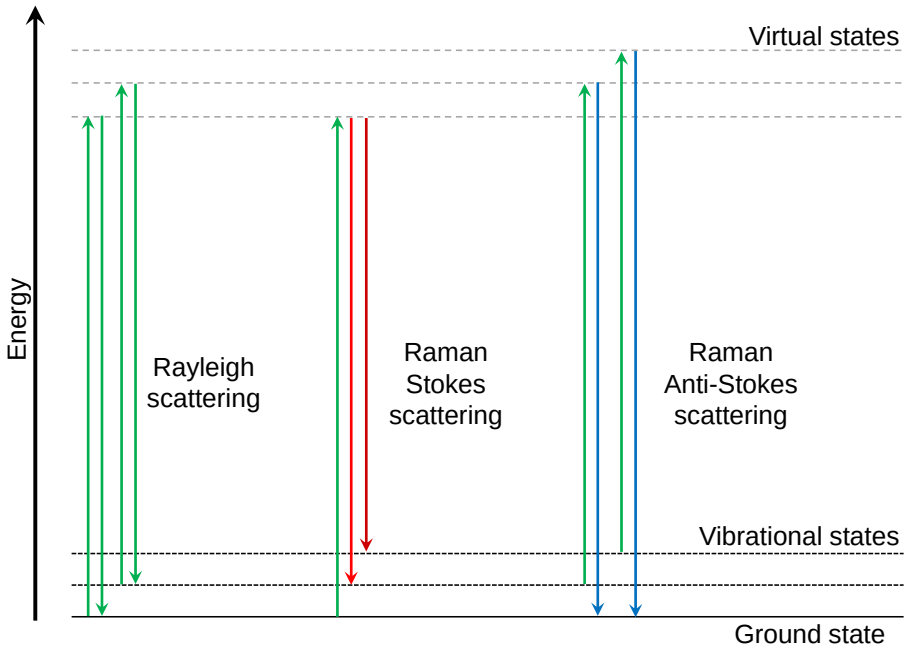

Figure 2.5.: Energy level diagram for Raleigh, Raman Stokes and Raman anti-Stokes scattering (cf. [96]).

case is the Anti-Stokes scattering, as depicted at the right side of Figure 2.5. Here, the incident photon interacts with an already excited state to a virtual one, which decays by irradiating a photon, having more energy, than the primary one ($\Delta\omega < 0$ cm^{-1}), indicated by the blue arrows in Figure 2.5.

Due to the very small Raman cross section in single-molecules ($\sim 10^{-29}$ cm^2) [96, 98, 100] and the diffraction limited optical spot size, techniques to increase the Raman intensity need to be employed to achieve a sensitivity, which allows for the investigation of single-molecules.

The first time, single-molecule Raman spectroscopy was reported in the last two decades [101–103]. The main difficulty in investigating single-molecules is the small Raman cross section. Consequently, a technique enhancing the Raman intensity needs to be employed. In the following, the plasmonic properties as well as effects are required for the technique of enhanced Raman spectroscopy.

Surface plasmons (SPs) are assigned to collective movements of electrons at the interface between a dielectric or vacuum and a conductive metal, as depicted in the inset of Figure 2.6 [104]. The coupling of a photon to surface plasmons results in a quasiparticle, called Surface Plasmon Polariton (SPP). Due to the non-linear dielectric function of metals, the dispersion relation of SPs is highly non-linear. As depicted in Figure 2.6, the dispersion of light in vacuum (red line) and the plasmonic dispersion (blue line) have no crossing point. Due to the k-vector mismatch between light in vacuum and SPs, it is highly inefficient to couple photons to SPs. On the other hand, a photon traveling through a high refractive index material, e.g. glass or

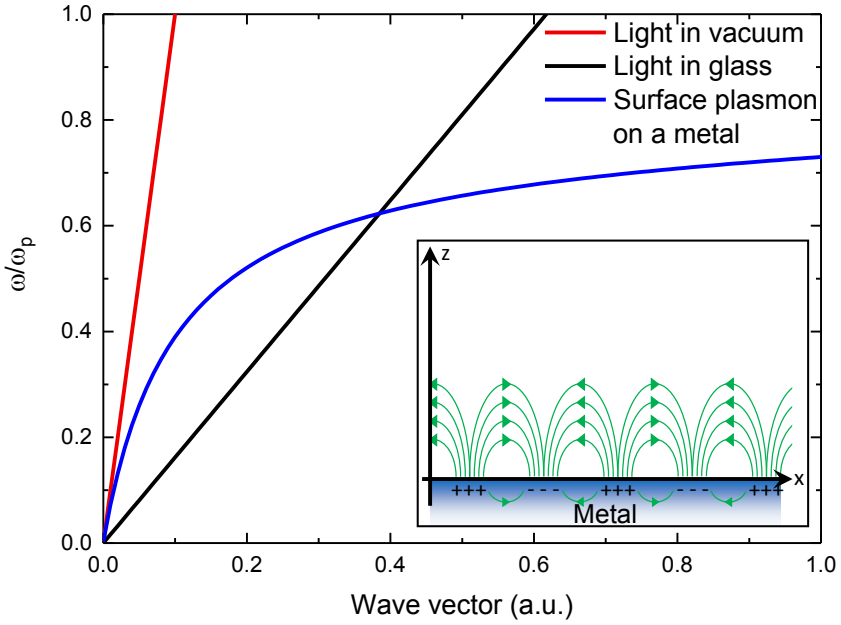

Figure 2.6.: Dispersion relations for light in vacuum (red line), for light in glass (black line) and surface plasmons on a metal (blue line). The plasmonic dispersion crosses the dispersion of light in glass at one point, which indicates that light can efficiently couple to surface plasmons. The inset illustrates the collective movement of electrons on the surface, representing a surface plasmon.

silicon follows a different dispersion relation than a photon in vacuum (different speed of light). This opens up a crossing point between the SP dispersion on the vacuum-metal interface (blue line in Figure 2.6) and the light dispersion in the medium, illustrated by the black line. At this point, light can couple to surface plasmons with a significantly higher efficiency [105].

Several different concepts exploiting plasmonic effects can be distinguished. Four major approaches are depicted in Figure 2.7. The first method of enhanced Raman spectroscopy is the Surface Enhanced Raman Spectroscopy (SERS), being illustrated by Figure 2.7a. The enhancement of SERS relies on several effects being introduced by the roughness of the surface. The main contributions are the field line crowding, the lightning rod effect and plasmonic resonances, as explained in detail in [106]. Due to Maxwell's equations, the electric field needs to be perpendicular to any metal surface, which causes a field line crowding of the plasmonic E-field on peaks of the rough surface.
The second concept is called Tip Enhanced Raman Spectroscopy (TERS), as displayed in Figure 2.7b, which relies on the same enhancement phenomena. The incident light is focused on the rough surface of a metallic tip in order to couple the incident photons to the SPs. A way to enhance the coupling efficiency is, to increase the surface roughness by e.g. structuring grids. By illuminating the tip from the side, SPPs are launched on the metal-air-interface of the tip. The SPPs propagate, due to the tip geometry, down to the apex and create a highly enhanced optical nearfield spot in the diameter of several nanometer [96], as sketched by the

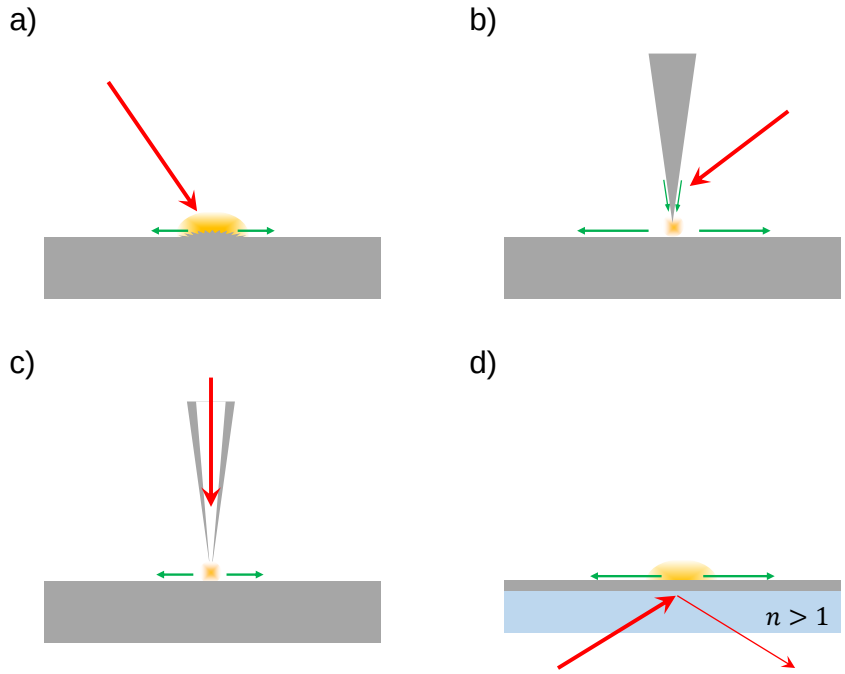

Figure 2.7.: Different concepts of enhanced Raman spectroscopy. a) Surface Enhanced Raman Spectroscopy (SERS); b) Tip Enhanced Raman Spectroscopy (TERS); c) Scanning nearfield optical microscopy (SNOM); d) Kretschman geometry for SERS.

yellow point in Figure 2.7b. An enhancement of several orders of magnitude can be achieved by employing this technique (cf. Figure 3.8) [107].
Another strategy to perform nearfield spectroscopy is illustrated in Figure 2.7c. Here, the incident light is guided through a cone shaped metallic tip. The inner diameter decreases subsequently, resulting in a highly enhanced local nearfield spot underneath the tip, represented by the yellow point in Figure 2.7c. This approach opens up the possibility of performing spatially localized optical spectroscopy [108] and is called aperture SNOM.
A possibility to increase the plasmonic coupling efficiency is offered by the so-called Kretschmann configuration, shown in Figure 2.7d (cf. [109]). Here, the light is focused through a higher refractive index material ($n > 1$) on a metal. The incident photons follow the black branch of the dispersion relation, plotted in Figure 2.6. At a certain point, there is no k-vector mismatch between the incident photons and the SPs on the vacuum-metal interface (blue line in Figure 2.6). If the metal layer is thin enough (nanometer regime), the incident light can be coupled to the SPs in a highly efficient way.

The possibility to efficiently couple photons to SPs is exploited by a variation of the aperture SNOM concept, the so-called apertureless SNOM. Here, the aperture SNOM and the Kretschmann geometry are combined. For this, we use the so-called Tetrahedral-Tip (T-Tip), being invented by U.C. Fischer et al. [110] to perform apertureless SNOM. The T-Tip is a tetrahedral glass fragment, acting as an apertureless nearfield probe.

The T-Tip combines the advantages of higher SPP coupling efficiency, due to the Kretschmann geometry with the possibility of performing nearfield spectroscopy. A tetrahedral glass fragment is metal coated on the sides, of the apex. A laser is focused to the apex through the backside of the fragment, as indicated by the red arrow in Figure 2.8a. In the focal volume of the laser, the incident light is coupled to the surface plasmons on the metal-air interface of the T-Tip. The SPPs propagate down to the apex, due to the tip's geometry. This results in an adiabatic squeezing of the SPPs and total reflection at the apex. There, a highly enhanced evanescent optical nearfield spot is formed, having a diameter of only several nanometer (cf. Figure 3.8) [46]. This is indicated by the yellow point in Figure 2.8a. The T-Tip is able to recollect emitted light within the size of the nearfield spot by dipole-dipole interaction. This means, an emitting molecule couples efficiently to the surface plasmons on the T-Tip [111].

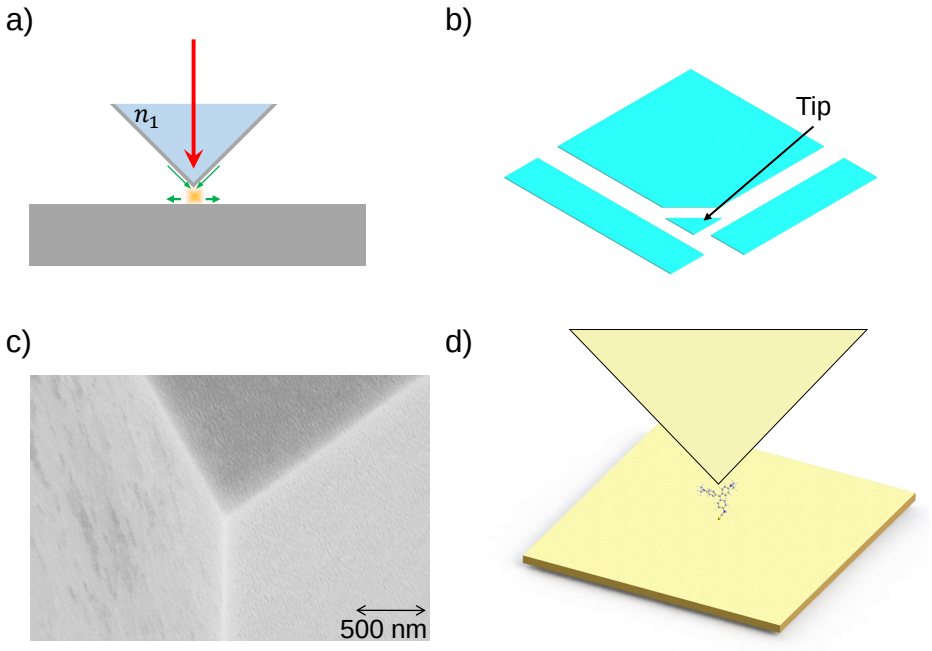

Figure 2.8.: Concept of apertureless SNOM (a), T-Tip fabrication (b) and SEM picture (c) of the T-Tip coated with gold. d) shows a scheme of the experimental configuration.

The glass fragment for the T-Tip is made from a standard Soda-lime glass slab with a thickness of 150 μm. In order to get an atomically sharp apex, the slab is dissected by breaking it in a controlled way. The production procedure is depicted in Figure 2.8b.
The Kretschmann geometry requires a glass-metal-vacuum structure. The three sides touching the apex are coated with a thin ($\sim$ 20 nm), conductive and plasmonically active metal layer. The coating procedure is the same as the one for the sample preparation and is described in section 2.4. A sketch of the T-Tip on top of a substrate with a Malachite green isocyanate molecule (MGIC) is shown in Figure 2.8d. The typically used coating material is gold, due to its inertness and plasmonic and optical properties. A SEM image of a T-Tip coated with 20 nm gold is shown in Figure 2.8c. From the picture, a flat surface on the order of several

tens of nanometer can be recognized. The quality of the enhancement as well as the size of the nearfield spot will be discussed later.

2.3. Density Functional Theory

The main idea of Density Functional Theory (DFT) was reported the first time by Hohenberg and Kohn in 1964 [112] as well as in 1965 by Kohn and Sham [113]. To calculate the properties of a large system (N electrons), using the Schrödinger equation requires a high calculation cost ($3N$ parameter). Hohenberg and Kohn proposed the reduction of the degrees of freedom in the Schrödinger equation by expressing the energy of the system as a function of the charge density of the electrons in the system. The modified Schrödinger equation has only three degrees of freedom. The computational solving of this equation is much simpler, compared with the initial equation.
The problem is that the functional is not known. Consequently, there are different functionals reported, which can be used for calculating the energy. Depending on the functional, the results vary.

The calculations shown in chapter 4 have been performed by Gong [114], using the *GAUSSIAN 09* package [115]. The employed functional *B3LYP* is a hybrid functional, using the non-local (α,β)-electron correlation from the *LYP* expression [116] and the local (α,β)-electron correlation from the *VWN* expression [117]. The basis set was *6-331G* [118].
First, the geometry of the molecule was optimized, afterwards the vibrational energies have been calculated from the optimized coordinates. All calculations represent the gas phase molecule, meaning without any influence of the electrodes (neither chemical influence, nor electric field or current).

2.4. Sample Preparation

The sample preparation as well as the tip preparation starts with a glass substrate with a thickness of 150 μm, which is mounted in an electron beam physical vapor deposition chamber (EBPVD) [119]. The evaporator (Leybold L560) is mounted in a UHV-chamber, having a base pressure of $\sim 10^{-7}$ mbar. Inside, an electron gun with electron optics and deflection coils are mounted. The electrons are accelerated to a crucible filled with metal. The metal heats up and starts to vaporize. Due to the open path between crucible and sample, a well-defined thin layer of metal can be deposited.

This amorphous film needs to be functionalized by depositing molecules on top. Two different approaches are used in this thesis. One is the drop cast method, which means a droplet of a well-defined concentration molecular solution is deposited on the substrate (2.4.1). The second approach is performed in UHV. A crucible with molecules is thermally heated under ultra-high

vacuum conditions. The molecules adsorb and bind to the substrate, which is placed in front of the crucible (2.4.2).
To characterize the quality of the sample, x-ray photoelectron spectroscopy was employed (2.4.3).

2.4.1. Drop Cast Method

The drop cast method is a commonly used approach to deposit molecules in a wet chemical way on low reactive materials, e.g. noble metals like gold and silver [120–124]. The used molecules exhibit thiol (4.1.1 and 4.2.1) and carboxylic (4.3.1) anchor groups. All used molecular species are solvable in tetrahydrofuran (THF).

The drop cast approach reported in literature [121] uses molecule deposition from a droplet in a solvent atmosphere. In order to create a solvent saturated atmosphere, a medium sized vessel is filled with its half volume with THF. In the center of the vessel, a high-grade steel post is placed. The top surface of the post is not moistened by the solvent bath. A ∼5x5 mm^2 piece of the substrate is placed on the post. Then, a droplet of ∼55 μl of a millimolar solution of molecules in THF is deposited on the substrate. The vessel gets closed after the deposition, in order to keep the atmosphere saturated and prevent the THF of the droplet from vaporizing.
The molecule deposition of thiol-anchored molecules takes about one day to form a saturated monolayer [121]. Acetyl protected thiol anchored molecules split their protection group of in contact with gold. This results in a covalent sulfur-gold bond. After this dwell time, the sample is taken out of the atmosphere and becomes rinsed by clean solvent (THF). This step removes all non-chemisorbed molecules from the surface.

In this thesis, the drop cast approach was adapted, to fabricate high quality samples in a shorter time. In this case, a droplet of ∼55 μl of a millimolar solution of molecules in THF is deposited on the sample in ambient conditions. In less than a minute, the droplet dries by vaporizing of the solvent. The concentration of the remaining solution on the substrate increases significantly during the vaporization of the solvent. The deposition procedure is repeated until the goal coverage on the substrate is reached. The substrate is then rinsed with THF several times in order to remove the molecules not binding to the surface.

2.4.2. Molecule Sublimation in UHV

The deposition of molecules on highly reactive (oxidizing) materials, e.g. nickel, makes it necessary to remove the oxide layer from the surface, which can be done by argon sputtering in UHV. Due to the extremely fast oxidation of bare metal films at ambient conditions, the molecules need to be deposited in-situ after the cleaning. Inside the chamber, a small crucible filled with powder of molecules is mounted on a temperature-controlled heater. By heating the crucible, the vapor pressure of the solid molecules increases. Above a certain temperature, the

sublimation rate is sufficient and the shutter in front of the crucible is opened. The substrate, being placed in a distinct distance to the crucible, is exposed to the molecular beam [125–127]. The molecules hitting the substrate adsorb and bind there, covering the sample up to a full monolayer. Further exposure leads possibly to multilayer formation [128].

2.4.3. Sample Characterisation by Photoelectron Spectroscopy

After depositing the molecules on the substrate, it is necessary to characterize it regarding the binding chemistry as well as the coverage.

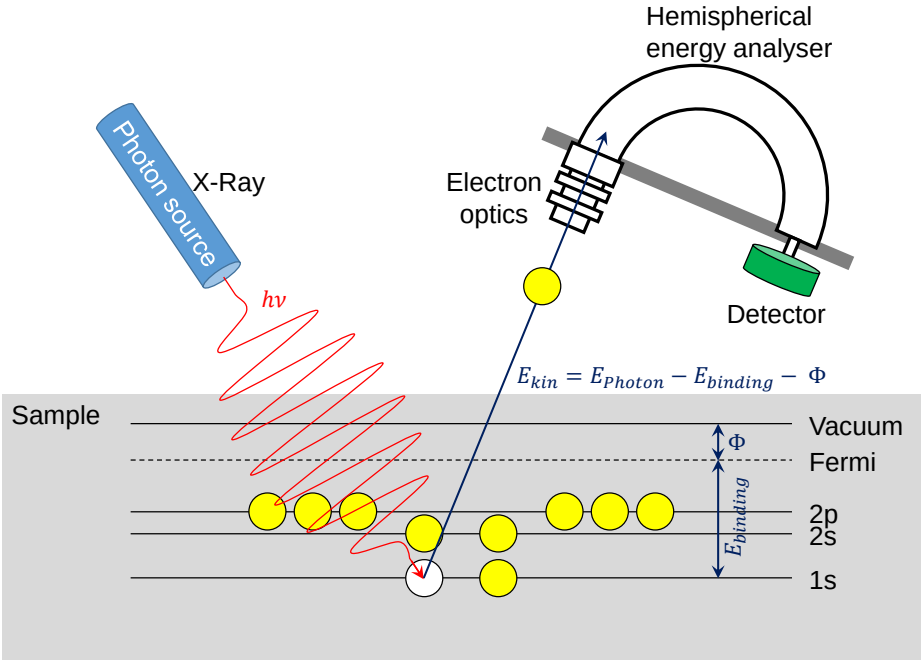

Figure 2.9.: Illustration of the working principle of X-Ray Photo Electron Spectroscopy. The incident photon forces an electron out of its shell. The photoelectron is collected, detected by the detection unit and its energy analyzed, as depicted in the top right.

Figure 2.9 sketches the concept of measurement for photoelectron spectroscopy, using x-ray (XPS) as the excitation source. The light source is depicted on the left side. A beam of light illuminates the sample. By the absorption of a photon, an electron is emitted, due to the photoelectric effect. The escaping electron has a kinetic energy of

$$E_{kinetic} = E_{photon} - E_{binding} - \Phi \tag{2.10}$$

E_{photon} describes the energy of the incident photon. $E_{binding}$ is the binding energy of the electron. Φ represents the work function of the material, which is given by the energy difference between the vacuum level and the Fermi level.

At the top right of Figure 2.9, the electron detection system is depicted. It consists of electron optics at the entry slit of a hemispherical analyzer and an electron detector at the exit slit. The analyzer itself transmits only electrons of a distinct kinetic energy and quantifies the energy resolution. In order to acquire a full spectrum, the pass energy of the analyzer is swept from the excitation energy to zero [129–131].

The technique of photoelectron spectroscopy allows the determination of the atomic/chemical species on the surface of the sample. The investigated intensities open up the possibility to calculate quantitatively the adsorbate coverage of a surface. Chemical shifts are observable by XPS too. The peak energy allows deducing the binding properties of the chemical species. Summarizing, XPS can qualitatively and quantitatively probe the chemical environment on a sample surface [131–133]. In section 4.3, XPS will be used to determine the binding chemistry of the molecules as well as the coverage of the sample.

CHAPTER 3

Improved Opto-Electrical Molecular Junction Spectroscopy Setup

The home-built ultra high vacuum opto-electrical molecular junction spectroscopy setup was completely rebuilt and refurbished, in order to achieve all the requirements, needed to characterize single-molecule junctions at low temperatures. Using the MJS technique, electric and Raman spectroscopy can be performed simultaneously, by employing an apertureless nearfield probe as counter electrode, which is a T-Tip (cf. 2.1).

3.1. Modified Vacuum System

The experiments were performed in an ultra-high-vacuum (UHV) environment, to prevent the molecules from decomposing in the presence of oxygen and strong optical fields (as reported by Domke [144]). The fundamental hardware part of this setup is a helium flow cryostat (Cryovac Konti-Kryostat UHV), which is mounted on a home-built UHV chamber, as depicted in light blue and gray in Figure 3.1. To change the tip or the substrate, the chamber can be opened at the center flange, as indicated by the dotted black line. The vacuum chamber is pumped by a "Edwards 12 rotary pump" and a "Balzer TPU060 turbomolecular pump", achieving a base pressure of $\sim 10^{-7}$ mbar at room temperature. The oil vapor originated by the rotary pump, which could contaminate the vacuum chamber is blocked by a catalytic filter, being mounted between the rotary pump and valve V_4. Lead bricks are used to constrain the tube between the rotary pump and the turbomolecular pump from transferring vibrations produced by the rotary pump. The turbomolecular pump employs ball bearings, resulting in low amplitude, but high frequency vibrations. To suppress the vibrations, a weight of 5 kg is mounted beneath the turbomolecular pump and the vacuum chamber, which results in a lower

resonance frequency of the bellow. Rubber dampers and a tension belt to the ceiling of the laboratory support this weight. The tension is adjusted to a level, where the damper - weight array reduces the vibrations, without introducing additional vibrations from the building.

The UHV chamber is continuously pumped, unless the tip or the substrate needs to be changed. While opening, the chamber is purged by nitrogen. During the evacuation time of the chamber, the valves V_1, V_2 and V_3 are closed and V_4 is opened.

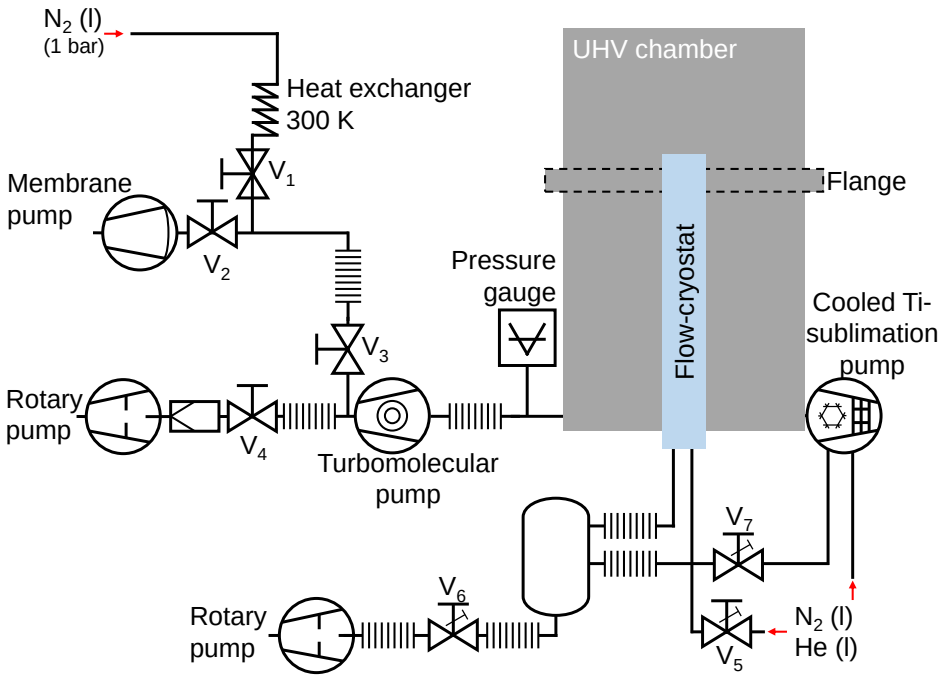

Figure 3.1.: Schematic drawing of the improved vacuum system of the MJS Steup

In order to purge the chamber, the rotary and turbomolecular pump are switched off and valve V_4 is closed. During the spin down of the turbomolecular pump (∼5 minutes), the tube between V_1 and V_3 is flushed by nitrogen. The membrane pump is switched on and the valves V_1 and V_2 are opened alternatingly. When the rotation frequency of the turbomolecular pump is below 25% of the operation speed, V_2 is closed, V_1 and V_3 are opened. At this point, the chamber is purged by dry nitrogen with a pressure of 1 bar. As long as the chamber is open, it is flushed.

The re-evacuation is done by closing the valves V_1, V_2, V_3 and opening V_4. Then the rotary pump is switched on. When the pressure reaches $\sim 10^{-2}$ mbar, the turbomolecular pump is switched on.
The pumping power can be increased by operating the especially designed titanium sublimation pump (TSP). The TSP built up on a CF100 flange, is ultra compact and features two high-current titanium filaments (40 A) and a cylindrical copper cryo shroud (see Figure 3.2), which can be cooled by liquid nitrogen, as depicted at the right side of Figure 3.1. The cylin-

drical cryo shroud has a mass of ∼1300 g, which can be cooled down to <100 K by pumping liquid nitrogen through the attached capillary (depicted in Figure 3.2). After cooling once, the cryo shroud stays cold (<150 K) for ∼6 hours. Thereby, a cryogenic pump without introducing further vibrations to the setup is installed. The cryo shroud can be cooled by operating the rotary pump of the helium pumping system and opening V_7 and V_6, however V_5 stays closed.

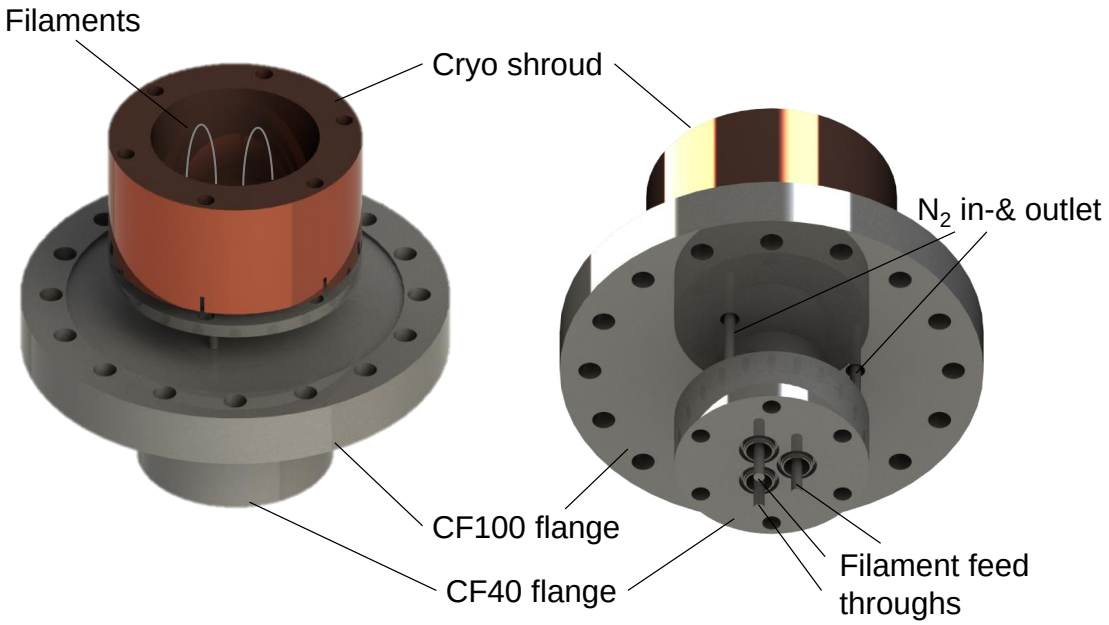

Figure 3.2.: SolidWorks image of the home-built titanium sublimation pump

In the center of the cryo shroud, the titanium filaments are mounted, as depicted in Figure 3.2. By operating the filaments with a current of 40 A for 60 s in intervals of 4 minutes, repeated 5 times, the base pressure of the chamber can be reduced to the low 10^{-8} mbar range. This results in a significantly slower formation of adsorbate layers on the sample, if the cryostat is cooled.

The cryostat provides a helium system for cooling, which is separated from the surrounding vacuum chamber, as depicted at the bottom of Figure 3.1. According to the specifications, this cryostat allows cooling down to 4 K. Additionally, the temperature can be stabilized by the use of a heater, which is PID-controlled. The cryostat features a capillary at the top of the cold finger. The width of the capillary is designed for the viscosity of liquid helium, but can be also used for liquid nitrogen. When the cryostat is being cooled, the helium system is connected to a liquid helium/ nitrogen reservoir by a vacuum isolated transfer rod and the rotary pump of the helium system is switched on (bottom of Figure 3.1). In case of using helium, the flow through the cryostat can be efficiently controlled by the needle valve V_5 in the transfer rod. If nitrogen is used, this valve is fully opened and the flow is controlled by the valve V_6 in the back flow line of the cryostat. The pressure in the capillary should not decrease

below 10 mbar, to prevent freezing of the nitrogen. The vacuum reservoir, which is installed between the flow cryostat and the valve V_6 is needed in order to reach a constant pressure in the back flow line of the cryostat. The constant pressure regime keeps the evaporation point of the cooling liquid exactly in the capillary. Otherwise, this point permanently moves from before to after the capillary, resulting in a not time-constant cooling.

The rotary pump, being responsible for the gas flow of the cooling medium, is constantly working and can handle a high volume flow. The transfer of the vibrations to the cryostat are damped by the mass of the vacuum-reservoir as well as flexible tubes, which are mounted by rubber dampers to the setup base.

The upgraded purging procedure while opening the chamber, in addition with the home-built titanium sublimation pump, reduced the base pressure by about two orders of magnitude and created thereby a cleaner environment for the single-molecule experiments. As second part, the vibrations of the installed pumps were eliminated as much as possible, which results in a significantly higher stability over a wide temperature range (see 4.1). At last, the helium system was adapted to be used by liquid nitrogen without freezing nitrogen in the capillary and disturbing vibrations.

A good vibrational decoupling combined with a pressure in the low 10^{-8} range and the possibility of cooling the setup down are the basis for the frontier experiment of investigating single-molecules at low temperatures.

3.2. Revised Mechanical Part

A schematic of the setup, based on the helium flow-cryostat is shown in Figure 3.3a. The CF100 cross, which acts as the mount for the cryostat and the TSP is vibrationally decoupled by rubber dampers from the ground. Due to the high mass of the setup, this decoupling is sufficient. On the left side of the cross, the turbomolecular pump system is attached. The right side mounts the titanium sublimation pump. From the bottom, the helium-pumping system is connected to the cryostat. The top of the chamber features a window, where the optics are mounted, which are necessary for the optical spectroscopy.

If the chamber is opened to change the tip or the substrate, the central part of the experiment is accessible, as illustrated by Figure 3.3b. This experiment head, which is attached on top of the helium flow cryostat, is easily recognizable (see Figure 3.4). Three screws mount the base slab of the experiment head to the cold finger of the cryostat, as depicted at the zoom in picture at the right side of Figure 3.4. This allows for cooling down the whole experiment to ∼30 K (cf. chapter 4.1).

The central part of the experiment is built up on a base slab. The piezo and tip holder are mounted on the base slab, being depicted on the left side of Figure 3.4. Three rods, used as guideways, support the tip holder. The tip holder - base slab distance is controlled by a

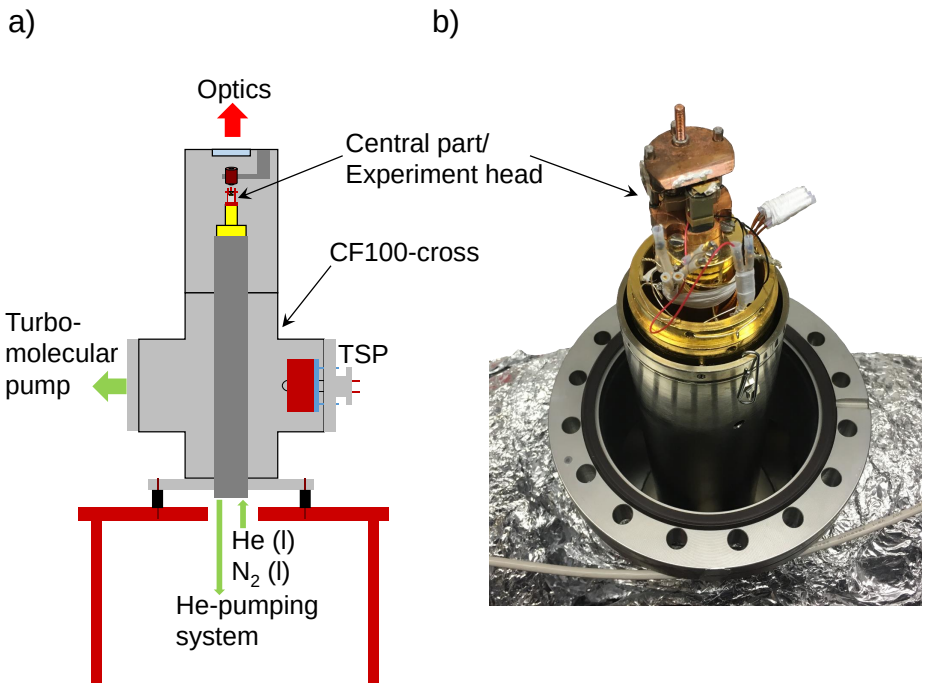

Figure 3.3.: Drawing and picture of the setup. a) schematic of the MJS setup. b) shows a picture of the chamber, opened at the central flange.

differential screw, having two windings with a different slope but the same direction, in order to allow a precise manual adjustment of the distance down to the low μm range. At the 45 degree sloped end of the tip holder, the tip is mounted on top of a thin glass slab, which is needed for electrical isolation. At the front of the base slab, a high precision piezo from Physical Instruments (Picma P-887.31) is mounted, which has an operational range of 8.446 μm at an applied piezo voltage of 90 V. This piezo only allows a movement in z-direction. The elongation of the piezo was calibrated by measuring the standing wave patterns between tip and sample (see appendix A.1) [46]. Any further possibility to move the sample is a potential source for instability (drifts, vibrations). Consequently, the x-y-movements were sacrificed to maximize the stability. On top of the piezo, a small magnet is glued, which locks the substrate holder into position, as shown at the left side of Figure 3.4. The substrate as well as the tip are glued and contacted by colloidal silver to their holders. The tip and the substrate are electrically contacted, using thin copper wires.

This geometry allows employing a wide variety of conductive materials as substrate, including ferromagnetic as well as antiferromagnetic materials. Furthermore, any plasmonic active and at the same time conductive material can be used to coat the T-Tip, which acts as counter electrode.

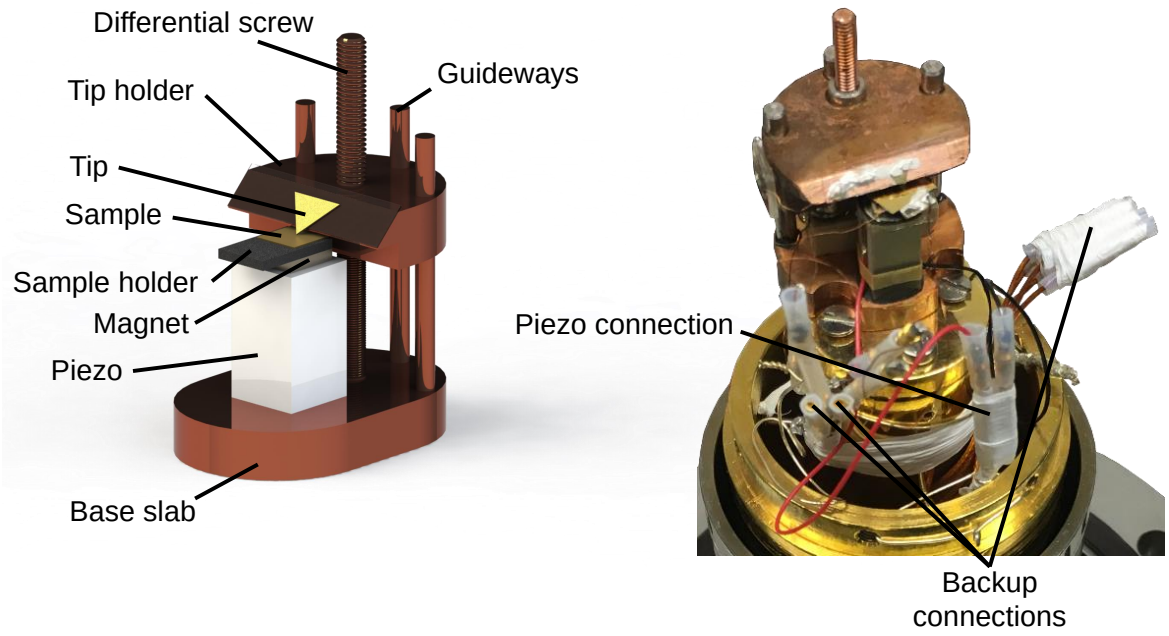

Figure 3.4.: The left side shows a image of the experiment head, which is mounted on top of a helium flow cryostat in a UHV-Chamber, as depicted on the right side.

3.3. Adapted Electrical Part

After explaining the general concept of measurement in the section 2.1, here the electronic environment, which is necessary to study the electric structure of single molecules, is explained in detail.
The electronic parts are depicted in Figure 3.6 on the bottom right. A self-written LabVIEW program, whose programming was part of this thesis, controls the setup. It includes the routines being necessary for calibrating the setup, forming the single-molecule junctions as well as performing Raman spectroscopy simultaneously. The different LabVIEW routines are explained in the appendix A.

The connections to the external measurement units with the experiment head have been renewed within this thesis too. The high voltage piezo connections are guided directly from the amplifier through two shielded MHV feed-throughs inside the chamber. From the bottom of the chamber to the connectors close to the central part (depicted at the right side of Figure 3.4) low impedance Kapton isolated coaxial cables are installed. Thereby, the shield is connected to ground and the inner core guides the voltage.

Similarly, the connection of the junction current is installed. Here, a Lemo plug acts as feed through. Inside the chamber, low diameter, low impedance Kapton isolated cables from Allectra are mounted. Again, the Teflon isolated gold-coated connectors at the top of the

flow cryostat are used. On the ambient side of the Lemo plug, the signal is also guided in single coaxial cables, where the shield is grounded. The consequent guiding of signal/ voltage in spatially separated and grounded lines reduced the noise level of the setup by a factor of three. If further electronic connections were necessary, seven backup lines are available. The possibility of connecting the sample holder by a plug additionally allows changing the sample with its holder and storing the unused sample inside the UHV chamber, attached to a magnet at the outer shielding of the cryostat.

An Agilent E5273A source meter is used to apply a well-defined junction voltage as well as simultaneously record the junction current. At the same time the piezo voltage, applied via a Meilhaus ME1000 digital input/output card, a home-built digital to analog converter and a home-built high voltage amplifier, is employed to control the tip-sample distance in a highly precise way.

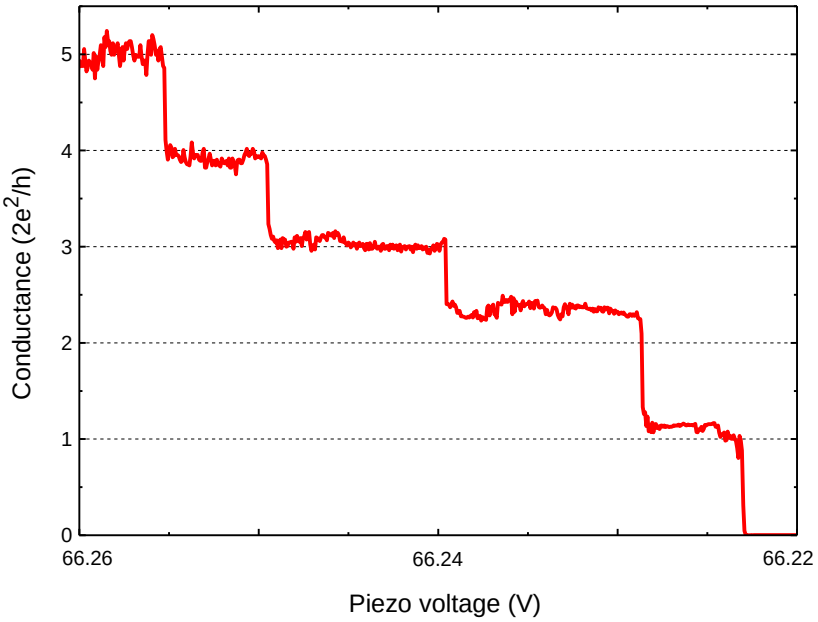

Figure 3.5.: Conductance quantization can be observed when a metallic (gold-gold) contact is established and subsequently broken, indicating that an atomically sharp contact has formed. Adopted from [46]

The source meter is able to apply voltages from the 1 mV to 10 V range with a precision of about 4 mV. The measurement accuracy is about 5 pA at a current range up to 10 μA. It is possible to determine the amount of averaging as well as the integration time per data point. In our experiments, it turned out that the integration over one powerline cycle (PLC) and average over three PLCs offers the best results. Integrating over the PLC reduces the influence of possible 50 Hz noise from the electric power supply to a minimum.
The source meter can be operated in two different modes. First, the so-called oscilloscope mode is employed, where continuously data points at a given voltage are recorded and plotted as a

timeline. This is used to form a junction by manual distance control. The second operation mode is used to investigate current-voltage-characteristics. This mode is chosen, after the junction is established, in order to acquire the electric characteristic of the junction. The current-voltage measurements are performed by ramping the applied voltage in discrete steps and record the current at each step, using the already described conditions of PLC integrating and averaging.

In order to control the tip-substrate distance precisely, a high precision low temperature piezo from Physical Instruments (type P-887.31) is used. To gain the highest possible resolution, the piezo-voltage needs to be noise-free and highly accurate. A home-built 16-bit digital to analog converter (DAC) with current output is used to pattern the piezo-voltage in 65536 digits, which allows a theoretical minimum step size of 0.26Å. The analogue output accuracy of the DAC is better than one digit. The current output is then converted to a voltage output between 0 V and 90 V. Thereby, the precision of the used HV amplifier is better than one digit of the DAC. Consequently, the DAC is the limiting device in terms of the step size. A real step size of 0.26Å can be estimated from the control unit point of view.

The fine tunable distance between tip and substrate as well as the possibility of keeping the distance constant for minutes within a range of less than one Ångström, offers a remarkable high stability, which allows experiments with single-molecules at room temperature.

The stability of the setup has been tested by measuring conductance quantization in gold-gold point contacts. The tip sample distance has been reduced, until a metallic contact was formed. Then, the tip was slowly retracted, while recording the junction current at a fixed bias voltage ($U = 0.01$V).
Figure 3.5 shows a stepwise decrease of the conductance during the retraction process. The conductance changes in multiples of the conductance quantum of $\frac{2e^2}{h}$. The possibility to form stable single atomic point contacts is a prerequisite for the ability to establish single-molecule junctions (section 4.1).

3.4. Expanded Optical Part

The optical part of the setup allows exploiting the enhancement properties of the T-Tip in a highly efficient way. A 100 times magnification and long working distance (3.4 mm) objective (Olympus LMPLFLN100X) with a numerical aperture of 0.8 is mounted inside the UHV chamber, as depicted and labeled in Figure 3.6 bottom left. The objective can be moved with a precision smaller than 1 μm in all three dimensions. For this, a Attocube ANP35 controller, employing two ANPX-101 (x-y-direction) and one ANPZ-101 (z-direction) actuators is used to control and read-out the actual position of the objective. Due to the limited load capacity of the actuators and the high weight of the objective, it was necessary to re-balance the objective (with its holder). A new holder, which allows the mounting of two springs for reducing the

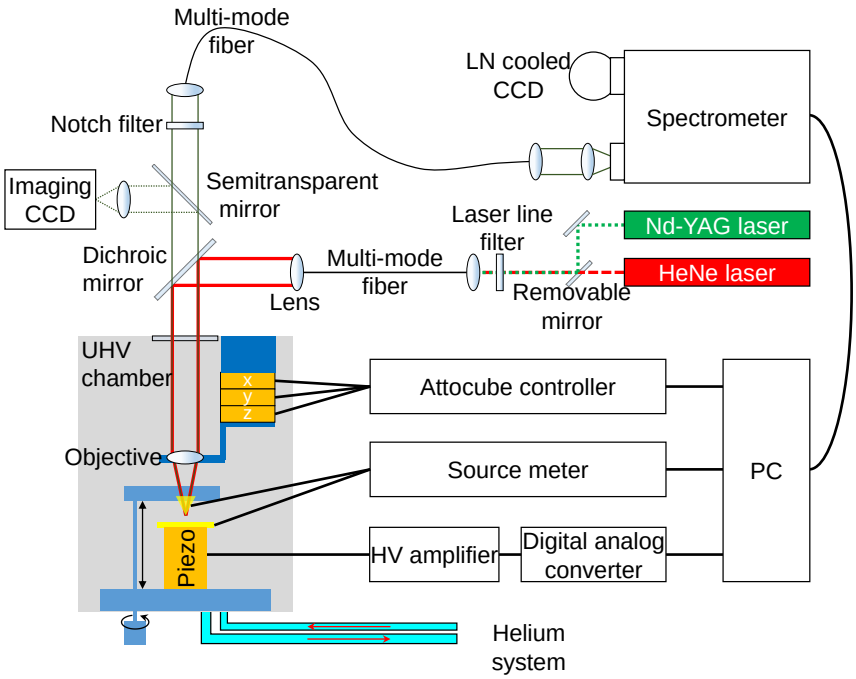

Figure 3.6.: Scheme of the setup, including the optical and electronic devices. The gray box on the bottom left represents the UHV-chamber, where the experiment head, depicted in Figure 3.4 is mounted on top of the helium flow cryostat. The optical part, including the two lasers as well as the spectrometer are shown in the upper part. All electronic components, the HV-amplifier, digital analog converter, source meter as well as the Attocube piezo actuator controller are illustrated at the bottom right.

load, was manufactured. At both ends of the holder, springs with different and adjustable spring constants are mounted. This results in the possibility of moving the objective parallel to the sample surface. Hence, the focus of the objective can scan the T-Tip in three dimensions in order to optimize the plasmonic coupling of the laser light as well as the collection of the Raman scattered light.

There are two different lasers available, as depicted in Figure 3.6 center right in red and green. One is a Helium-Neon-laser from Thorlabs (HRP120), having a power of about 12 mW. It is used for investigations on gold-coated T-Tips. In front of the red laser, a laser line filter is mounted in order to remove sidebands of the laser. Additionally a green laser (frequency doubled Nd-YAG-laser Coherent Compass 315m-150), which is better suited if silver, nickel or other higher band-edge materials are employed was mounted. Consequently, a new beam line was built and integrated with the beam line of the red laser. This results in the possibility of switching between the two lasers within a minute. The green laser offers to adjust the power up to 150 mW. The mirror in front of the red laser is removed, when it is operated. Otherwise, the mirror guides the green laser to an objective, being responsible for the coupling into the fiber. The center of Figure 3.6 shows a multi-mode fiber, having a core diameter of 200 μm (Fiberware AS200/220IRAN), which is used to guide the laser to the optical part of the setup. All fiber holders have been upgraded to ability of adjust all translational and

rotational degrees of freedom, in order to achieve full control over the optical path.
The thick red lines in Figure 3.6 depict the laser pathway, being collimated by a lens (focal length 40 mm). If the green laser is operated, the laser line filter is mounted between the lens and the dichroic mirror, in order to filter out sidebands and the fundamental oscillation of the laser as well as the fluorescence of components in the optical way. The laser light is reflected down into the UHV-chamber by a dichroic mirror, which is changed according to the used laser. It is reflective for the excitation light and transparent for other wavelength than the laser (20 nm bandwidth). Inside the chamber, the light is focused in the T-Tip. At the apex of the T-Tip, a highly enhanced nearfield spot emerges. The Raman scattered light is guided backwards by the tip, due to dipole-dipole interaction, as described in section 2.2. The T-Tip behaves like an efficient nearfield probe, having a reversible optical pathway.

The Raman-scattered as well as a small amount of the reflected laser light is guided through the dichroic mirror to a semitransparent mirror (uncoated thin glass slab). This mirror cuts out less than one percent of the light and reflects it to a lens in front of an imaging CCD, as sketched at the top left of Figure 3.6. The Imaging CCD is used to visualize where the excitation spot is located as well as to determine the focal plane. The remaining Raman-scattered light is guided through a Raman notch filter, suppressing the laser intensity by 10^{-5}. Afterwards, the light is focused again into a multi-mode fiber, which transmits the Raman signal to a spectrometer, where it is collimated and refocused to the spectrometer entrance slit.

The Spectrometer (Princeton Instruments SP2300i) spatially separates the light by its wavelength and projects the energy resolved entrance slit image to a liquid nitrogen cooled CCD (Princeton Instruments ST133). In order to vary the energy resolution, two different gratings are mounted. One is an 1800 g/mm diffraction grating, having a blaze angle of 532 nm, which is used for detailed energy resolution studies. The second grating has 600 g/mm, with a 532 nm blaze angle too. This grating is used for investigations needing a larger range of energy shift recorded at the same time.

As mentioned above, the objective can be moved in all three dimensions across the tip. A 3D cuboid can be screened pointwise, by various step sizes automatically by a LabVIEW routine (see appendix A.3.2). At each point a full spectrum, including the reflected laser light is acquired and saved. Therefore, the laser spot is focused by manual position control on the substrate, close by the tip (z-adjustment). Afterwards the x-y position is adjusted to be on the tip, close to the apex. Then the scan is performed.

The color in the 3D plot in Figure 3.7 illustrates the intensity of the laser reflection as a function of the location of the laser spot. The red colored area in Figure 3.7 corresponds to the backside of the tip, as indicated by the tip model. The yellow part represents the bottom edges of the T-Tip, meeting at the center of the plot.
The inset of Figure 3.7 exemplarily shows one of the investigated spectra. The laser peak is marked in yellow; the considered Raman peak is highlighted in red. The contour of Figure 3.7 shows the intensity of the Raman signal of a self-assembled monolayer (SAM) of Raman

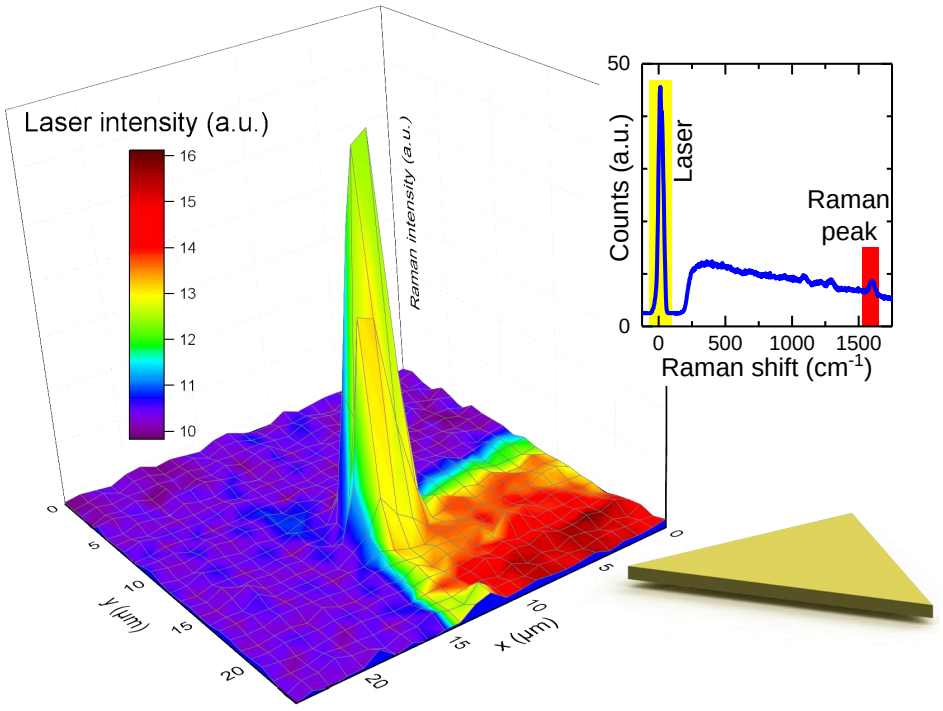

Figure 3.7.: 3D Plot of the spatially resolved Raman signal and laser line intensity. The color surface illustrates the brightness of the reflected laser light as a function of the spot position. The contour sketches the intensity of the detected Raman-scattered light of a SAM of organic test molecules. A FWHM spot size of the excitation laser spot of about 2 μm can be extracted. The inset displays exemplarily one of the acquired spectra.

active organic molecules (TPD). At the center, corresponding to the apex of the T-Tip, the Raman intensity is orders of magnitude larger than the surrounding area. A highly enhanced region at the apex of the tip can be recognized. The diameter of the enhanced spot is about 2 μm, which is in good agreement with the diffraction limited excitation spot size.

The extension of the enhanced nearfield spot has been investigated too. A gold-coated T-Tip MGIC Au-substrate configuration was used, as illustrated in Figure 2.8d. The MGIC (Figure 3.8a) molecule is known to be a very Raman active molecule, which is commonly used as a test molecule [107, 145–147]. Again, a 3D scan was performed to find the spot with the maximum signal. Subsequently, tip-sample distance was increased from full contact to a value of 18 nm. The black line in Figure 3.8b shows the investigated Raman signal in contact. The observed intensity after retracting the substrate by 18 nm is depicted by the red line. A difference of one order of magnitude in intensity can be observed.
Figure 3.8c illustrates the quantitatively investigated Raman intensity of peak A as a function of the tip-sample distance. A decrease to $\frac{1}{e}$ of its initial value is recorded at a distance of ~9 nm, as shown by the exponential fit (red curve).

An extension of the enhanced nearfield spot of ~9 nm can be concluded. Additionally, a nearfield enhancement of more than one order of magnitude could be observed.

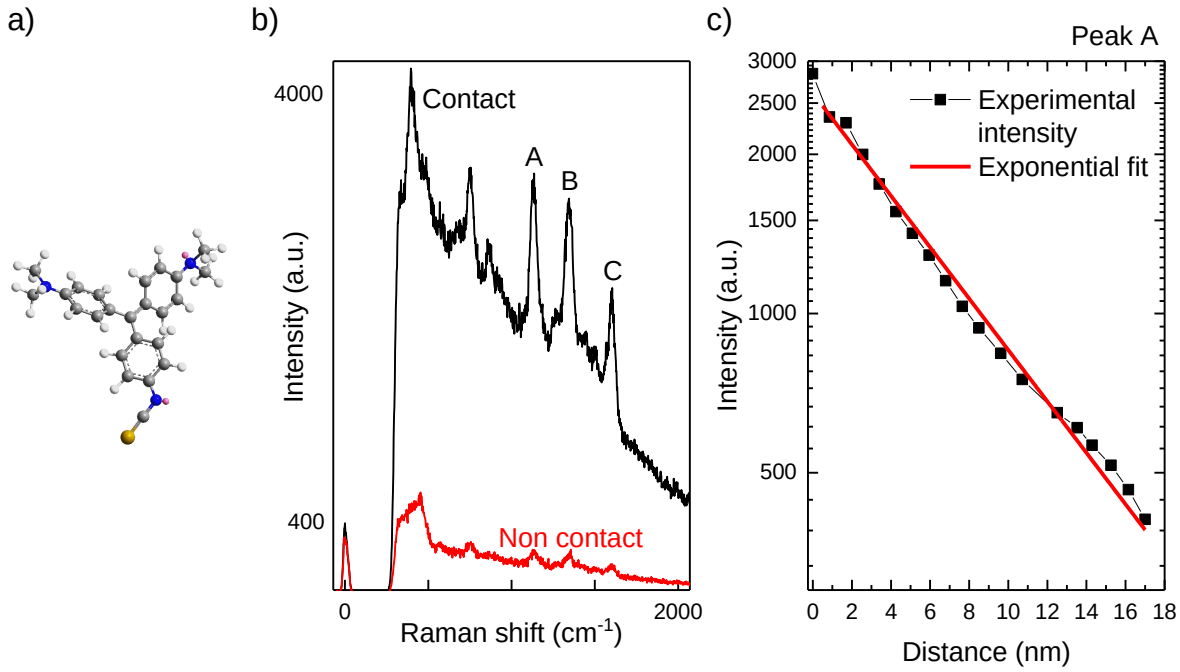

Figure 3.8.: Tip-sample distance dependent Raman intensity. a) molecular structure of MGIC. b) Raman spectra in and out of contact. The inset sketches the structure of the MGIC molecule. c) shows the intensity of peak A in dependence of the distance. Adopted from [46]

3.5. Experimental Procedures

This section describes the experimental procedure, starting with a fully retracted tip and ending with the investigation of Raman spectra of a single-molecule junction. All routines are programmed in LabVIEW as part of this thesis and are attached with a detailed description in the appendix A. Except for the feedback loop, every other automatized routine was newly developed and implemented. A further achievement is the possibility of controlling the optical and electrical measurements with one LabVIEW program, instead of WinSpec and Agilent VEE.

At first, the piezo is biased by 90 V, using a fast home-built tunneling electronic feedback loop, which reduces the piezo voltage as soon as the current between tip and substrate is bigger than a set point. Then, the tip-sample-distance is reduced by approaching the tip holder manually towards the substrate, using the differential screw, until the tunneling regime is reached. The tip is now in the working range of the piezo (8.4 μm).

For the next step, the tunneling electronic is switched off and the piezo control as well as the junction contacts are switched to LabVIEW controlled devices. The piezo voltage is set to 0 V and a junction voltage of e.g. 0.3 V is applied. The piezo voltage is ramped from 0 V up to the level, where a certain set current (e.g. 0.3 nA) is reached. When the set point is reached, the routine keeps the tunneling current constant by adjusting the piezo voltage permanently

(cf. appendix A.2.1). The approaching routine is kept running for about 30 minutes in order to reduce the drift and creep of the piezo and wait till the setup has stabilized.
To determine the conductivity of the molecules, a so-called current-distance measurement is performed (cf. appendix A.2.2), especially when investigating a new molecular species for the first time. A LabVIEW program, recording the junction current at a given voltage as a function of the tip-sample distance was implemented. The sample is approached until the set point in current is reached and then it is retracted until the current reaches the noise level. This procedure is usually repeated 100 times. It is possible to repeat the set of current-distance measurements with different junction voltages. The measured data often contains different regimes. The first regime is the noise regime, where no junction current is observed. Second, the tunneling regime is reached, where a roughly exponentially increasing current is observed, which is almost not influenced by the molecules. Third, after a step in the current, a plateau is observed, which is characteristic for the formation of a molecular junction. By approaching further, a metallic contact is established. From the plateau current as a function of the junction voltage from several tens of current-distance curves (I-d-curves), the conductivity of the molecule at a given junction voltage can be estimated.

Now, the piezo voltage is reduced by about 2 V from the tunneling contact, to ensure that the vibrations caused by the movement of the objective do not cause the tip to crash into the substrate. In this step, the objective (moved by the Attocube actuators) is roughly positioned so that the laser spot is focused close to the apex of the T-Tip (cf. appendix A.3.1). Next, two-dimensional scans (depicted in Figure 3.7) are performed (cf. appendix A.3.2). The first scan, using a larger step size (5 μm) is needed to determine roughly ($\pm$10 μm) the position of the apex of the tip. The second fine scan is performed with a step size of 1 μm. From the result of the second scan, the position with the maximum Raman signal at the tip can be determined and the laser is focused in this spot.

At this point, the optical part of the setup is prepared for the measurements. The integration time of the CCD is increased to a minimum of ten seconds, depending on the Raman intensity of the investigated molecule. The optical part of the setup is perfectly stable in the order of several hours. This means that after adjusting the laser spot once on the apex, no further aligning and optimization is needed.

A junction voltage of about 1.0 V is applied and the tip-sample distance is subsequently reduced by increasing the piezo voltage manually (cf. appendix A.2.3). This is performed until the tunneling regime is reached. The current is kept constant by manual distance control, at a very low value (slightly above the noise level) for about 30 minutes to reduce again the drift and the creep of the piezo.
As a consequence, the setup is stable enough to form a single-molecule junction. The current is increased by reducing the tip-sample distance, to a value slightly below the one determined by the current-distance curves (shown e.g. in Figure 4.2). The formation of a junction by staying in this regime for a longer time is likely. As soon as a molecule binds with the second anchor to the tip, a jump like increase of the junction current is observed. Due to the small coverage

of molecules on the substrate, only every tenth to 20th approach leads to a single-molecule junction. If no junction is formed, the last steps are repeated until a junction is established.

When the junction has formed, optical and/ or electrical spectroscopy can be performed. Optical spectroscopy means investigating the Raman spectra as a function of the applied junction voltage or in dependence of the applied stress on the junction (retracting or approaching the electrodes between the measurements). The first is used for the investigations in section 4.1 and 4.3. The second method is employed for the experiments in section 4.2.
To characterize the junction electrically, the current as a function of the applied voltage is investigated. In our experiments, it turned out that the most reproducible results could be obtained, if the voltage is swept from -1.5 V to +1.5 V in 200 discrete steps. The molecules in a junction are sensitive to voltage pulses/ steps as well as large currents/ voltages resulting in the breaking of the junction. The use of more and smaller steps in a given voltage range makes the investigated results become more reproducible. Above $\pm$1.5 V the junctions tend to destabilize. A reason for that might be the high current or the large electric field in the gap between the electrodes.

CHAPTER 4

Results and Discussion

In the following, we demonstrate that we can characterize single-molecule junctions electrically as well as spectroscopically, even at low temperatures of ∼77 K.

In section 4.2, stress-induced changes in the vibrational spectrum of 1,7-dithiol-7-helicene molecules are presented and discussed, using a gold substrate and a gold-coated T-Tip. A softening in a specific vibrational mode induced by pulling the molecular junction was observed.

Third, the electron transport properties of (1,2-ethynediyl)dibenzoic acid in ferromagnetic as well as non-magnetic junctions were examined (4.3). Different charge-states were identified by optical and electrical spectroscopy and a negative differential conductance could be observed, which could be explained by a spin-valve configuration.

4.1. Molecule Junction Spectroscopy at Low Temperatures

A major goal in the field of nano devices is to perform logic operations on molecules. Therefore, different approaches have been followed [25, 158, 159]. The main issue is to address single-molecules as active parts in devices. The MJS technique allows the investigation of single-molecules at room temperature. The ability of cooling down was not employed in previous work. The setup is based on a helium flow cryostat, whose stability (vibrations, drift) depletes drastically up on cooling. The following section demonstrates that the pilot experiment of investigating single-molecules in a wide temperature range with this setup

was successful. From previous work it is known that the molecule [2,2',2",5'-tetramethyl-[1,1':4',1"-terphenyl]-4,4"-dithiol] (TM-TPD) acts as an optical switch, caused by changing its conformation, due to triggering different charge states by the applied voltage [46, 48, 114, 160]. The molecule [1,1':4',1"-terphenyl]-4,4"-dithiol] (TPD), which shows no switching behavior at room temperature, was investigated too. The comparison of the investigated data at different temperatures reveals that TPD also changes its conformation/ Raman intensity with voltage at lower temperatures.

4.1.1. Sample Preparation

The molecule TM-TPD as well as TPD feature thiol groups to anchor the molecule to the tip and the substrate. The samples were prepared by using the drop cast method (2.4.1) on an amorphous gold film. Figure 4.1 sketches the experimental configuration.

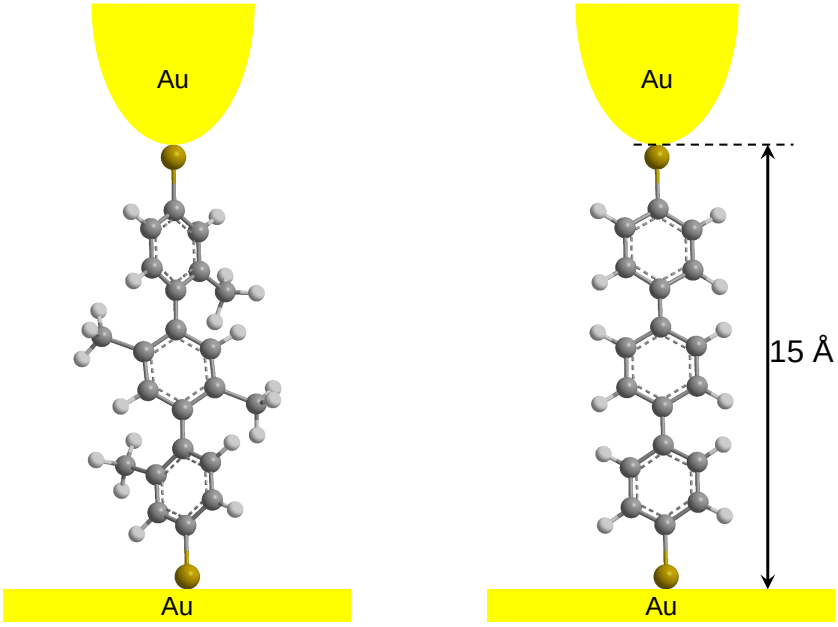

Figure 4.1.: TM-TPD at the left side and TPD at the right side within a junction.

Due to the chemical similarity, the same preparation recipe could be used for both molecules. The Marcel Mayor group at Uni Basel prepared the TM-TPD molecule powder. Sigma Aldrich provided a 99.8% pure molecule powder of TPD. Thus, a 0.3 mM molecule-solution, using THF as solvent was prepared. A droplet ($\sim$55 μl) was deposited on the gold surface. When the solvent was completely vaporized, a new droplet was added. This procedure was repeated 5 times, then the sample was rinsed 3 times with $\sim$1 ml THF. The described preparation procedure results in a low-coverage substrate. From XPS it can be estimated that the coverage

is in the range of ∼15% of a monolayer. The molecules are statistically distributed on the surface, which means that just a few molecules can be within the optical nearfield spot. The prepared sample was glued on the substrate holder and mounted in the MJS-setup (cf. section 3).
Due to the nature of the anchor groups, a gold-coated T-Tip was used. In this case, the gold coating on the T-Tip exhibited a thickness of ∼20 nm.

4.1.2. Voltage-Driven Conformational Switching in a Single-Molecule Junction at Low Temperatures

At first, the "lock-in" behavior during the approach of the tip to the TM-TPD functionalized substrate with successful chemical bonding to the tip was investigated, as shown in Figure 4.2a. Initially, no current above the noise level is observed. Then, the exponential tunneling regime is reached, as expected from a narrowing gap. In this regime and at this voltage, electrons tunnel through the molecules, similar to the tunneling through a dielectric, from the tip to the substrate.
Finally, a step-like increase can be recognized, followed by ∼15 Å wide a plateau in current.

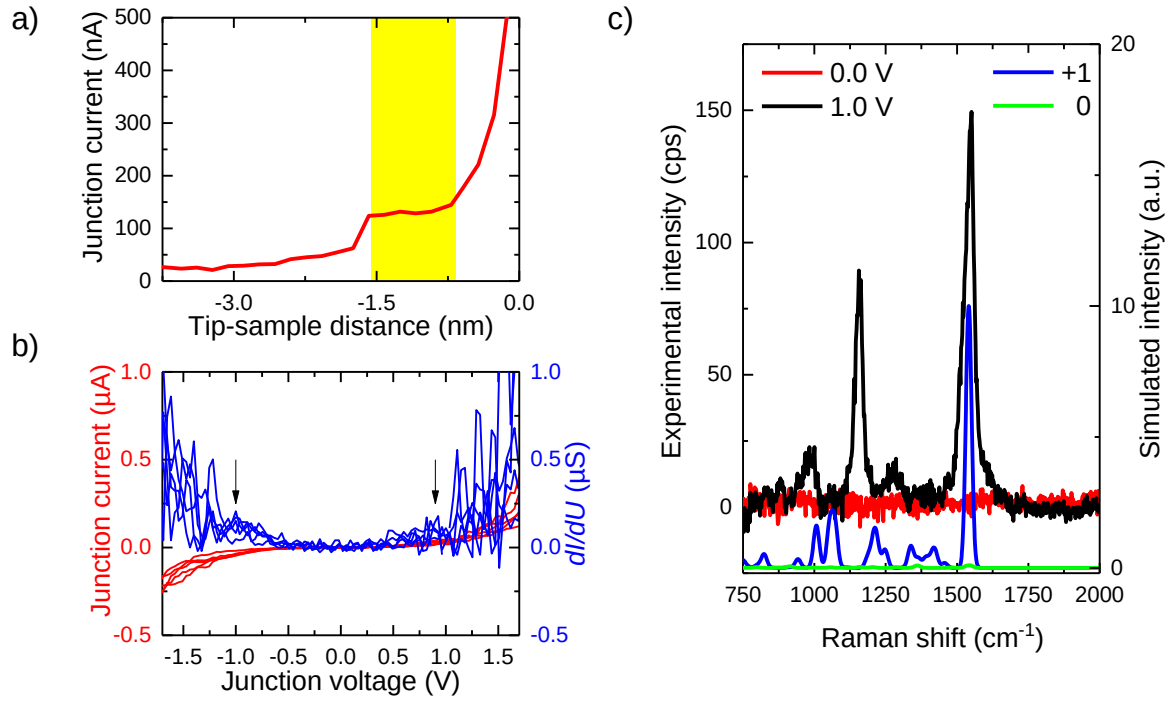

Figure 4.2.: Experimental current-distance, current-voltage and spectroscopy results of TM-TPD. a) shows an approach curve at 0.1 V. The yellow marked area sketches the regime, where a single-molecule junction is formed. b) depicts the investigated current-voltage characteristics (red) of several TM-TPD junctions, including the differential conductance (blue). c) displays the room temperature Raman signal of a TM-TPD junction at different voltages (red and black) and the DFT simulated Raman spectra for the neutral (green) and the positively (blue) charged molecule. Adopted from [46]

This area, marked yellow in Figure 4.2a, is the region, where the junction is established. The plateau indicates that a molecule is bridging the electrodes and opening up a new additional transport channel between the electrodes. A metallic contact can be achieved by reducing the tip-sample distance further (0 Å). This measurement indicates that only one single-molecule is measured per junction, as long as the measurement is performed in the yellow marked regime. Figure 4.2b displays the current-voltage characteristics of gold-(TM-TPD)-gold junctions. The red curve depicts the junction current as a function of the junction voltage, whereas the corresponding differential conductance is shown by the blue curve. At a voltage of ±1.0 V, a marked like increase in the current is observed. The differential conductance reveals a peak-like feature at this voltage, as marked by the arrows.

Figure 4.2c depicts the investigated Raman signal of a TM-TPD junction at different applied voltages and DFT simulated spectra for the neutral (green) and the positively charged state (blue) of the molecule. Between a junction voltage of -0.9 and 0.9 V, no signal is observed. Above the threshold of ±1.0 V, the Raman-response of the molecule is switched on. The threshold level fits to the measured peak-like feature in the differential conductance on TM-TPD junctions.

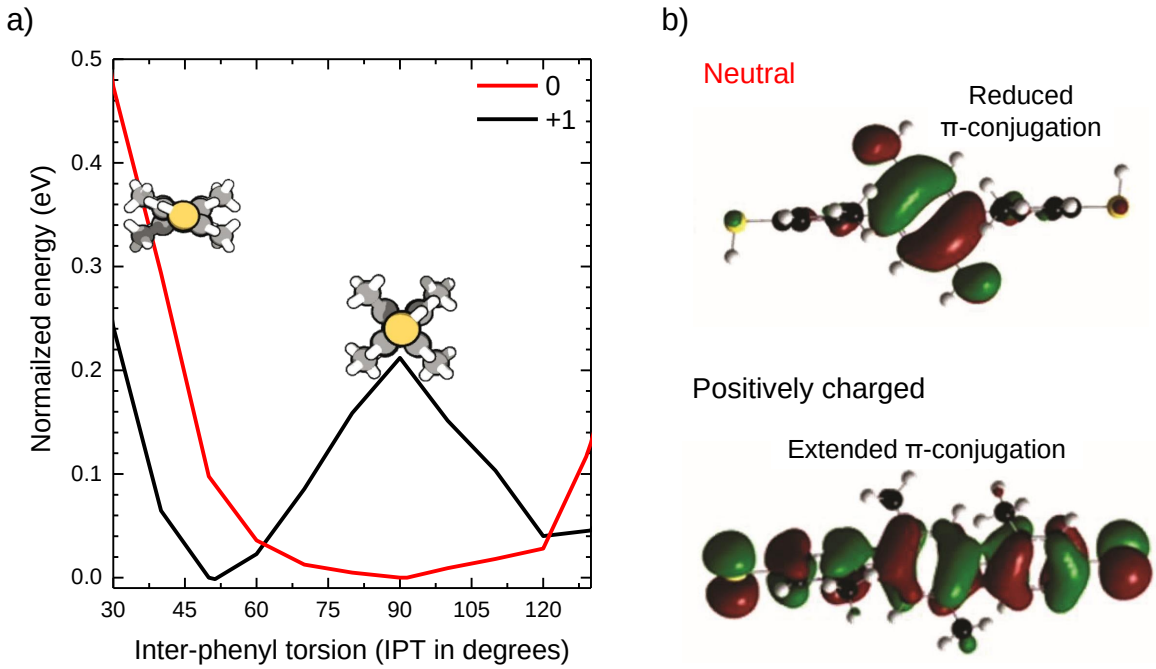

Figure 4.3.: DFT simulated potential landscape and orbital structure. a) displays the calculated inter-phenyl torsion (IPT) angles vs. ground state energy (neutral and positively charged). b) depicts the simulated spatial distribution of the HOMO of TM-TPD for the neutral and +1 charged state. Adopted from [46].

The investigations revealed that a Raman signal is only observable, if the molecule is contacted and a voltage above the threshold (±1.0 V) is applied (cf. [46, 48]). The occurrence of a Raman signal in conjugation with a change in the bias voltage indicates that we observe single-molecules, which are located in the junction. By looking into the ground state conformation of

different charge states of the molecule, the change in the Raman intensities can be attributed to a conformational change of the molecule.

Figure 4.3a displays the calculated ground state energy in dependence of the inter-phenyl torsion angle (IPT). The IPT is the torsion angle between the upper and the center phenyl ring (see Figure 4.1). The red curve shows the neutral TM-TPD energy. The black curve represents the energy landscape of a positively charged TM-TPD. Due to the steric hindering, caused by the methyl groups of TM-TPD, the uncharged molecule shows minimum energy IPT of 88°. The +1 charged molecule exhibits the minimum energy at an IPT of 52°. Hence, a conformational change from the neutral to the positively charged species can be concluded. Figure 4.3b depicts the spatial distribution of the HOMO of TM-TPD for the neutral and the positively charged state. The neutral state, having the ground state conformation, shows a reduced-conjugated π-electron system, located on the center phenyl ring. This results in a low polarizability of the molecule. The modified conformation of the +1 charged state exhibits a full π-conjugation. In contrast to the neutral case, the conjugated π-system of the charged molecule reveals a large polarizability. This leads to a remarkable change in the Raman intensity by the conformational change, as expected also from the DFT-simulated Raman spectra (see Figure 4.2c).

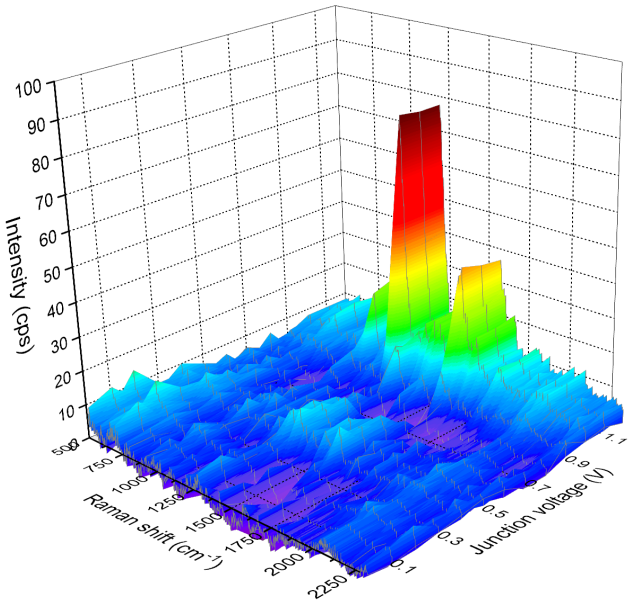

Figure 4.4.: Color-surface plot of the investigated TM-TPD Raman spectra at 77 K as a function of the applied junction voltage.

The calculated potential landscape raises the question about the stability of the conformation at room temperature and the influence of thermal fluctuations. If the conformation were not stable, the measurements would reveal a mixture of the assumed conformations during the

investigation. A reduction of temperature could reduce the amount of energetically reachable torsion angles, resulting in different spectroscopic signatures compared to the behavior at than at room temperature.

The flow cryostat was cooled down to 77 K using liquid nitrogen. In order to reduce the amount of adsorbed contamination on the sample, the home-built Titanium sublimation pump has been operated several times as well as its cryo-shroud was cooled down to 77 K. By this, a reduced base pressure of $1 \cdot 10^{-8}$ mbar was obtained. When the cryostat reached 77 K, the setup needed to be thermalized for two hours in order to minimize thermal drifts. Then, the tip was approached, the objective was positioned right on top of the apex and a junction was formed and investigated. In contrast to the measurements at 300 K, the success rate of the junction formation decreased, because more tip conditioning was necessary, due to the subsequent formation of adsorbate layers on the sample. Consequently, only every ∼100th approach led to a successful formation of a molecule junction.

Figure 4.4 depicts the investigated Raman signal of a single-molecule TM-TPD junction at 77 K as a function of the applied junction voltage. The maximum lifetime of a junction at the reduced temperature was ascertained to ∼5 minutes. Compared to the room temperature measurements, additional vibrations due to the nitrogen pumping system as well as thermal drifts are observed.

No Raman signal occurs as long as the applied junction voltage is below 1.0 V, as recognizable

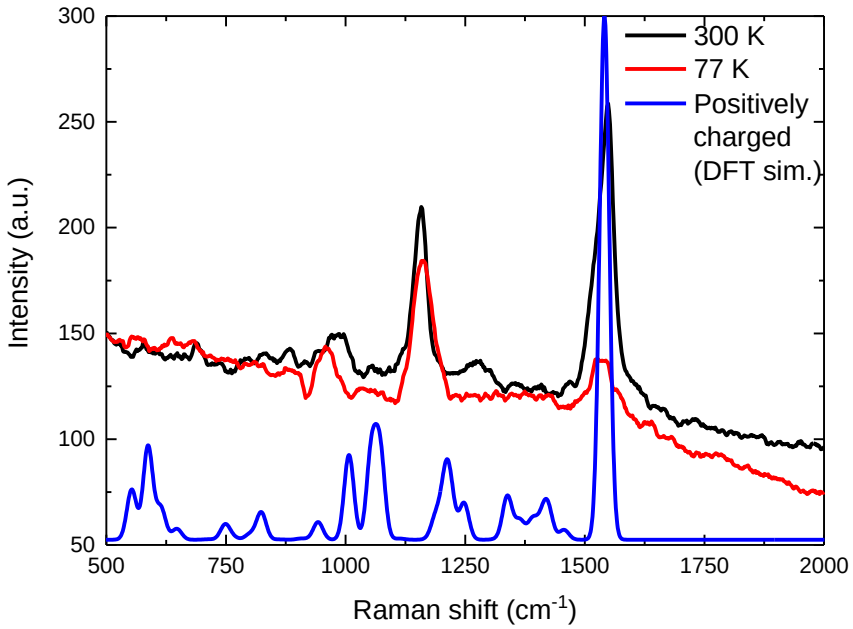

Figure 4.5.: Experimental TM-TPD data for room temperature (black) and low temperature (red) plotted, in blue the DFT-simulated spectrum for the positively charged molecule is shown.

from Figure 4.4. Above the threshold, again (similar to Figure 4.2) several peaks arise. The

experimental result fits well to the theoretically calculated behavior, according to the change of the conformation.

To compare the low temperature results with the room temperature ones as well as with the simulation, both *on* state signals and the calculated signal of the positively charged molecule are plotted together in Figure 4.5.
The red and black curves depict the investigated Raman spectra of TM-TPD at 300 K and at 77 K. A change in the intensity of the observed peaks occur. The peak at a position of 1160 cm^{-1} is similar in its energy as well as its intensity for 300 K and 77 K. The initially dominant peak at 1550 cm^{-1} decreased to one sixth of the peak intensity at 300 K.
The tiny side peak at 980 cm^{-1} shifts to a position at 960 cm^{-1} at 77 K, thereby it is not changing in intensity. The second side peak at 1270 cm^{-1} completely disappears by varying the acquisition temperature from 300 K to 77 K. Similar phenomena have been observed even at RT and can be assigned to statistical fluctuations, occurring if single-molecules are investigated.

Due to the mentioned difficulties on the formation and stability of the single-molecule junction at 77 K, this experiment was performed as pilot experiment. Therefore, the feasibility of investigating single molecules at 77 K was furnished, but the experiment on TM-TPD was not repeated several times in order to gain more statistics on the data.

4.1.3. Voltage Induced Raman Intensity Change of the TPD Molecule at Low Temperatures

The second investigated molecule is the TPD species (Figure 4.1 right side). The binding chemistry as well as the chemical structure is similar to the methylated TM-TPD. The only difference is the absence of the methyl groups, resulting in the removal of the steric hindrance. Consequently, the optimum IPT angles reveal different values than the one for the methylated molecule. The current-voltage characteristics of TPD junctions at 300 K are depicted in

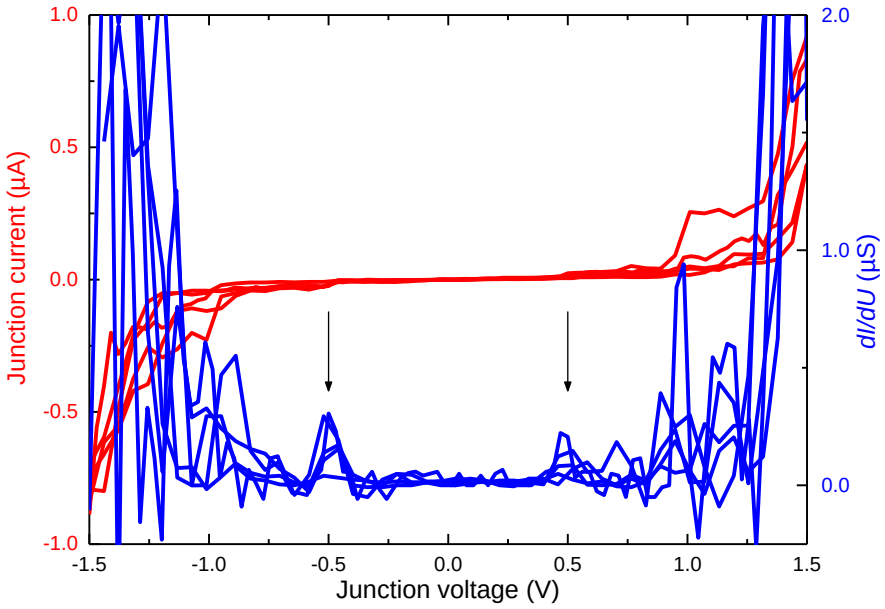

Figure 4.6.: Current-voltage characteristics of TPD at 300K. The arrows mark the peak-like features in the dI/dU curves, which are assigned to the charging point of the molecule.

Figure 4.6. Similar to Figure 4.2b, the conductance shows a step-like increase at a certain threshold voltage. The conductance changes at ± 0.5 V, as observable by the peaks in the differential conductance (blue curves). The peaks are highlighted by the arrows in Figure 4.6. The change occurs at a lower voltage as well as a higher conductance in contrast to the TM-TPD system. The TPD molecule reveals a smaller inter-phenyl torsion angle than TM-TPD, which results in a better conjugated π-electron system (shown later). This higher conjugated π-electron systems causes a higher conductivity, which can be seen from the current-voltage characteristics.

The TPD system was investigated at room temperature as well as at a reduced temperature of 77 K. Figure 4.7 illustrates the junction voltage dependent Raman signal for room temperature (a) as well as 77 K (b).

At 300 K no intensity change occurs, as can be seen from the 2D color map plot at Figure

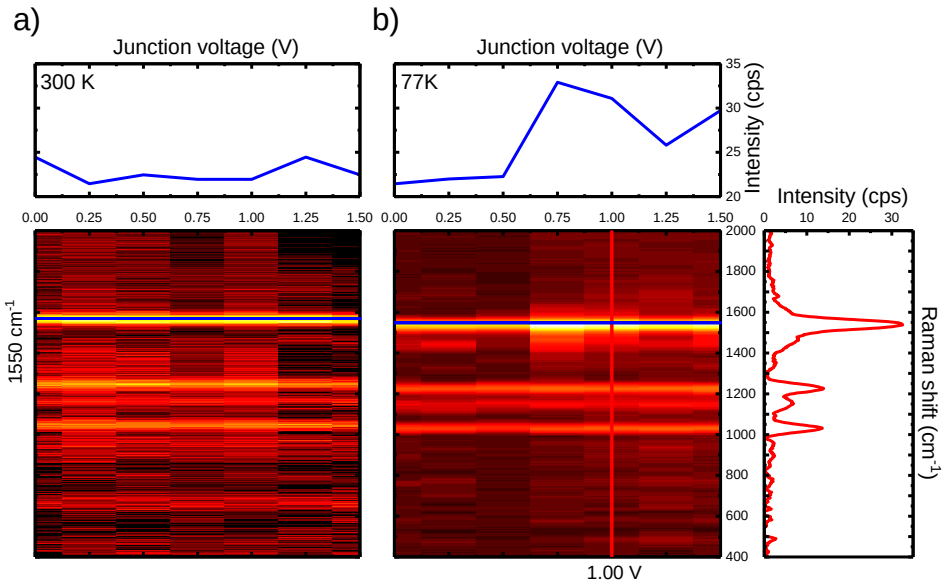

Figure 4.7.: Voltage and temperature dependent Raman signal of TPD. a) depicts the TPD Raman spectra as a function of the junction voltage at room temperature, b) shows the junction voltage dependent Raman signal at 77 K.

4.7a. The total intensity of the Raman-peak at 1550 cm^{-1} (blue line in the 2D plot) is shown in dependence of the applied junction voltage at the top of the color map plot. In this intensity plot, no voltage dependence of the Raman signal is observable.
The Raman spectra acquired at a reduced temperature of 77 K display a change in the Raman intensity with the junction voltage (see Figure 4.7b). Above the threshold voltage of 0.5 V applied to the junction (fits to the peak positions in Figure 4.6) the Raman intensity increased to 1.5 times of its initial value, as depicted in the color map and the intensity plot at the top of Figure 4.7b. This is in contrast to the room temperature measurement, where the intensity stayed constant over the whole junction voltage range. The remarkable change might be due to the lower temperature, which causes the center phenyl ring to stay closer to its optimal torsion angle. At the right side of Figure 4.7b, exemplarily one investigated and baseline subtracted Raman-spectrum of the TPD-system at 77 K and 1.0 V junction voltage is shown.

In order to clarify the observation of the intensity change at 77 K, the simulated spectra for the neutral (black) and the positive state (red) are plotted together with the experimentally investigated spectra below (0.0 V - blue) and above the threshold (0.6 V - green) in Figure 4.8.
By looking at the intense simulated peak at a Raman shift of 1550 cm^{-1} at Figure 4.8, it is obvious that the positive species (red) shows a slightly higher intensity than the neutral one (black). The simulated intensity difference between neutral and positive charge state fits the

intensity change at the threshold junction voltage of 0.5 V well, as depicted by the blue and the green curve in Figure 4.8.

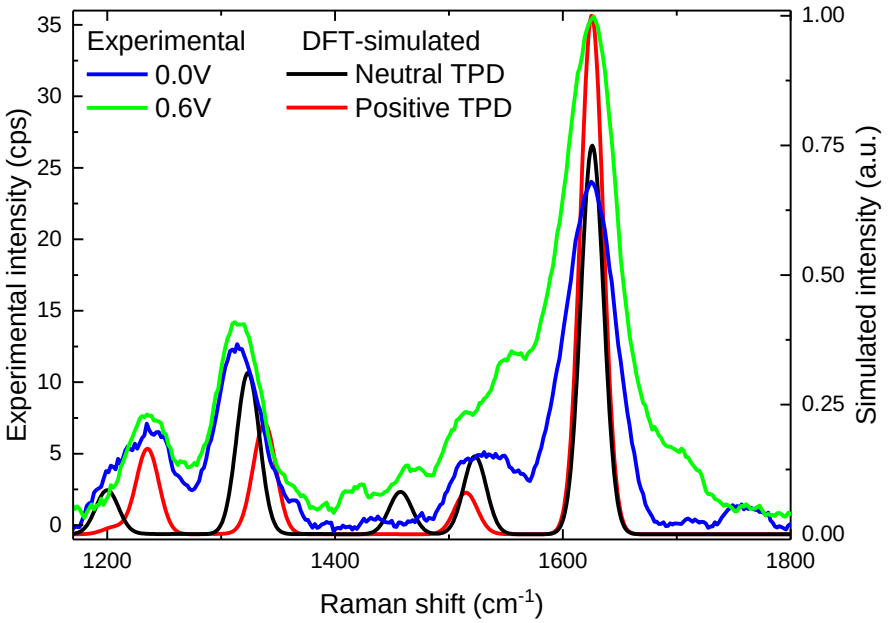

Figure 4.8.: Simulated and experimentally investigated Raman spectra (at 77 K) for TPD.

The observed intensity change of the peak at 1550 cm^{-1} can be explained by the smaller difference between the optimal IPT of the neutral and positively charged TPD. Figure 4.9 shows the simulated potential energy ΔE as a function of the inter-phenyl torsion angle for both states. In comparison with the TM-TPD landscape, a potential curve with a significantly broadened minimum can be seen.

The calculated optimal angles are 33° for the neutral molecule and 24° for the positively charged TPD molecule, as illustrated by the insets in Figure 4.9. Here, the optimum torsion angle of the two different conformations are closer to each other than in the TM-TPD case. The thermal energies ($\frac{3}{2}k_B T$) for 300 K (pink) and 77 K (green) are marked in Figure 4.9 right side. Both simulated torsion angle curves show a significantly higher amount of energetically reachable range of torsion angles at 300 K. The occurrence of an intensity change at 77 K in contrast to 300 K indicates that the reduction of the electrode temperature by cooling the system forces the center phenyl ring to stay closer to its optimal angle, being different for the two charge states.

In summary, the feasibility to investigate electrical as well as the optical properties of single-molecule junctions at low temperatures has been demonstrated. The TM-TPD system acts as a voltage-driven conformational switch shown by its optical Raman-response both at low and at room temperature. The equivalent unmethylated molecule (TPD) was investigated, which

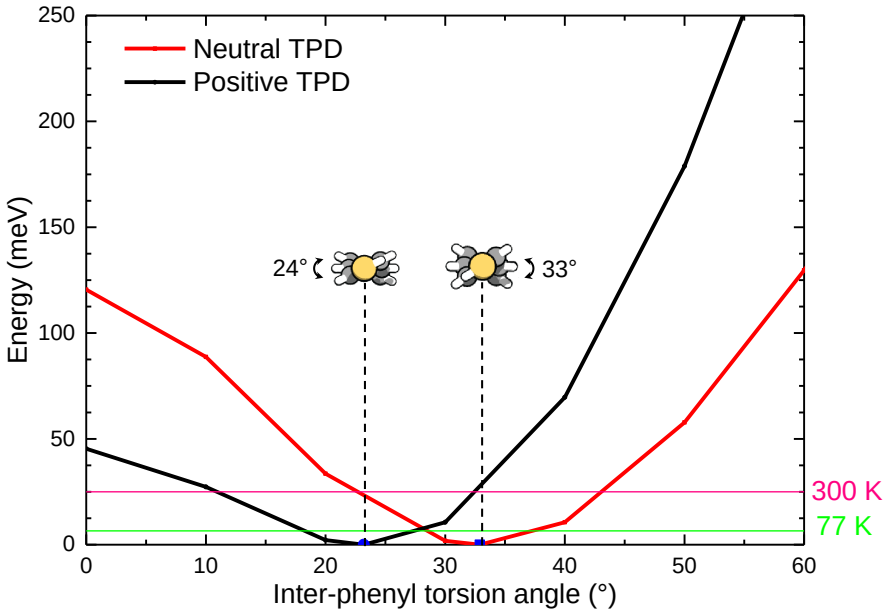

Figure 4.9.: DFT-simulated potential landscape of the inter-phenyl torsion angle for TPD (red and black). The pink and green curves show the thermal energy of 77 K and 300 K.

does not show such behavior at room temperature. The comparison of room temperature and low temperature measurements reveal that TPD also changes its Raman intensity according to the applied voltage, albeit only observable at low temperatures. From these results one can conclude that the MJS-setup is able to probe the electronic as well as the vibrational properties of single-molecules in a wide temperature range.

4.2. Strain Induced Shifts in Vibrational Frequencies of 1,7-Dithiol-7-Helicene

The following section gives an overview about results of the experimental study of the 1,7-dithiol-7-helicene molecule. First, its molecular structure and components will be presented. The concept of measurement is introduced and the preparation of the sample is described. Afterwards, the correlation of the shift of the vibrational energies with the distance of the electrodes is investigated. Finally, the acquired results are compared with calculations.

4.2.1. Sample Preparation and Experimental Setting

Figure 4.10a illustrates the structural formula of the 1,7-dithiol-7-helicene (DHE) molecule. DHE consists of 7 phenyl rings, attached to each other by sharing one pair of carbon atoms. A screw like geometry emerges, having one winding with one overlapping phenyl ring. On both ends, a acetyl protected thiol group is attached (see Figure 4.10a), in order to ensure a covalent anchoring to the electrodes.

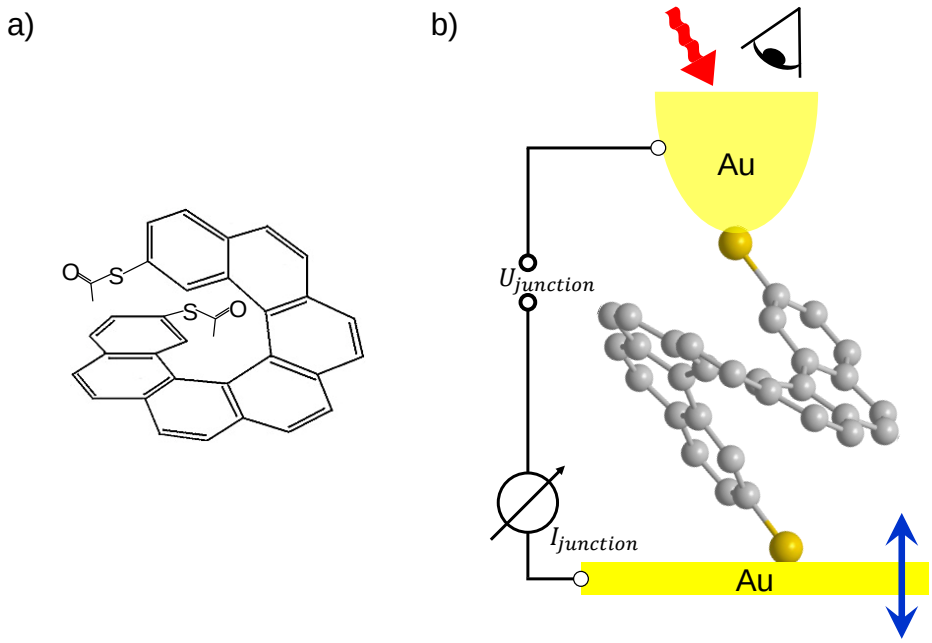

Figure 4.10.: Experimental configuration for DHE. a) depicts the structure of the molecule (1,7-dithiol-7-helicene). Adopted from [169]. b) illustrates the experimental configuration as well as the concept of measurement (blue arrow).

Figure 4.10b sketches the concept of the measurement. A DHE functionalized gold substrate and a gold-coated T-Tip was employed. As indicated by the red arrow and the eye in Figure 4.10b, Raman spectroscopy using the red laser was performed. Simultaneously, the junction

was formed. The formation of the junction can be monitored by the junction current. Formation of the junction first and subsequently retracting the substrate in small steps, as indicated by the blue arrow in Figure 4.10b, might cause a deformation of the electrodes as well as the application of stress on the helicene molecule.

The substrate was prepared, following the recipe, described in section 2.4.1. The molecule powder from the Ivo Starý group at IOCB Prague was dissolved in THF until the solution was saturated. The molecules were deposited on the substrate (4 droplets of ∼55 μl) which was rinsed afterwards.

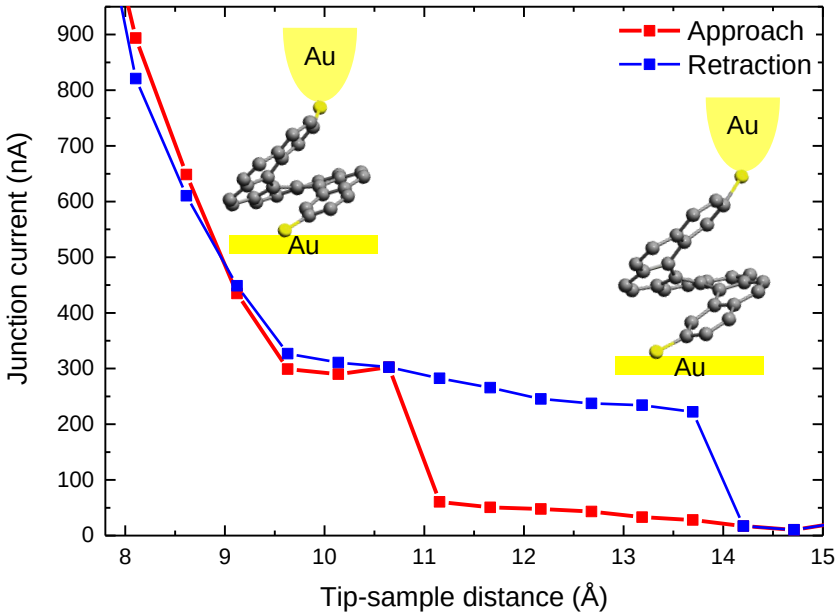

Figure 4.11.: Current-distance measurement of the DHE molecule at a junction voltage of 1.0 V.

At first, the molecules on the substrate were investigated by performing current-distance measurements, as described in section 3. The applied voltage was kept constant. The junction current was recorded and the piezo-voltage was increased or decreased simultaneously. It is possible to acquire the approaching as well as the retracting branch. It was investigated, how far a DHE junction, having a pristine length of about 10.5 Å (from DFT simulation), can be stretched by pulling with the electrodes.
Figure 4.11 depicts exemplarily one approach and one retraction curve, investigated at a junction voltage of 1.0 V. The tip was stepwise (0.26 Å)fully attached to the substrate and subsequently retracted in steps of 0.26 Å.
The approaching curve features a step, followed by a plateau at a tip-sample distance of ∼10.5 Å. The retraction curve shows a plateau, having a length of about 4 Å, up to a tip-sample distance of ∼14 Å, which occurs at a junction current of ∼280 nA. The two inset sketches in Figure 4.11 depict the molecule in the junction at the distance of 10 Å as well

as a stretched junction at the distance of 14 Å. The length difference between the occurring plateaus indicate a stretching of the DHE. The drop in the current at a tip-sample distance of ∼14 Å is due to the breaking of the junction. In contrast to the junctions investigated in section 4.1, the approach and retraction curves show a hysteresis behavior. This can be assigned to the stretching of the flexible DHE molecule.

As second step, the current-voltage behavior was examined. These measurements, performed on gold-DHE-gold junctions turned out to be difficult. In case of using the usual parameter set of ±1.5 V range and 200 steps, the junction broke at a voltage of ∼1 V. A reduced range to ±1.0 V patterned in 200 steps shows an nonlinear increasing tunneling current with the applied voltage. Neither in the current, nor in the differential conductance, any peaks or features can be identified. Consequently, the further focus was set on the Raman spectroscopy.

The blue curve in Figure 4.12 displays the observed Raman spectrum on a relaxed gold-DHE-gold junction biased by 0.1 V. Additionally, the DFT-simulated gas phase Raman spectrum is shown in red.

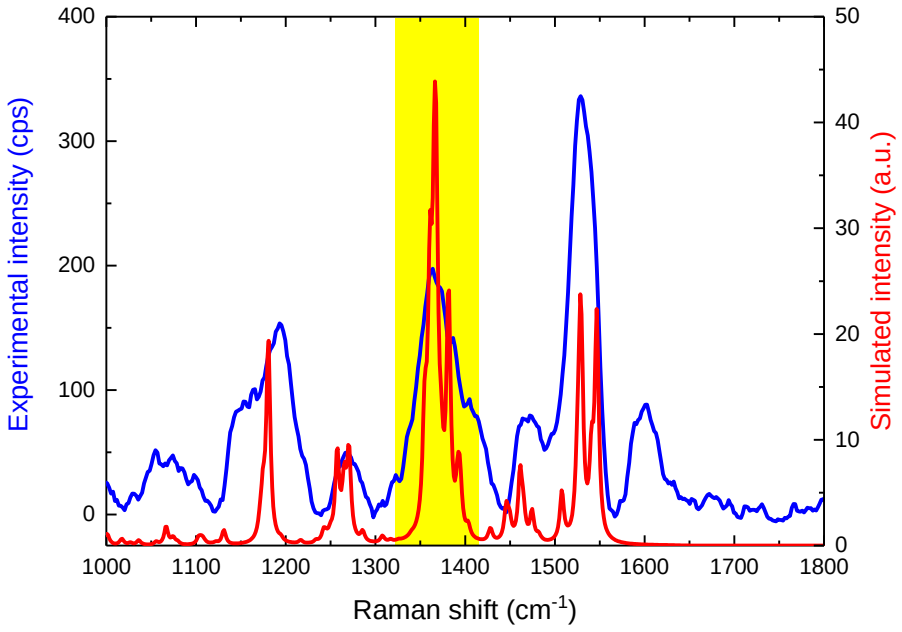

Figure 4.12.: Experimentally investigated (blue) and simulated (red) Raman spectra of DHE.

The experimentally observed spectrum is in good agreement with the calculated one. The different peak intensities could be explained by statistical fluctuations, typical for single-molecule spectroscopy.
The peak, located at 1362 cm^{-1} in the relaxed junction is systematically investigated in the next section. This peak was chosen, because it is the most intense one, according to simulation. The comparison of the shape of the simulated with the experimental spectrum indicates that

almost no contamination contributes to this peak, in contrast to the peak at 1550 cm^{-1}. Accordingly, the peak at 1550 cm^{-1} was observed in absence of DHE molecules too.

4.2.2. Stretching the Helicene

This section discusses the shift in the Raman spectrum in dependence of the applied mechanical stress in the molecule. In order to explain the change in the vibrational spectrum, DFT calculations have been performed for the DHE molecule.
The experimental approach to apply stress on the molecule is, to form the junction first and then slowly displace the electrodes, such that the tip-sample distance is subsequently increased. The widening of the gap is supposed to introduce stress to the molecule, bound to the electrodes. At a certain gap size, the stress is to high and the junction will break.

Figure 4.13 shows the measured Raman spectra in dependence of the relative electrode displacement. The experiment was performed by forming the gold-DHE-gold junction biased at 0.1 V first and afterwards increasing the tip-sample-distance in steps of 0.26 Å every ten seconds. Simultaneously, one full Raman spectrum at each step was acquired (integration time 10 s). The waterfall-plot (Figure 4.13) displays the investigated spectra, from the relaxed starting point in the back to the broken contact at the front.

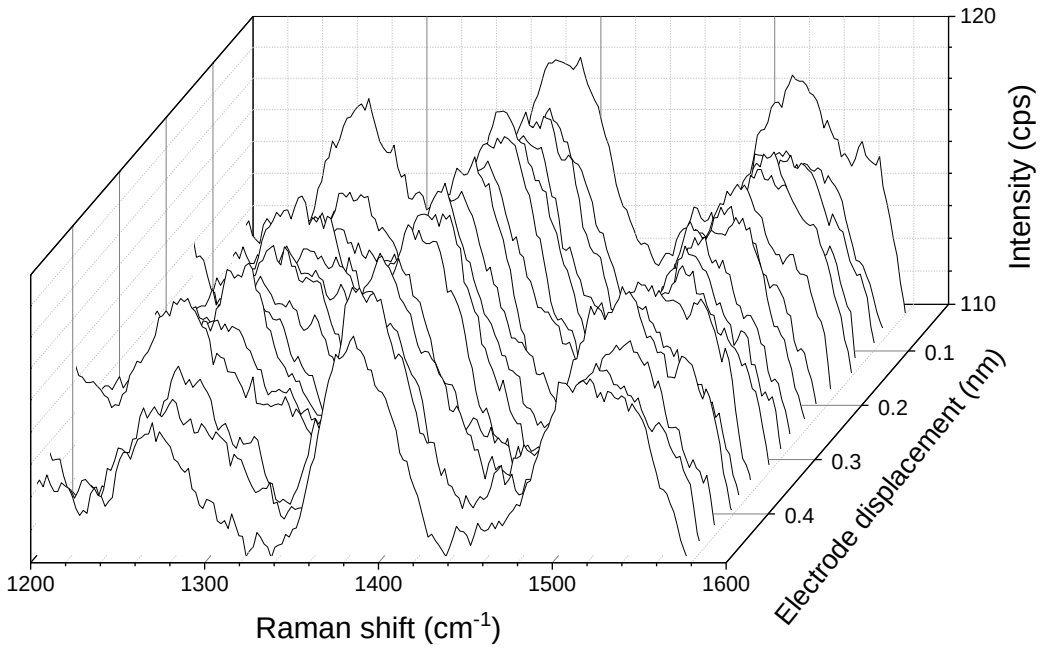

Figure 4.13.: Raman spectra as a function of the electrode displacement.

Due to the large noise level in comparison with the total intensity, no clear tendency can be directly deduced from the data in Figure 4.13. To suppress the effect of noise and to better

analyze the data, a Gaussian peak, with a center in the range between 1340 and 1400 cm^{-1} was fitted.

Figure 4.14 shows the fitted data in dependence of the electrode displacement.

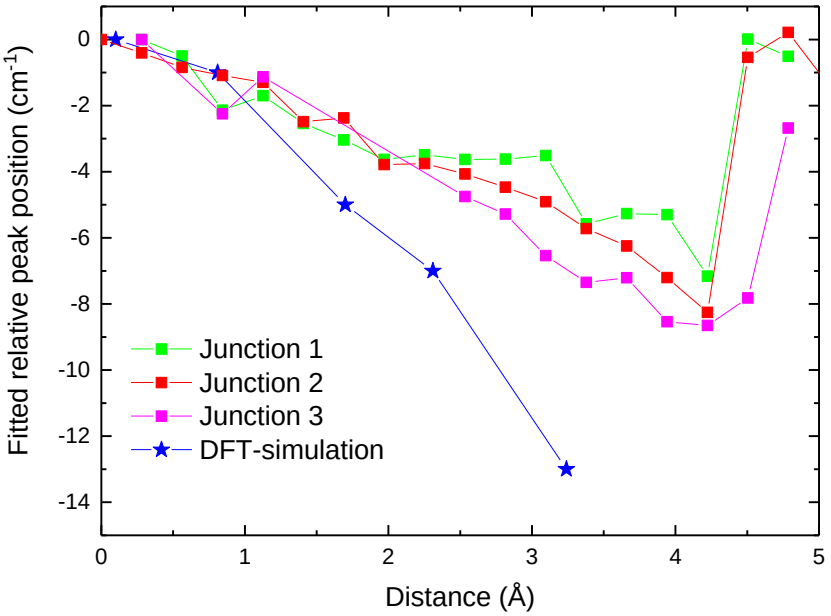

Figure 4.14.: Vibrational energy of the 1362 cm^{-1} mode in dependence of the electrode displacement.

Three different junctions were pulled from the initial length of the molecule, up to the breaking point of the junction. The three junctions reveal the same reduction of the vibrational energy with increasing tip-sample distance. This means that the vibrational mode becomes increasingly softer, with a larger electrode displacement.
The observed behavior was simulated by artificial stretching of the molecule. The stretching in the simulations has been implemented by adding a spatially fixed sulfur atom at each sulfur atom of the molecule. An additional sulfur was chosen, in order to form a non-polar, covalent bond to the fixed anchor. Afterwards, the geometry was optimized to the ground state, to determine the sulfur-sulfur length (10.5 Å). The molecule was subsequently stretched along the sulfur-sulfur axis up to a length of 13.6 Å in 4 steps. For each step, the geometry was again optimized to the ground state and the Raman spectrum was computed. The calculated peak at 1362 cm^{-1} was analyzed and is shown by the blue curve in Figure 4.14. The experimentally observed tendency as well as the calculated softening of the vibrational mode refers to the longitudinal atomic movement of this vibration. From literature, it is known that longitudinal modes show a softening with increasing stress [170–172].
Figure 4.14 also shows a jump in the peak position at a distance of ∼4.2 Å (0 Å is the pristine junction). At this point, the Au-DHE-Au junction breaks. According to literature [173, 174],

the gold-gold bond in the substrate or tip exhibits the weakest bond rupture force in this configuration. The breaking force of the junction can be determined to be ∼1.5 nN [55, 75, 175].

The slope of the simulated curve with respect to the experimentally observed ones fits for the first points well. Further electrode displacement (above ∼1 Å) leads to a drastic difference between the experimentally observed shift and the calculated one. This indicates a deformation of the electrodes. The stress on the junction does not correspond to the tip-sample displacement. The observed junction length increase (Figure 4.11 and Figure 4.14) of ∼4 Å contains the joint deformation of the leads and the molecule. The molecule cannot be stressed as much as the simulation allows, because of deformation in the gold electrodes and the gold-gold bond rupture force. By comparing the simulated shift with the experimentally observed one, a maximum molecule stretching of 2.5 Å is suggested.
The step-like behavior of the green curve in Figure 4.14 indicates a deformation of the electrodes too. The pulling of gold atoms out of the leads, having a diameter of ∼1.7 Å, fits well with the observed steps. Similar behavior was observed in break junctions (cf. 2.1) [176, 177]. The value of ∼2 Å fits to literature values for the stretching length of a gold-gold point contact [55] as well as the observed point contact length in the conductance quantization measurement (section 3.2).

In earlier investigations, the deformation of gold electrodes by pulling of a thiol-anchored molecule, which is bound to a gold surface, have been analyzed [174]. Following these investigations, we present a tentative picture for the present system: At the initial state, the DHE molecule is bound to the tip at the top and anchored to the gold surface at the bottom, as depicted in Figure 4.15a. The red colored atoms in Figure 4.15 represent the sulfur anchor atoms.

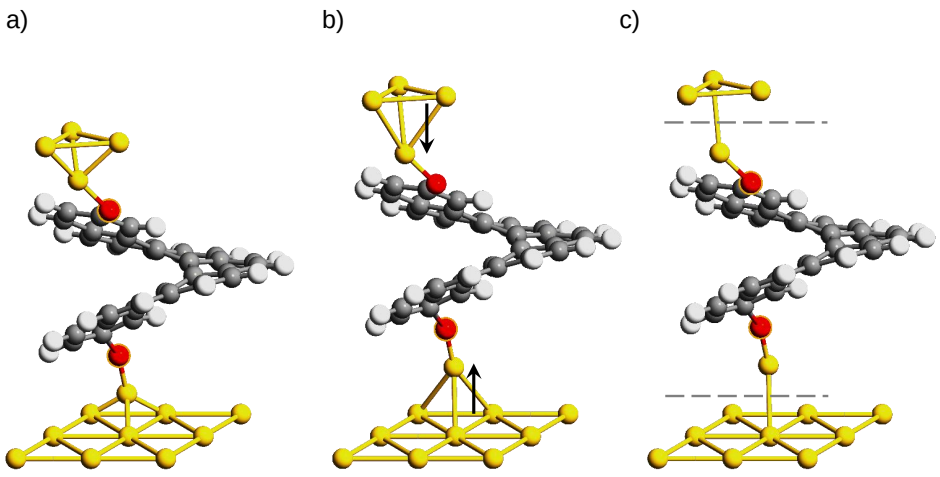

Figure 4.15.: Schematic of the stretching/ breaking of the junction (cf. [174]).

When stress is applied, gold atoms, forming the Au-thiolate bonds are pulled out of the surface, as illustrated by the arrows at the bottom and top of Figure 4.15b. This eventually results in single gold-gold bond formation for the gold atoms, anchored to the molecule. Such processes can occur at both electrodes, as sketched at Figure 4.15c. If the tip-sample distance is increased further, one of the gold-gold contacts at the bottom or top of the molecule breaks, as indicated by the dashed gray lines in Figure 4.15c.

This section reported a strain induced energy shift for a vibrational mode in a gold-DHE-gold configuration. The junction was established at a well-defined junction voltage and the electrode displacement was subsequently increased until the junction broke. At each point, a spectrum was acquired and the fitted peak position investigated. The resulting data, show a decreasing energy for the 1362 cm^{-1} mode with increasing stress.
From DFT simulations, the same tendency is suggested. By comparing the simulated and experimentally observed spectra, it is indicated that the molecule could be stretched by ∼20%. In order to learn more about the energy shifts, it is necessary to perform more experiments in a systematical way. The junction stressing needs to be performed at different voltages (positive and negative), the statistic has to be improved and other vibrational modes need to be investigated.

In the future, (sub-)monolayers of the DHE molecule could be used, to build touch sensitive devices, as described in [178]. It would be essential to grow monolayers in a highly controlled way on a gold functionalized flexible surface. The touch sensitivity might be realized by exploiting additionally the piezoelectric properties of the helicene [179].

4.3. Single-Molecule NDC

Negative differential conductance (NDC) describes the phenomenon of a decreasing current through a device with an increasing applied voltage. Therefore, the development of NDC devices might be important to improve the calculation speed of operations in electronics [196]. In the 1990s, the relevance of NDC devices, especially the NDC transistor for future electronic circuits has been shown by a patent from the Fujitsu Company [197]. NDC devices can be applied in logic grids, e.g. cross bar architecture [198] and for decreasing the memory size, by using a NDC device as three state logic bit. This results in a significant increased storage density. Furthermore, the speed of logic even-odd calculations will be improved by the possibility to perform logic decisions on a multi input level (> 2) [196].
In the last decades, molecular NDC devices, based on organic SAMs or single-molecules have been reported [199–203]. One of the first publications about a molecular NDC device was Chen [203]. Within one year, it turned out that the presented data does not represent the influence of the organic molecules [204]. In the following years the unambiguous occurrence of NDC devices at low temperatures was demonstrated [199–202, 205–207]. Until now, only a very few room temperature stable NDC devices are known [208–210].
Recent theoretical research has predicted the occurrence of NDC in ferromagnetic metal-molecule-metal heterostructures [211–213].

Here, the investigated system employs ferromagnetic electrodes in order to observe phenomena induced by magnetic properties at room temperature. First, the ferromagnet (nickel) - molecule - ferromagnet (nickel) junction geometry was measured. A negative differential conductance (NDC) at a certain junction voltage was observed. Furthermore, non-magnetic junctions, using the same molecular species were examined. The NDC was only observable, if at least one of the electrodes is a ferromagnet. A potential explanation for the observed NDC might be given by a single spin phenomenon, as discussed later (section 4.3.4).

4.3.1. Sample Preparation and Experimental Setting

Nickel is a reactive material, which is not suitable for thiol anchored molecules. This is due to the weakening of the carbon sulfur bond, becoming unstable at room temperature (cf. [214]). Even, if there are recipes reported [215–218], allowing the deposition of thiol-anchored molecules on nickel by the wet chemical approach, it was not possible to deposit a sub monolayer of intact molecules on the amorphous nickel film. The XPS measurements on these films revealed a high amount of organic contamination and a small amount of sulfide, but no thiolate signal. These results were reproduced by different approaches, using the TPD molecule. We started with the standard drop cast approach (see 2.4.1), followed by drop cast in inert nitrogen environment. The most complicated approach used a HCl cleaning and water rinsing before dipping the substrate into a saturated molecule solution (5 minutes) and rinsing by solvent afterwards in a dry nitrogen atmosphere. In the last approach, the parameter of the

HCl concentration, the amount of water rinsing, the molecule concentration in the solution as well as the amount of solvent rinsing were varied.

Consequently, different anchor groups needed to be employed. Therefore, molecules with carboxylic anchors were chosen. Figure 4.16a displays the fully symmetric molecule 4,4'-(1,2-ethynediyl)dibenzoic acid (EDA), bought from Sigma Aldrich.
From literature, it is well known that the carboxylic group deprotonates when the molecule

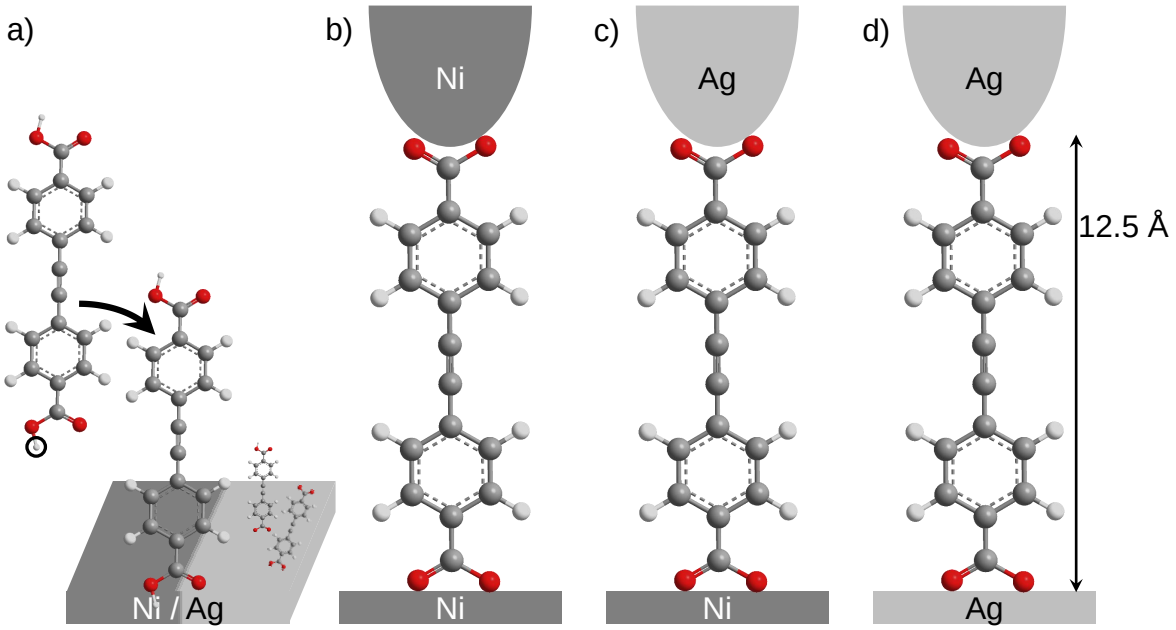

Figure 4.16.: Experimental configuration. a) shows the 4,4'-(1,2-ethynediyl)dibenzoic acid (EDA) molecule becoming deprotonated by binding to the substrate. b) displays the EDA molecule in a nickel-nickel junction. c) illustrates the silver-EDA-nickel configuration. d) sketches the non-magnetic case, using the EDA molecule anchored to a silver tip and a silver substrate.

binds to either nickel or silver [219]. Figure 4.16a shows the pristine molecule at the left side and the single deprotonated one already attached to a substrate at the right side. The EDA molecule features two carboxylic groups, used to anchor the molecule on both sides. Furthermore, the completely symmetric molecule exhibits two phenyl rings as well as a C-C triple bond as center of the molecule. A large delocalized π-electron system can be derived from the structure, resulting in a strong Raman intensity. The first investigated geometry is depicted in Figure 4.16b. A nickel coated T-Tip and an EDA functionalized nickel substrate were used. Second, a silver-coated tip replaced the nickel tip, in order to proof the influence of the ferromagnetic properties of the tip as well as to enhance the spectroscopic efficiency. Third, a completely non-magnetic system was used, consisting of a silver T-Tip, and an EDA functionalized silver substrate. The last geometry excludes every kind of magnetic effects, as demonstrated later (cf. Figure 4.16d).

The high reactivity of the nickel requires in-situ substrate cleaning and molecule deposition (cf. 2.4.2). The EDA molecule powder (99.8% purity) was mounted in a heatable crucible in UHV. Simultaneously, the substrate, 300 nm amorphous nickel (roughness of ∼20 nm) on glass, was transferred into the UHV chamber. The substrate was cleaned by argon sputtering at a pressure of $\sim 10^{-6}$ mbar, using a ion current of ∼10 μA for 15 minutes. Afterwards the cleanness of the substrate was confirmed by XPS.

The molecules were dosed on the clean substrate by heating the crucible up to 200 °C for 5 minutes. A sub monolayer of EDA molecules was deposited on the nickel substrate, as confirmed by XPS. Figure 4.17 displays the XPS spectra of the cleaned and EDA functionalized nickel substrate.
Figure 4.17 illustrates the spectrum, belonging to the nickel $2p_{2/3}$ states at a binding energy of ∼850 eV. The blue curve depicts the photoelectron spectrum of the cleaned (sputtered) substrate, which shows the highest peak at 852.7 eV, fitting nicely the literature value for the $2p_{3/2}$ of clean nickel [131]. The red curve in Figure 4.17 reveals the XPS spectrum of the EDA functionalized nickel, where the main peak stayed at the position of 852.7 eV. The small reduction of the peak (∼15%) indicates that the surface is only partially covered. In case of a larger coverage, one would expect a shift to 853.8 eV due to the chemical binding of the molecules to the surface nickel atoms [131].

Figure 4.18 displays the carbon 1s spectrum of the clean (blue) and the functionalized (red) nickel substrate. The blue line in Figure 4.18 shows only a tiny peak at 283.5 eV, which could be due to implanted carbon atoms in the nickel film, caused by the fabrication method. The low intensity of this peak still allows the conclusion that the substrate is reasonable well prepared. The red curve in Figure 4.18 shows the carbon 1s spectrum of the EDA functionalized substrate. The most remarkable feature is the peak shoulder at 287.5 eV (green fit and dotted black line), which can be clearly assigned to the carbon atom of the carboxylic group of the molecule, according to literature [220].

Figure 4.19 displays the oxygen 1s photoelectron spectrum. The blue curve shows the cleaned substrate. The peak at 530 eV is due to gathered oxygen in the nickel film during the EBPVD process and could not be decreased by further cleaning. This peak is even present in the EDA functionalized case (red curve). By subtracting the blue curve from the red one, the corrected EDA signal emerges (depicted in green). The main peak of the green curve at 531.2 eV corresponds to a carboxyl group, binding with both oxygens to the nickel, according to literature [219]. The peak shoulder (532.0 eV) matches to the oxygen in a pristine carboxylic group [189, 219]. From literature, it is well known that the carboxylic group of the molecule deprotonates upon adsorption to the nickel surface [219], as depicted in Figure 4.16a. It can be concluded that the EDA molecule can be deposited in a highly controllable way on nickel substrates, using the evaporation method described in section 2.4.2. Furthermore, we infer that at least some of the molecules may not be bound on both sides to the substrate. The thickness of the EDA layer on nickel can be roughly estimated to be about 0.1 ML, which turned out to be a good value for single-molecule investigations (cf. section 4.1).

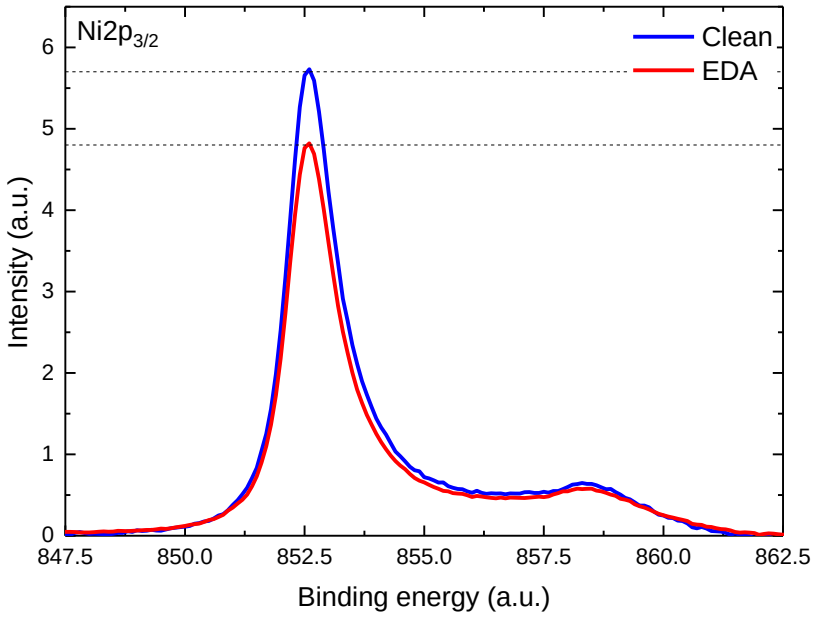

Figure 4.17.: X-Ray photoelectron spectra of nickel $2p_{2/3}$ states. The blue line depicts the clean substrate, whereas the red line represents the EDA functionalized substrate.

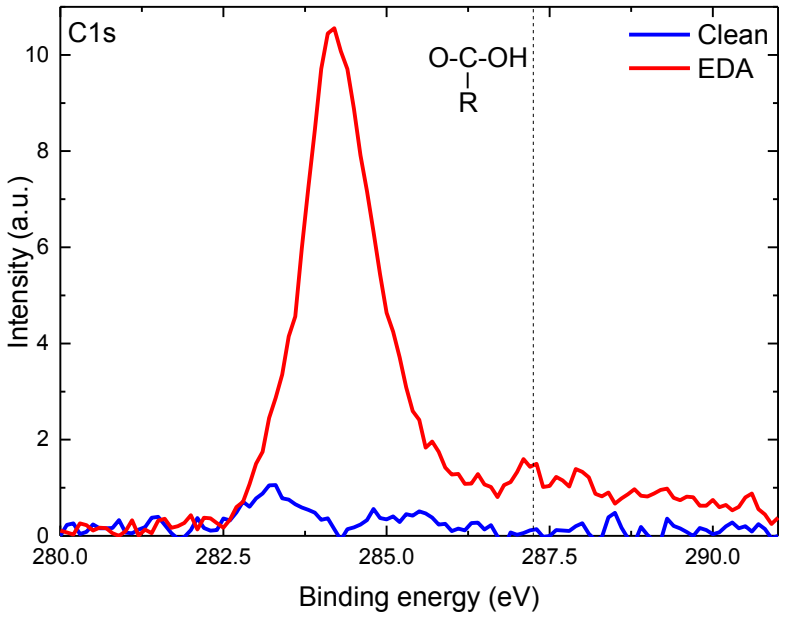

Figure 4.18.: XPS spectra of the carbon 1s states. The blue line shows the cleaned, sputtered substrate. The red line illustrates EDA functionalized substrate.

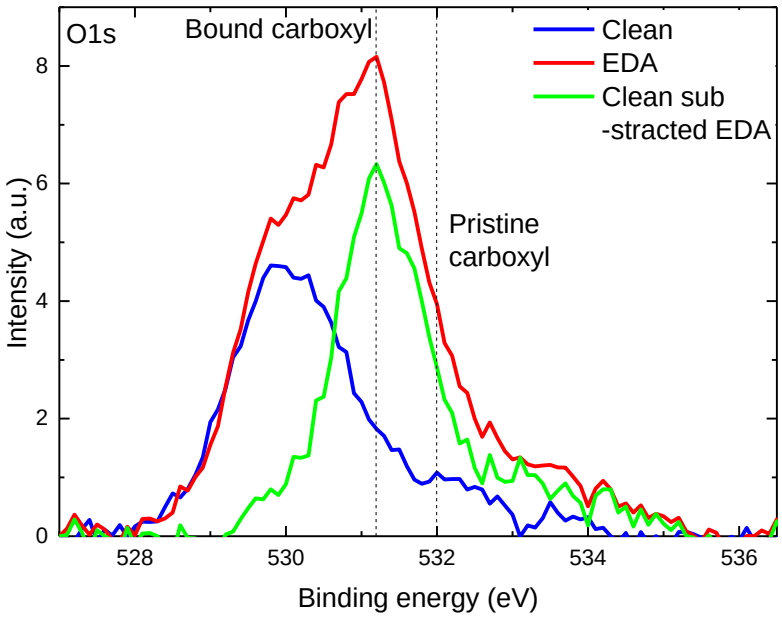

Figure 4.19.: XPS spectra of oxygen 1s states. The blue line displays the spectrum of the "clean" substrate. The red line shows the corresponding measurement on the EDA functionalized substrate. The green curve represents the EDA curve, which is subtracted by the clean signal.

In order to perform non-magnetic control measurements, a second substrate, using EDA molecules was prepared. This time a silver film on glass was employed with the drop cast standard recipe, as already described in section 2.4.1 and section 4.1.1. Thus, no XPS check of the substrates was performed, especially, because the presence of molecules on the surface could be probed by Raman-spectroscopy, as described in section 4.3.3.

The molecules on the substrate can be investigated by performing current-distance measurements. The applied voltage is kept constant while the piezo-voltage is ramped up, in order to reduce the tip-sample distance and the junction current is recorded, as described in detail in section 3.5
Figure 4.20 depicts current-distance profiles, on the EDA functionalized nickel (left side) as well as the silver substrate (right side). Both current-distance characteristics were extracted by analyzing several selected approach curves from subsequent measurements.

For the case of Ni, the applied junction voltage was fixed at 1.0 V. At a tip-sample distance of about 1.1 nm (from full metallic contact), a step in the current occurs, which is followed by a plateau. This step is due to the formation of a molecule junction, as explained in section 4.1. The occurring plateau shows a current of ∼28 nA. The step position fits well to the simulated size of the EDA molecule (12.5 Å). It can be concluded that it is possible to form a single-molecule junction, using an EDA functionalized nickel substrate and a nickel-coated T-Tip.

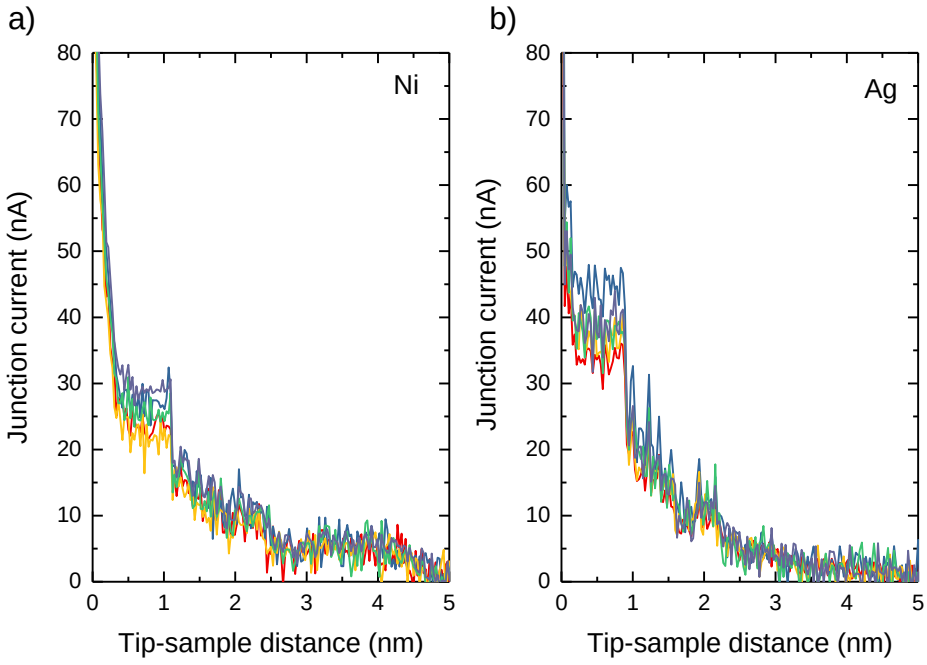

Figure 4.20.: Five subsequent approach curves for the EDA molecule of each geometry. a) shows the current-distance characteristics of Ni-EDA-Ni junctions. b) depicts the approach curves of Ag-EDA-Ag junctions.

Figure 4.20b shows the result of several current distance measurements acquired at 1.0 V junction voltage with silver-EDA-silver junctions. Similar to Figure 4.20a an exponential behavior is observed. The plateau, occurring in Figure 4.20b shows a current-level of ∼40 nA, which is significantly higher than in the nickel-EDA-nickel geometry. The length of the investigated plateau in the silver geometry (Figure 4.20b) is similar to the one of the nickel geometry. This allows to infer that for both geometries it is possible to form single-molecule junctions.

4.3.2. Negative Differential Conductance Observed in a Ferromagnetic Single-Molecule Junction

The nickel-EDA-nickel geometry, as depicted in Figure 4.16b was investigated first, in order to obtain the magnetic influence of electrodes on the EDA molecule. The following section presents current-voltage measurements of several different junctions, whereas the shown Raman spectra are obtained in a row from one junction.

First, the junction current as a function of the junction voltage is plotted. Figure 4.21 depicts six current-voltage-characteristics of three different junctions. The red curves illustrate the investigated junction current, measured at 200 discrete voltage levels. The blue curves in Figure 4.21 depict the derivative of the junction current, the differential conductance.
At a junction voltage of -1.0 V, a drop of ∼15% in the junction current was observed, as marked

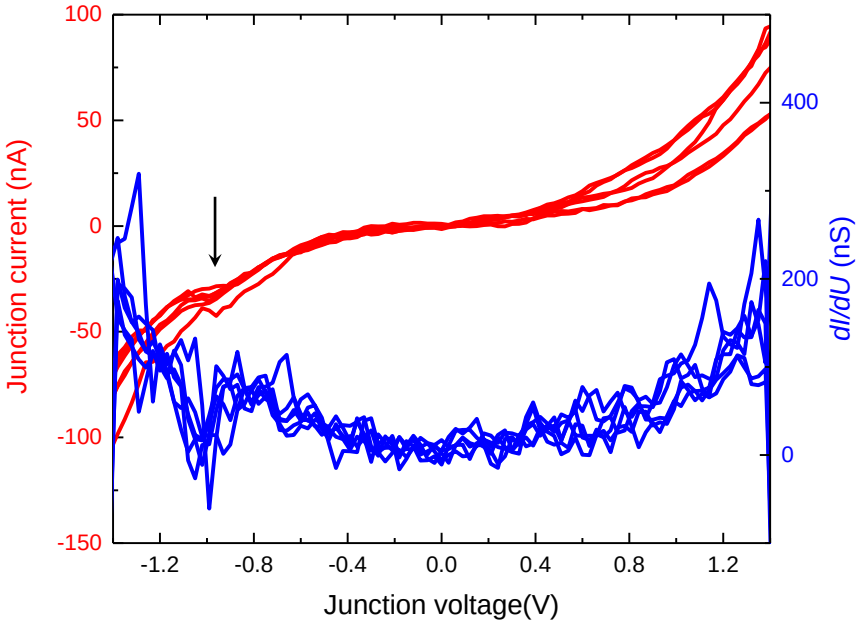

Figure 4.21.: Current-voltage characteristics of Ni-EDA-Ni junctions. The red curves illustrate the junction current as a function of the junction voltage. The blue curves show the corresponding differential conductance.

by the arrow in Figure 4.21. The corresponding differential conductance at the voltage level of -1.0 V decreases to negative values, as displayed by the blue curves in Figure 4.21. In contrast to the system investigated in section 4.1, the current-voltage measurements exhibit an asymmetry.
A potential explanation for the observed negative differential conductance will be discussed in detail later. At one of the junctions, investigated in Figure 4.21, Stokes Raman spectroscopy was performed. By varying the junction voltage, two different species of Raman spectra were observed. The optical/ plasmonic properties of nickel and silver require the use of the green laser, because the excitation wavelength of 532 nm fits the band edges of nickel and silver [105, 221] better than the red laser (633 nm).

Figure 4.22 illustrates the two different species of the experimentally acquired spectra (red and blue). The red spectrum was observed, if the junction was biased above -1.0 V, the blue spectrum was measured below this threshold. The most remarkable difference between the two species is the peak at a vibrational energy of 2271 cm^{-1} (red curve), which shifts to a value of 2187 cm^{-1} (blue curve). The atomic movement of this vibrational mode is, according to simulations, the C-C triple-bond stretch mode, as indicated by the arrow, close to the molecule drawing in Figure 4.23.

The peaks at a Raman shift of $\sim$1550 cm^{-1} and $\sim$1345 cm^{-1} which stay almost constant with the junction voltage, could be due to contamination and are also observed when unfunctionalized substrates (without molecules) are investigated. The contaminations origin is most likely in

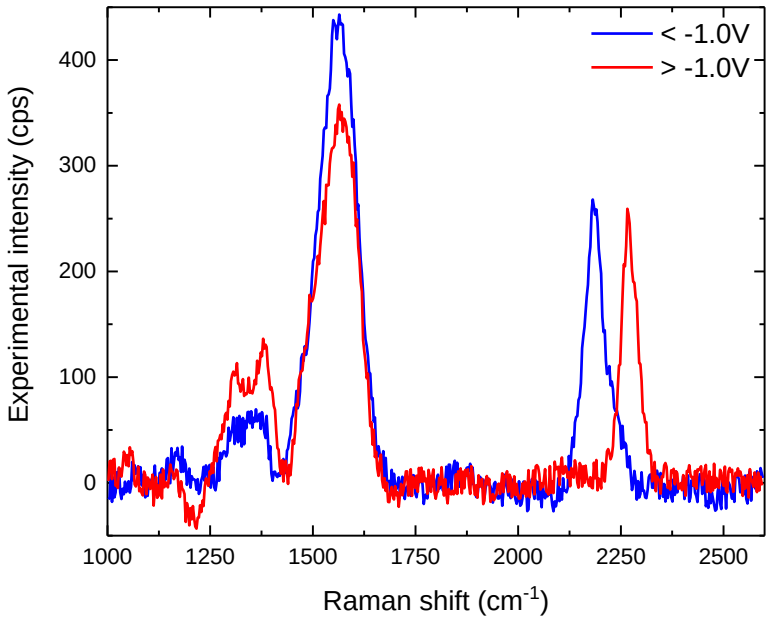

Figure 4.22.: Experimentally investigated Raman spectra of EDA. The blue and red curves show the two different species of acquired EDA spectra for different bias voltages.

the fabrication process of the T-Tip. Here, the exposure to ambient conditions by dissecting the glass fragments as well as mounting the uncoated tips in the EBPVD machine might cause the absorption of aromatic organic contaminants. The vibrational energy of ∼1550 cm^{-1} is, according to simulations assignable to the breathing mode of phenyl rings. This means, the contamination exhibits a similar vibrational structure as the investigated molecules, but the triple-bond vibrational mode at 2271 cm^{-1} is unique. This mode is only observable, if an EDA functionalized substrate was investigated.

Figure 4.23 displays the two species of experimentally investigated peaks at ∼2200 cm^{-1},being the most remarkable feature of the acquired Raman spectra. The change of the spectral pattern indicates a junction voltage influenced modification of the charge state of the molecule (similar to 4.1).

The dark blue, purple, cyan, black and green curves in Figure 4.23 display the simulated Raman spectra for different charge states. The neutral, the +1, -1, +2 and -2 charge states were simulated by DFT (see 2.3).The charged states were achieved by removing one or two electrons from the HOMO, respectively adding one or two electrons to the LUMO. It can be seen from the peak position of the simulated curves that the neutral one (dark blue) fits best to the red curve, representing the unbiased measurements. From the peak intensity and the peak position of the ∼2200 cm^{-1} peak it is clear that the simulated spectrum for the +1 state (cyan colored spectrum in Figure 4.23) fits the experimental data below -1.0 V (blue curve) best. The comparison of the -1 state simulated spectrum (magenta curve) with the

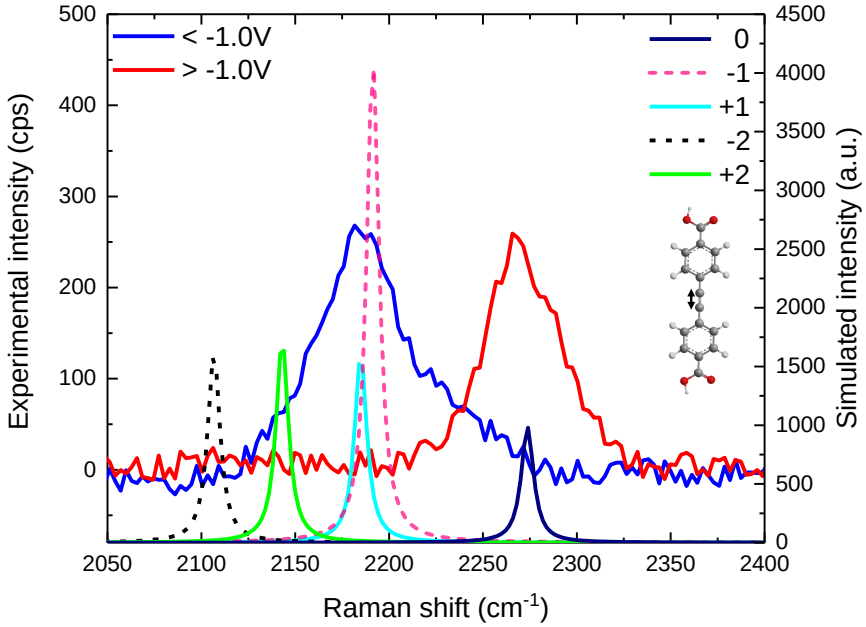

Figure 4.23.: Simulated and investigated Raman spectra of EDA. The blue and red curves show the experimentally investigated intensity of EDA for different bias voltages. The dark blue, magenta, cyan, black and green colored curves depict the simulated Raman spectra for different charge states of the molecule.

blue curve in Figure 4.23 reveals that the peak position at ∼2190 cm^{-1} fits, but the intensity is to large in respect with the uncharged species. It can be concluded that the molecule remains uncharged as long as the junction voltage is above -1.0 V. Below this threshold, the EDA molecule becomes +1 charged.

To investigate the voltage dependence of the Raman measurements in further detail, the junction voltage was swept in discrete steps of 0.05 V in a range from -1.5 to 1.5 V. A two dimensional color map plot, illustrating the Raman intensity as a function of the junction voltage, is shown in Figure 4.24.

From Figure 4.24 it is obvious that the experimentally observed Raman spectrum reveals the same intensity and shape, as long as the junction voltage is not exceeding the threshold of -1.0 V. The spectrum changes step-like from one behavior to another at this level. The step-like change is most present for the peak at 2281 cm^{-1}, respectively 2187 cm^{-1}. The intensity of the peaks at 1550 cm^{-1} and 1380 cm^{-1} changes, according to Figure 4.24, which indicates that vibrational modes of the molecule are contributing to that peak. It can be concluded that applying a junction voltage below -1.0 V results in a current drop of ∼15%, which is accompanied with the change of the molecular charge state.

In the following, it was investigated how this effect is affected by the magnetic electrodes. Therefore, the nickel coated T-Tip was substituted by a silver coated T-Tip.

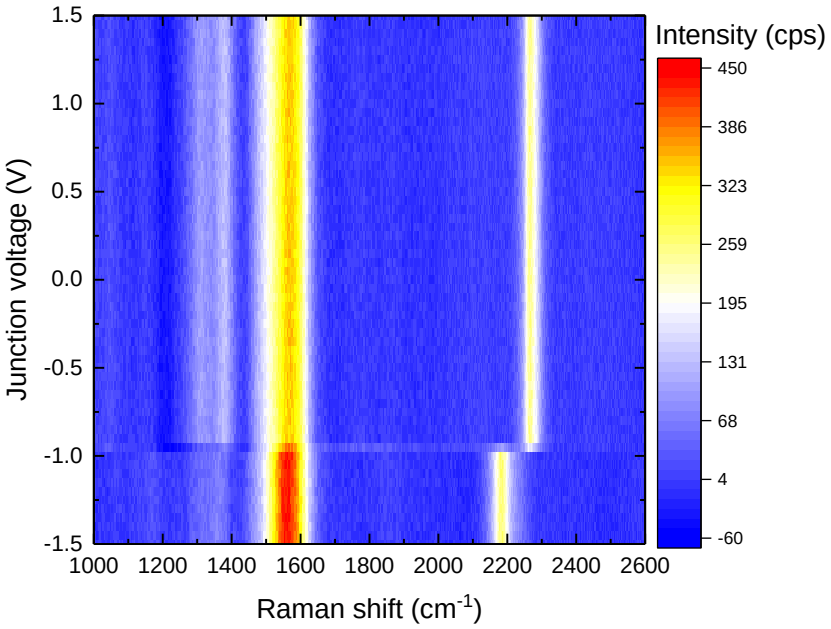

Figure 4.24.: 2D color map plot, illustrating the Raman intensity as a function of the applied junction voltage.

Figure 4.25 displays the current-voltage measurements, performed on five different junctions on the EDA-functionalized nickel substrate, using a silver-coated T-Tip as counter electrode. The red curves represent the junction current, measured in 200 equally distributed discrete voltage levels between -1.5 V and 1.5 V, similar to the measurements shown in Figure 4.21. The blue curve in Figure 4.25 depicts the corresponding differential conductance.

In accordance with the previous measurement, a current drop of about 15% occurs at a voltage level of -1.0 V, which is marked by the arrow. The corresponding differential conductance decreases to negative values too. In agreement with the measurements performed in the nickel-EDA-nickel geometry, the voltage drop, investigated at the silver-EDA-nickel configuration is asymmetric and located at the same junction voltage. Thus, the observed negative differential conductance does not seem to be influenced by the magnetic properties of the used T-Tip.

The optical properties of silver allows performing Raman spectroscopy too. Silver exhibits a slightly higher band edge than nickel, which fits the excitation laser energy better [105, 221]. Additionally, the plasmonic propagation length is higher in case of silver [222, 223]. This results in a slightly higher enhancement, achieved by the T-Tip geometry, in comparison to the nickel-coated T-Tip. This effect is accompanied by the increase of the collection area on the tip (larger plasmonic propagation length). As in the Ni-EDA-Ni case, the junction voltage was varied and Raman spectroscopy was performed at 60 equally distributed voltage levels in the range between -1.5 V and 1.5 V. The data is shown in the 2D color map plot in Figure 4.26.

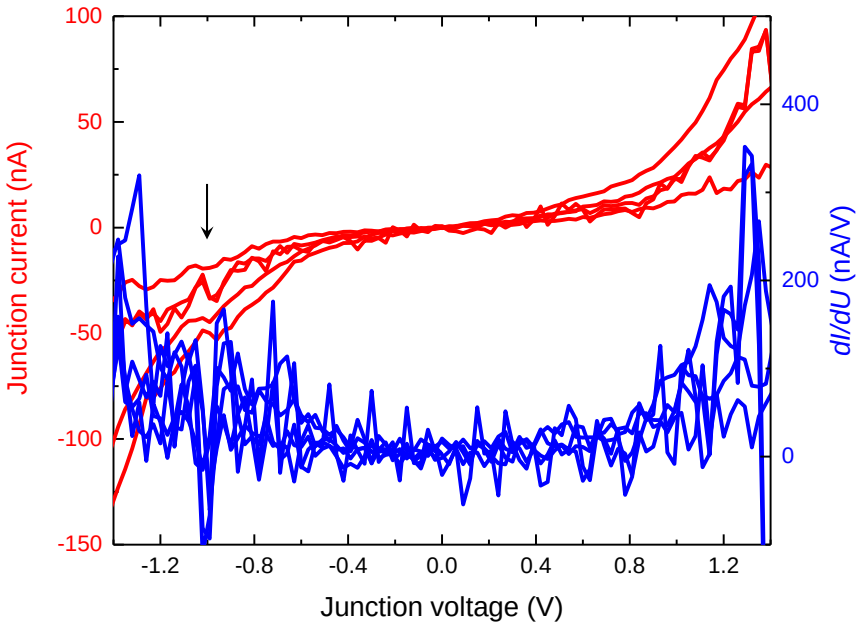

Figure 4.25.: Current-voltage characteristics of Ag-EDA-Ni junctions. The red curves illustrate the junction current as a function of the junction voltage. The blue curves show the corresponding differential conductance.

At the threshold of -1.0 V the Raman spectrum changes, nicely fitting to the observed current drop, depicted in Figure 4.25. The positions of the Raman peaks stay at the same energies even after changing from nickel to silver as coating material of the T-Tip. The C-C triple bond peak for the neutral species, observed at 2281 cm^{-1} (cf. Figure 4.24 and 4.26) exhibits an absolute intensity of ∼250 cps for both geometries and remains clearly identifiable. Nevertheless, the peak at a Raman shift of 1550 cm^{-1} reveals a significantly higher count rate in case of using a silver-coated T-Tip.

The larger collection area, due to the better plasmonic properties of silver, introduce more influence of surrounding contamination. The state of the molecule at junction voltages below -1.0 V can be assigned again to the positive charge state, because the Raman spectrum fits the positive state DFT-simulation best, as in the case of the nickel-coated tip (cf. Figure 4.23).

Using both kinds of T-Tips (nickel and silver), a change at -1.0 V was observed in the optical measurements as well as the negative differential conductance. Summarizing, the coating material of the T-Tip, does not play a role, for the occurrence of the NDC as well as its voltage level. Consequently, the appearance of the NDC must have something to do with the EDA-Ni configuration.

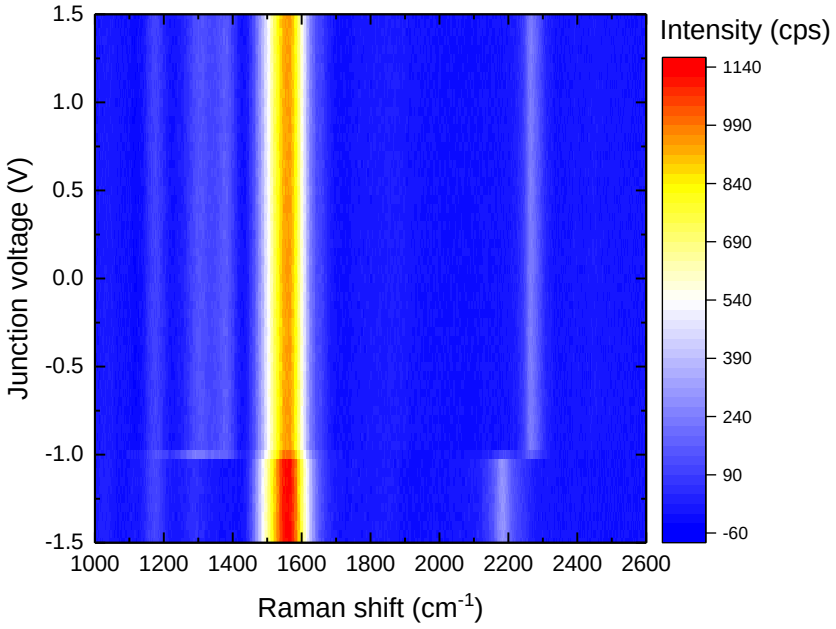

Figure 4.26.: 2D color map plot, illustrating the Raman intensity of the Ag-EDA-Ni geometry as a function of the applied junction voltage.

4.3.3. Non-Ferromagentic Junction

Suppressing any effects of the magnetic substrate, the EDA-functionalized nickel substrate was changed to an EDA-functionalized silver substrate. The new substrate was prepared, by the drop cast method (cf. section 2.4.1) on a thin silver layer (∼300 nm) on a glass slab, as described in section 4.3.1. As counter electrode, again a silver-coated T-Tip was used. After ensuring that a single-molecule junction has formed (Figure 4.20b), current-voltage measurements on the silver-EDA-silver geometry (depicted on the right side of Figure 4.16) were performed.

Figure 4.27 displays the junction current of three different junctions in dependence of the applied junction voltage (red curves) as well as the corresponding differential conductance (blue curves) for several different junctions.

The current-voltage measurements (red curves in Figure 4.27) reveal a symmetric step-like increase of the current at the voltages of ±0.6 V. The step-like increase of the current, arising from the opening of a new transport channel through one of the molecules orbitals (cf. 2.1), causes a peak-like feature in the corresponding differential conductance (blue curves in Figure 4.27). Due to the symmetric coupling to the electrodes, a symmetric alignment of the molecular orbitals between both electrodes can be assumed, similar to the system investigated in section 4.1. The preparation procedure for the tip and the substrate has been the same. The only different step is the additional wet chemical treatment for the molecule growth on

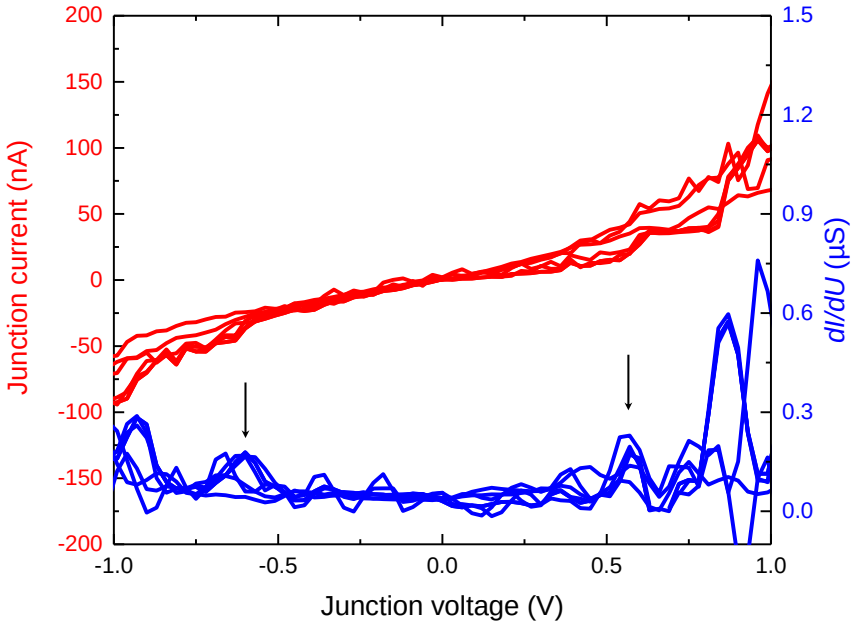

Figure 4.27.: Electric properties of non-magnetic EDA junctions. The red curves illustrate the junction current as a function of the junction voltage. The blue curves show the corresponding differential conductance.

the substrate. At this step, no further oxidation of the (relatively inert) silver surface occurs. The observed junction current of ∼37 nA at a voltage of 1.0 V (red curves in Figure 4.27) is consistent with the observed plateau current in the current-distance measurements (cf. Figure 4.20b).

In addition to the current-voltage measurements, Raman spectroscopy was performed. The investigation of the silver-EDA-silver junctions revealed two distinct Raman spectra, as observed before. The red and the blue curve in Figure 4.28 depict the experimentally observed species. The threshold for changing between the two kinds of spectra is at ±0.6 V. The dashed pink and dashed black curves in Figure 4.28b represent the calculated spectra of the -1, respectively the -2 charge state of the molecule.

The cyan colored and green colored lines are the simulated Raman spectra, assigned to the positively and double positively charge state of EDA. The dark blue colored graph shows the DFT-computed Raman-pattern of the EDA molecule for the neutral state.

Consistent with the experimental data and the simulated ones in section 4.3.2, the dark blue curve (neutral molecule) in Figure 4.28b achieves the best fit to the unbiased spectrum (red curve). The spectrum, investigated at a junction voltage of 0.6 V (blue curve in Figure 4.28b) shows the best agreement with the simulated spectrum for the single positively charged state (cyan curve), according to the intensity and the position of the peak at 2187 cm^{-1}. The peak at ∼1550 cm^{-1} is again potentially influenced by contamination.

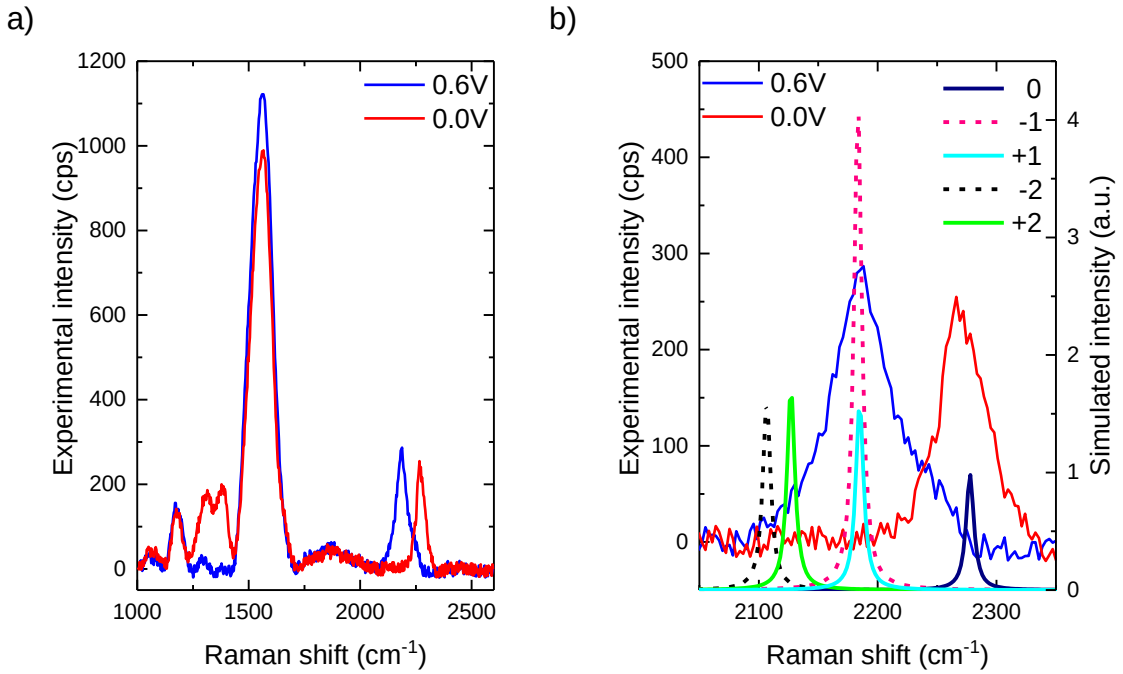

Figure 4.28.: Investigated and calculated Raman spectra of the Ag-EDA-Ag geometry. The blue and red curves sketch the experimentally investigated intensity of EDA on silver for different bias voltages. b) depicts in addition the simulated curves (dark blue, magenta, cyan, black, green colored).

Between silver electrodes, the molecule seems to change its charge state, which can be observed in the electrical characterization as well as in its Raman response.

Figure 4.29 displays the Raman spectra as a function of the applied junction voltage. The junction voltage was varied in the range between -1.5 V and 1.5 V in 60 steps of 50 mV. The peak assigned to the C-C triple bond stretch mode (2271 cm^{-1}) changes its position at a threshold voltage of ± 0.6 V, as depicted in Figure 4.29. The dominant peak, located at a Raman shift of 1550 cm^{-1} changes its intensity by about 100 cps. Here, the similarity to the measurement of the Ag-EDA-Ni geometry, depicted in Figure 4.26 is clearly recognizable. The main difference is the arising symmetry, in respect to the junction voltage, which could be explained by the symmetric coupling due to the sample preparation.

4.3.4. Potential Explanations for the Observed NDC

The following section outlines possible explanations for the observed phenomena. At first, the already known case for non-magnetic electrodes [48, 160] is discussed. Figure 4.30a depicts a schematic drawing of the observed current-voltage characteristics. The left part, which is labeled as neutral, exhibits a nonlinear increase of the current with the voltage. This is the standard behavior for a tunneling current, as known from literature [224]. The nonlinear behavior is indicated by the dashed black graph in Figure 4.30a, which represents the direct

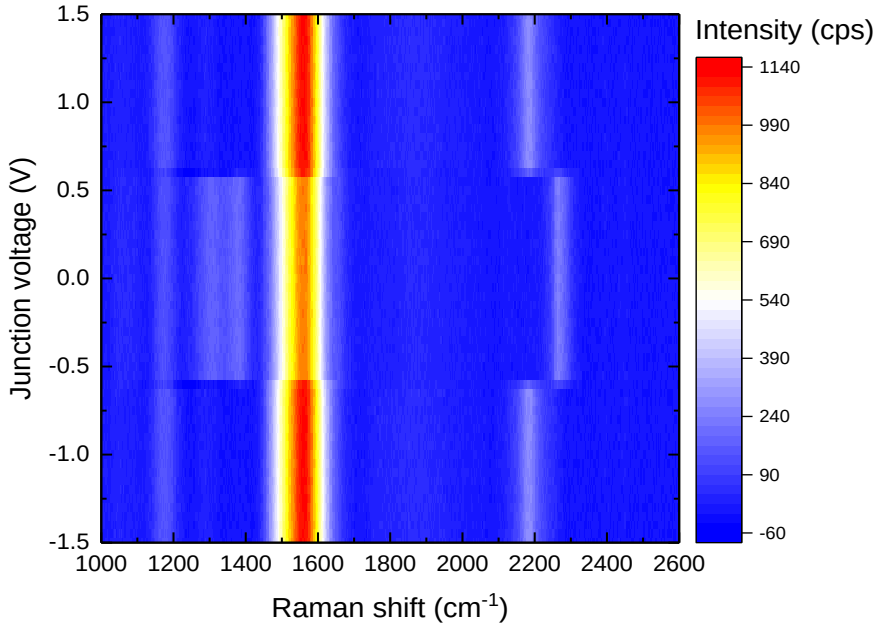

Figure 4.29.: 2D color map, showing the investigated Raman intensity (Ag-EDA-Ag junction) as a function of the bias voltage.

tunneling current through the molecule. This dependence is experimentally observed, as long as no molecular orbital is involved in the transport. Figure 4.30b depicts the level diagram for the neutral molecule, indicating that this behavior is observed in the HOMO-LUMO gap region [225]. The Fermi levels (μ_L and μ_R) shift symmetrically with respect to the molecular levels, when a voltage is applied. The symmetry arises due to the symmetric binding conditions on both sides (molecule deposition on natively oxidized silver and use of a natively oxidized silver T-Tip). As long as none of the electrode levels is aligned with the HOMO, it stays fully occupied. Some electrons can directly tunnel from one electrode to the other, passing through the EDA molecule.

The dashed green line in Figure 4.30a is a step function, indicating the current contribution of the HOMO by transport through the orbital (cf. 2.1). As soon as the bias voltage reaches the dashed line, μ_L is aligned with the HOMO of the molecule. An electron can hop to the electrode. Thereby, a process of depopulating and repopulating the orbital is started. The experimentally observed charge state of +1 could indicate that the molecule is single positively charged most of the time. This allows the assumption of larger repopulation time constants than the depopulation ones. Theoretically, the second electron might also hop off and the HOMO would depopulate completely. This is experimentally not observed. A potential explanation might be the hindering by a shift of the levels due to the coulomb blockade.
The direct tunneling current is still present, but the additional small current, due to the transport through the single depopulated HOMO is added, as illustrated by the small blue-red-

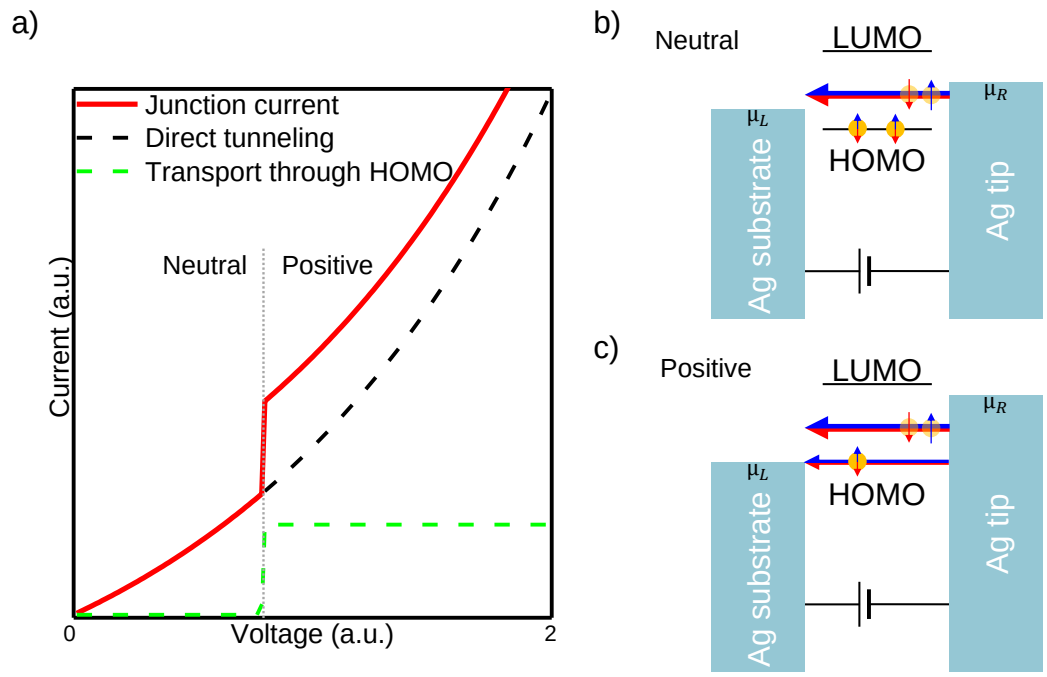

Figure 4.30.: Schematic transport picture through a non-magnetic junction. a) depicts the nonlinear tunneling current in black, the estimated current through a molecular orbital in green and the resulting sum and observed current in red. b) sketches the level diagram for the direct tunneling through the molecule (gap region). c) shows the level diagram for the HOMO, being aligned with an electrode level, resulting in depopulation of the HOMO and in a current through the orbital.

colored arrow in Figure 4.30c. The total junction current increases step like at the threshold voltage, as displayed by the red line in Figure 4.30a.

In summary, non-magnetic junctions reveal a nonlinear tunneling current and show a step like increase at a certain threshold voltage. This is expected (see 2.1) and observed, as depicted in Figure 4.30 and 4.27. The occurring charged state could be identified by the systematic comparison of the acquired Raman spectra with the simulated ones, as illustrated in Figure 4.28. The (electrically and optically) observed symmetric behavior suggests a symmetric coupling of the EDA molecule to the tip and the substrate.

In case of using the EDA functionalized nickel substrate and a nickel coated T-Tip, the coupling to the electrodes can be asymmetric. The EDA molecules were deposited on a clean, non-oxidized, surface in UHV. This means that the molecules are bound to a pure (metallic) nickel surface, whereas the bond formation to the tip happens on a natively oxidized surface, potentially leading to asymmetric tunneling barriers on both sides of the molecule as well as an asymmetric pinning of the molecular orbitals. The stronger coupling to the substrate is indicated by the smaller barrier between the molecule and the substrate in Figure 4.31b and c. If a voltage is applied, the oxide layer reduces the effective potential drop on the molecule by its insulating properties. The Fermi levels of the electrodes (μ_{L} and μ_{R}) shift asymmetrically in

respect to the molecular orbitals. The use of a non-magnetic tip (silver) reproduced the same results as the nickel-coated tip. This indicates that the native oxide passivation layer on silver is already thick enough that the level pinning to the substrate stays dominant, respectively the tunneling barrier between molecule and tip is larger than the one between tip and substrate. Due to the similarity of the acquired data for the nickel and silver-coated T-Tip, the magnetic properties of the tip seem to be of no importance.

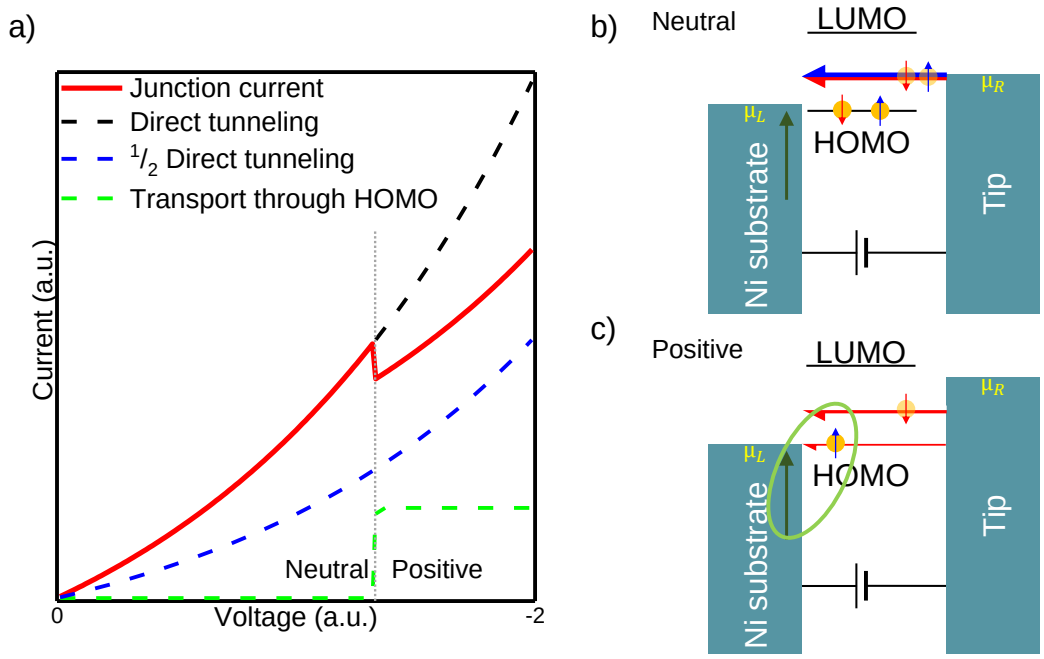

Figure 4.31.: Schematic for the transport mechanism through a molecule in a ferromagnetic junction. a) polarity flipped estimated current-voltage dependence (0 to -2). The direct tunneling current is depicted in black, half of the direct tunneling current in blue, the current through a molecular orbital in green as well as the resulting sum and observed current in red. b) sketches the level diagram for the direct tunneling through the molecule (gap region). c) shows the level diagram for the HOMO, being aligned with an electrode, resulting in partial depopulation of the HOMO.

According to literature [226], s- and p-states reveal a larger expansion in space, than the d-states, meaning that tunneling mostly relies on the s- and p-states. Figure 4.32a displays the cumulative density of states of the nickel s- and p-states. It can be easily recognized that the calculated DOS exhibit only a very small spin polarization, which is in accordance with the calculations of Emberly et al. [227]. Thus, no spin-polarized current is expected, since the tunneling current is carried by the s- and p- states of the electrodes.

One potential explanation that comes into mind is that spin polarization of the current from the electrodes leads to a Tunneling Magneto Resistance (TMR) configuration [84]. This can be excluded, because the tunneling current is per se not spin dependent/ polarized. Additionally the non-blocking configuration expected for TMR, which would show an step-like increase in

the current was not observed (parallel aligned spins). Another potential mechanism might be the formation of a spin valve.

At low bias voltages is depicted in Figure 4.31b and is similar to the non-magnetic case. Here, the molecular orbitals stay mainly pinned to the left electrode μ_L (substrate). The right electrode (tip) is shifted up and opens up a non-polarized direct tunneling channel, passing through the molecule in the HOMO-LUMO gap region, depicted by the blue-red arrow in Figure 4.31b and the two yellow circles (arrows represent the spin of the electrons).

The case of higher bias voltages is depicted in Figure 4.31c. The asymmetric configuration (tunneling barrier to the tip) explains a large shift of the Fermi level of the tip (μ_R) and the small shift of the levels of the molecule. At the threshold of -1.0 V, the HOMO becomes aligned with the substrate (μ_L), as shown in Figure 4.31c. At this point, similarly to the non-magnetic case, one of the electrons can hop from the HOMO to the lead. The acquired spectra suggest that the molecule becomes single positively charged (cf. Figure 4.22). The second electron at the HOMO seems to be blocked from hopping off, e.g. by coulomb blockade. At this point, a negative differential conductance was observed. The occurrence of the NDC without influence of the material of the tip indicates that the ferromagnetic substrate-EDA configuration is responsible for the effect.

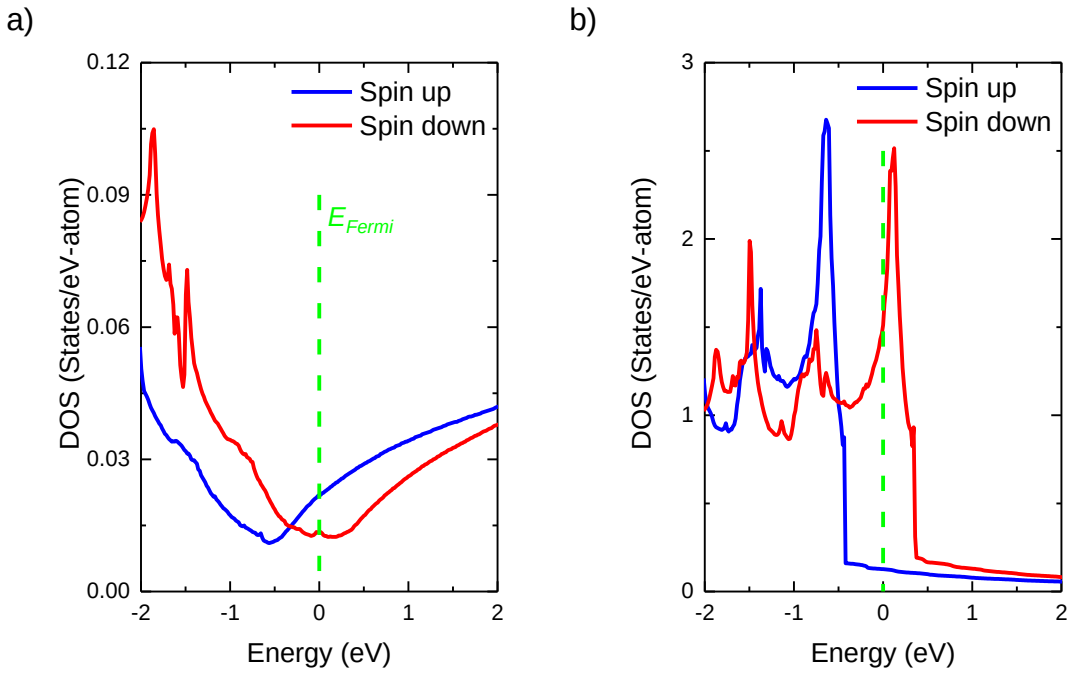

Figure 4.32.: Density of states for nickel, adopted from [228]. a) shows the cumulative DOS of the nickel s- and p-states. b) displays the DOS of the d-bands of nickel.

Furthermore, we have to take into account that the binding of the molecule is most likely established by hybridization with the d-states of the nickel [227, 229]. The density of states

of the nickel d-bands is depicted in Figure 4.32b. A clear anisotropy is observable, whereas the spin up levels are completely filled and the spin down levels reveal a large amount of unoccupied states.
The strong anisotropy of the substrate (Figure 4.32) results in the ferromagnetic properties of the nickel. Consequently, magnetic domains are formed. This becomes an important property as soon as the molecules charge state is modified to +1. Now, a distinct spin remains at the HOMO of the molecule.
It is well known from literature that a spin, located at a molecule, aligns either ferro- or antiferromagnetic to a (anti-)ferromagnetic substrate [230–233]. Thus, we assume that the remaining spin at the HOMO gets magnetically coupled to the substrate in its favorable spin direction and cannot be replaced/ flipped by an electron with the opposite spin without additional energy.

At the point, where the HOMO gets aligned with the Fermi level of the substrate, a new transport channel is opened up. The small red arrow in Figure 4.31c represents the newly appearing electron transport channel through the orbital. In contrast to the non-magnetic case, the HOMO is occupied now by a distinct spin, which allows (due to Pauli principle [234]) only the opposite spin direction to pass through this orbital. Only half of the (unpolarized) current is able to flow through the molecule. This positive contribution to the conductivity is accompanied by the reduction of the direct tunneling current. The direct tunneling current through the molecule seems to be decreased by blocking one of the two spin channels by spin scattering [227, 235]. Hence, the nonlinearly increasing direct tunneling current is reduced to half, as indicated by the dashed blue line in Figure 4.31a as well as the small red arrow in Figure 4.31c. By summing up the positive contribution for the transport through the HOMO and the negative contribution, originating from the reduction of the direct tunneling current, a drop of the junction current emerges exactly at the position, where the molecule gets charged. Thus, the negative differential conductance, caused by the emerging of a spin valve is observed at the threshold of -1.0 V (cf. Figure 4.21).

The last section, demonstrated the possibility of building a room temperature stable NDC device by using a ferromagnet-molecule-metal junction. The observed Raman spectra, in combination with the current-voltage-characteristics for the ferromagnetic as well as the non-magnetic configuration suggest the occurrence of a single spin phenomenon.

In order to clarify the origin of the NDC, further experiments need to be performed. First, the statistics should be increased. Second, the nonmagnetic test experiment needs to be performed, using a simpler metal (e.g. aluminum), to unambiguously prove the presented hypothesis.

CHAPTER 5

Summary

In conclusion, the investigation of single-molecules at low temperatures, the stress induced change of the vibrational modes of helicene molecules as well as a single-molecule NDC have been demonstrated in this thesis.

The investigations used the multitechnique of electrical and optical (Raman) spectroscopy, combined in the home-built MJS-setup.
To demonstrate the feasibility to measure single-molecules at low temperatures, the TM-TPD and TPD molecules have been employed. The investigations of both molecules revealed slightly different results for room temperature and low temperature measurements. The TM-TPD system showed Raman signal only in its conducting state, which results in the possibility of switching the Raman-response reversibly on and off. The low temperature measurements on the TPD system demonstrated a voltage dependent change of the Raman intensity, similarly to the TM-TPD results. The switching behavior of TPD was only found at low temperatures, which can be, according to simulations related to the lower amount of energetically reachable conformations.
Distinct charged states are identified by the current-voltage as well as the Raman measurements. Furthermore, DFT calculation have been performed to support and verify the experimentally acquired data.

After benchmarking the setup, two different geometries have been investigated. At first, a gold-molecule-gold heterostructure was used. The employed molecule was a 1,7-dithiol-7-helicene, consisting of seven phenyl rings and a thiol anchor group at the first and the last ring.
The measurements were performed by establishing the junction and subsequently displacing

the electrodes. At each point, a Raman spectrum was acquired. The investigated spectra display a systematic change in the vibrational pattern with the tip sample distance. Simulations have been performed to verify the stretching of the helicene molecule. The experimental data show a stable junction up to an electrode displacement of about 4.2 Å, where a stretching of ∼2.5 Å can be assigned to the molecule itself by the comparison of the experimental and simulated data. The rest of the displacement is associated with deformation of the electrodes. The shift of one distinct vibrational mode was chosen and systematically analyzed. Thereby, a decrease of the intramolecular vibration energy of 8 cm^{-1} was observed. The identification of a changing vibrational energy in dependence of applied strain to such molecules in a single-molecule junction is a novel result, promoting further evidence about the stability of the setup as well as the investigation of single-molecules.

The second geometry used a nickel-molecule-nickel and a silver-molecule-silver heterostructure. The employed molecule was symmetric and featured carboxylic anchor groups on both sides. Acquiring data from this molecule in junctions with ferromagnetic leads, asymmetric current-voltage characteristics were observed. Furthermore, the EDA molecule revealed a charged state of +1 when the junction was biased with a voltage lower than -1.0 V. Exactly at this position a negative differential conductance was observed. The positive charge state of the molecule was identified by comparing the Raman spectra with simulated spectra for different charged states.

The same molecule was also investigated using non-magnetic (silver) electrodes. Thereby, symmetric current-voltage characteristics without a current-drop were observed. Additionally, a charging of the molecule to the positive state was observed at ±0.6 V.
The occurrence of the NDC only in case of using at least one ferromagnetic electrode indicates a phenomenon, which is related to the magnetic properties of the electrode.
The current-drop of about 15% in case of using ferromagnetic electrodes in combination with the charging of the molecule at this threshold voltage shows the possibility of building a room temperature stable NDC device. The single-molecule junction might behave like a spin-valve, which filters one of the spin-directions above a certain bias voltage.

This technique might be interesting for future applications like NDC transistors or NDC logic grids, using the crossbar architecture. The additional state, offered by the NDC could increase the calculation speed in logic elements and the storage density significantly. Furthermore, the NDC state is room temperature stable, resulting in the opportunity to implement such devices in already existing computational infrastructure.

As demonstrated, the MJS-setup opens up many possibilities for studying single-molecule phenomena. In order to get more evidence about the molecule stretching of DHE, systematic voltage dependent stretching experiments needs to be performed.
The hypothesis about the NDC should be proved by performing test experiments on single-molecule junctions with simpler metals like aluminum in combination with EDA.

The demonstrated proof of concept for the low temperature investigations offers a great potential for further fundamental research about single-molecule properties in various configurations. The ability of building frequency tunable single-molecule springs, as shown in chapter 4.2, demonstrates the capability of the MJS technique for basic research. On the other hand, systems, which combine fundamental research with application relevant techniques, like the single-molecule NDC have been developed too. Therefore, the MJS setup offers a bunch of tools to understand processes on the single-molecule scale and further develop molecular systems to a stadium, being relevant for application.

APPENDIX A

LabVIEW Routines

This appendix explains in detail the newly designed LabVIEW program, including all measurement routines and analysis tools. Because of the graphic programming interface (block diagram) of LabVIEW, no code can be attached. The block diagram is enormously large and would fill several 10s of pages. Therefore, only screenshots of the user interfaces are shown and the routines are explained in detail.

A.1. Setup control and characterization

The LabVIEW program, controlling the setup was built from the zero level. Therefore, the design of the program is completely new and subsequently structured. The block diagram of the program is patterned in three parts (flat sequence). First, all components are initialized. The controller of the liquid nitrogen cooled CCD and the Attocube actuators are remotely controlled (LabVIEW remote function), because the drivers are not working on systems, newer than Windows XP. Consequently, these devices are connected to a Windows XP computer and controlled by a (self-written) LabVIEW program, running on this PC. However, all devices can be operated from the main computer. After initializing all components, which works fully modular (unused devices can be deselected and initialized later) the measurement routines are embedded in a running loop. By pressing the stop button, this loop is stopped and all connections to the initialized devices are terminated.

The main loop of the program runs a stacked sequence of all different routines, where only one per time can be selected and activated. The selection occurs by choosing the appropriate

tab in the user interface. In Figure A.1, at the top, the tabs are shown. In the following, the different routines (tabs) will be explained, including their importance for the measurements.

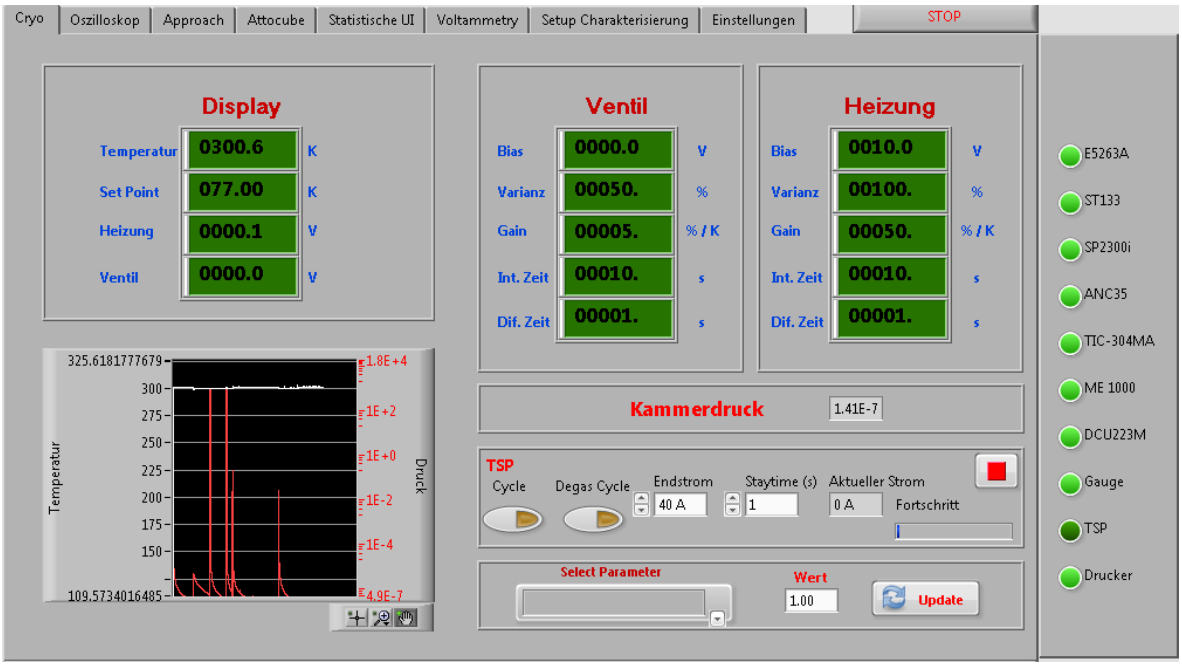

Figure A.1.: Cryostat and TSP control tab

When the device initialization loop finished successfully, the cryostat control tab is automatically opened. At the right side, the different devices are shown, whereby the green indicators show a successful initialization of the according device. The cryostat controller (heater and throttle valve) outputs actual values and offers the possibility of modifying the control behavior by changing a bunch of parameters. The main properties are displayed in the green boxes. Additionally, the chamber pressure is read out and displayed, if this tab is selected. The actual pressure and the actual cryostat temperature are illustrated in the plot at the bottom left. As last part in this routine, the TSP can be controlled. It is possible to run cycles, ramping the filament current up and down in a controlled way. Simultaneously, the filament current is displayed. The large stop button at the top right, ends the main loop of the whole LabVIEW program.

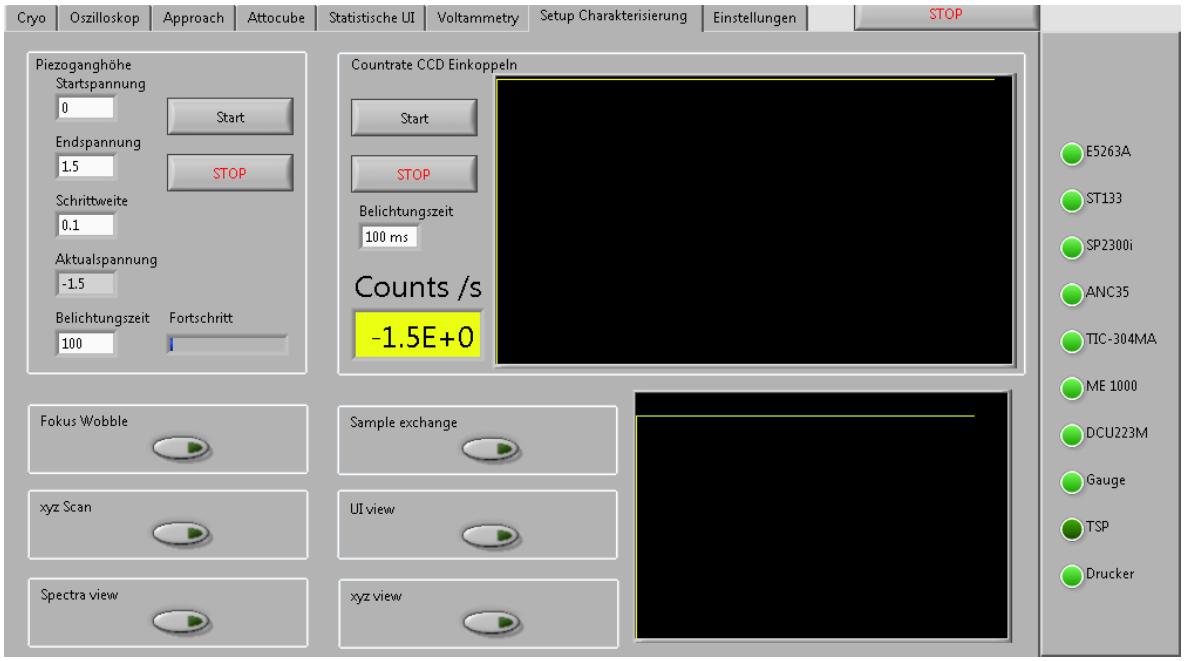

Figure A.2.: Setup characterization tab

The next important tab/ routine about the basic parameter of the setup is the setup characterization routine, as shown in Figure A.2. Here, several routines, which are necessary to characterize the setup parameters in a fully automatized/ highly convenient way are implemented. The first routine is run by the gray box at the top left. This routine is needed to calibrate the travel distance of the piezo (standing wave method). For this, the tip needs to be in the working distance of the piezo and the laser beam needs to be fairly focused to the apex. Now, the count rate of the laser peak is recorded as a function of the elongation of the piezo. This results in a sine-like minimum-maximum pattern, which can be correlated to the excitation wavelength. Out of that, the maximum piezo travel distance as well as the minimum step size can be calculated.

The second routine (top right box in Figure A.2) is needed for optimizing the coupling to the fibers. The diagram shows the Gaussian peak fitted laser intensity as a timeline. This simplifies the finding of the maximum signal point. Additionally the width of the Gaussian peak is displayed in the diagram at the bottom right. This can be used for optimizing the incoupling to the spectrometer. The buttons at the bottom left open several different subroutines. The so-called focus wobble routine moves the sample periodically up and down, in order to align the optical path to be perpendicular to the objective in the chamber (concentrically defocusing spot). Furthermore, a sample exchange routine, which moves the objective to a save position and switches the pressure gauge off, can be used. The remaining buttons open the scanning LabVIEW program (A.3.2) and different analysis routines (A.4).

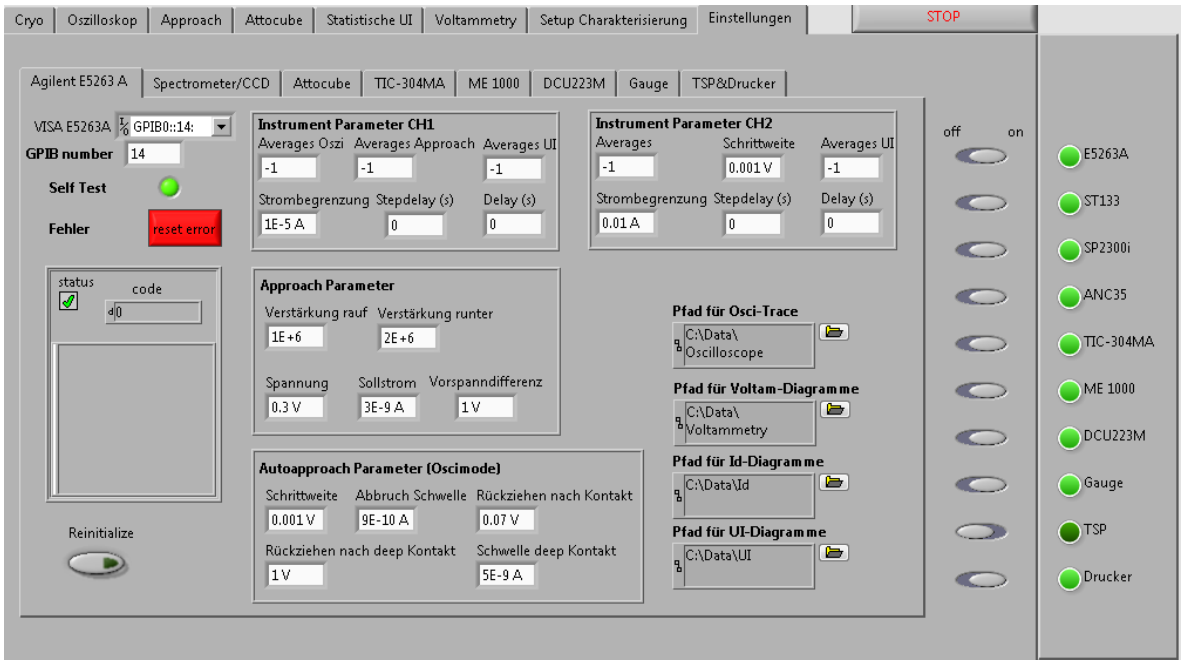

Figure A.3.: Preferneces of the source meter

The following two Figures show the main preferences tabs of the LabVIEW program.
One is the tab, where the parameters of the Agilent source meter can be modified (Figure A.3). The basic communication parameter, as GPIB port number and communication errors are displayed in this tab at the left. At the bottom right, the paths (oscilloscope traces, I-V data, I-d data) for saving the measurement data can be adjusted. The measurement parameters are modified by the values in the gray boxes at the center. The uppermost one changes the PLC averaging, current compliance and step delay time for the oscilloscope, I-V (A.2.3) and feedback (A.2.1) routines. The second box offers the possibility of modifying the regulation parameter of the feedback loop, as the up/ down gain, the set point, and the bias voltage. The lowest box includes the values, used by the auto-approach routine (included in the oscilloscope routine). Here, the step size, the maximum current, the retraction coefficient as well as the emergency deep contact parameters can be adjusted.

The switches, displayed at the right side, offer the possibility of initializing or terminating measurement devices, either at starting of the program or while the main loop is running.

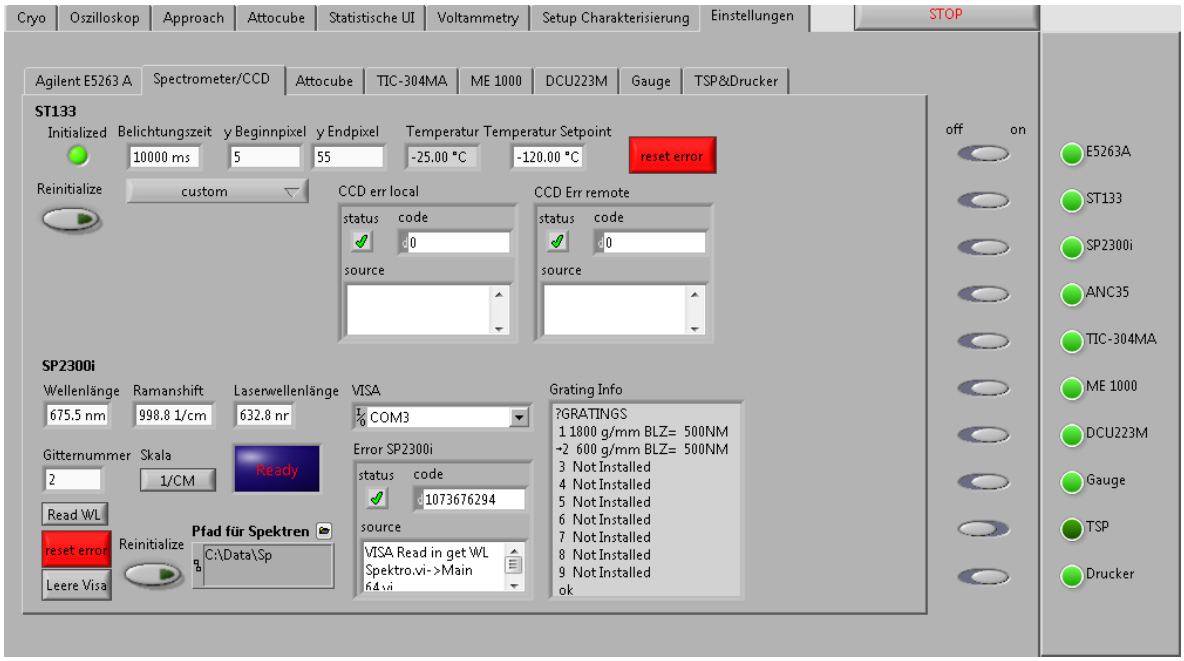

Figure A.4.: Settings tab for the CCD and the specrtometer

The last important settings tab (Figure A.4) adjusts the parameter of the liquid nitrogen cooled CCD and the spectrometer. As mentioned, the CCD is remotely controlled, meaning the parameter are automatically transferred to the LabVIEW routine on the Windows XP computer.

Here, the parameters, like the exposure time, the read out mode and the temperature set point of the CCD can be adjusted. The actual temperature is also displayed. By moving the mouse cursor over the display area, the temperature is actualized. Furthermore, occurring communication errors to the Windows XP computer as well as errors of the communication between the remote computer and the CCD are displayed.
The lower part is used for controlling the spectrometer. Here, the information about the installed gratings can be read out. Additionally, the center wavelength is adjustable and the laser wavelength can be read in, for calculating the Raman shifts. The energy scale is switchable between wavelength and Raman shift.

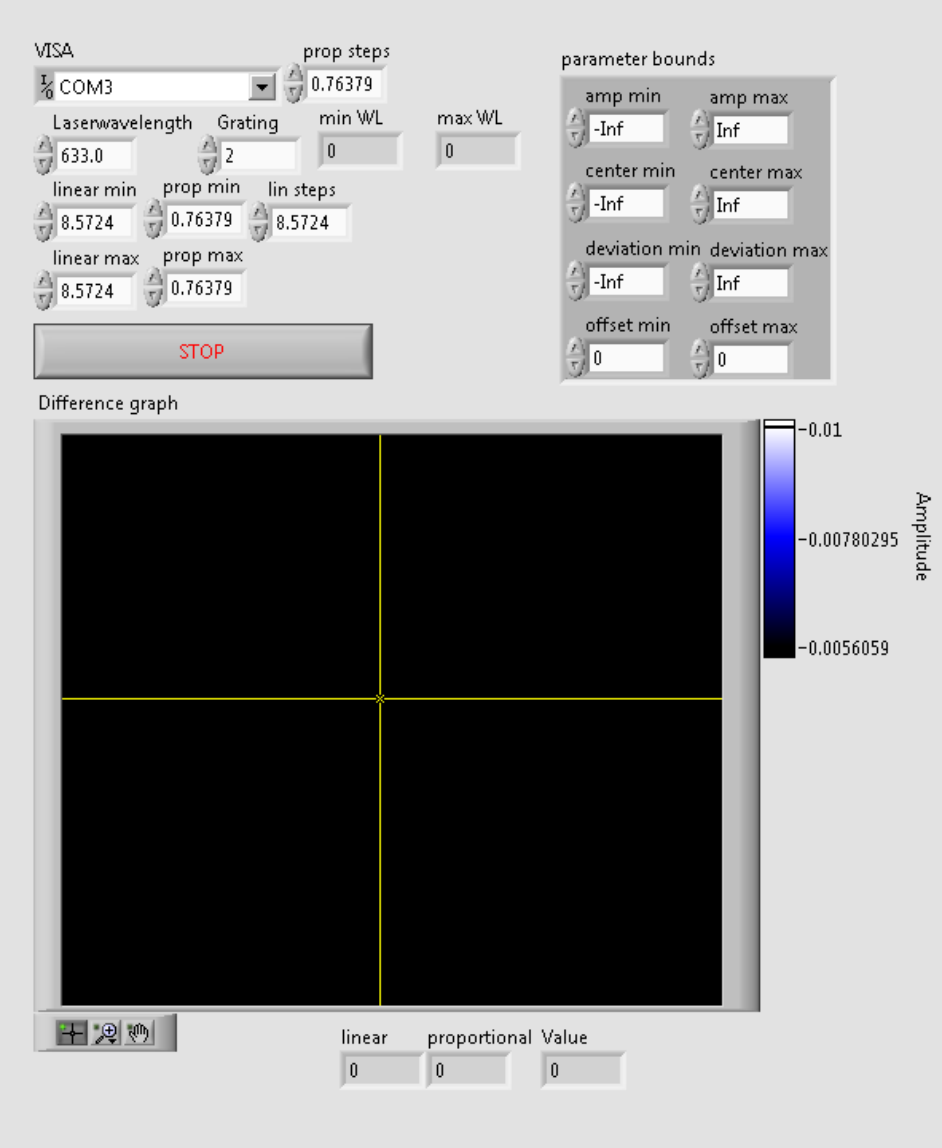

Figure A.5.: Calbration tool for the spectrometer

For calculating the energy scale accurately, it is necessary to calibrate the spectrometer. Another fully automatized self-written LabVIEW tool does this. Here, the linear and proportional constants for the spectrometer can be calibrated. By knowing the actual laser wavelength, three spectra are recorded. One with the laser in the center and two with the laser on both edges of the spectral range. From this, the parameters are calculated by achieving the minimum energy discrepancy between the energies of the three measured laser peaks. The user interface of this tool is shown in Figure A.5.

A.2. Electric Measurements

The following section points out the routines, used for single-molecule junctions electrically.

A.2.1. Feedback Loop

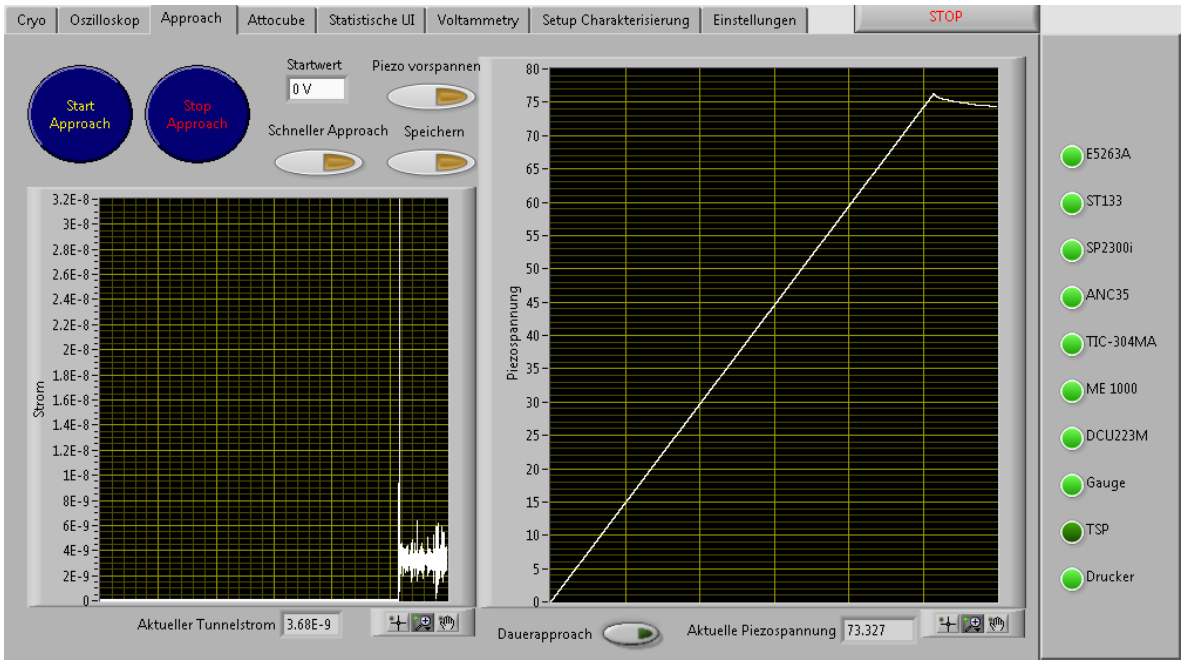

Figure A.6.: User interface of the feedback loop

After approaching the tip in the travel range of the piezo, the feedback loop is used. This routine controls the piezo voltage in dependence of the current. If the current is below the set point, the piezo voltage of the next step is calculated by the difference between the current set point and the actual current, which is than multiplied with a gain factor. In case of a current, larger than the set point, the difference is multiplied by a (larger) second gain factor. This prevents the tip crashing into the substrate, due to piezo creep. The diagram on the left side shows the current as timeline. The corresponding piezo voltage is displayed at the right side. This routine can start either from a piezo voltage of zero or from an inserted higher start value. The gain up factor can be influenced by pressing the fast approach button, resulting in a 10 times larger step size. When this routine is stopped, it is possible to keep the piezo voltage at a level, which is equivalent with a tip sample distance of ~90 nm. The approach traces can be manually saved.

This routine was previously existing, but was implemented to LabVIEW and modified by the features of the last paragraph.

A.2.2. Current-Distance Measurement

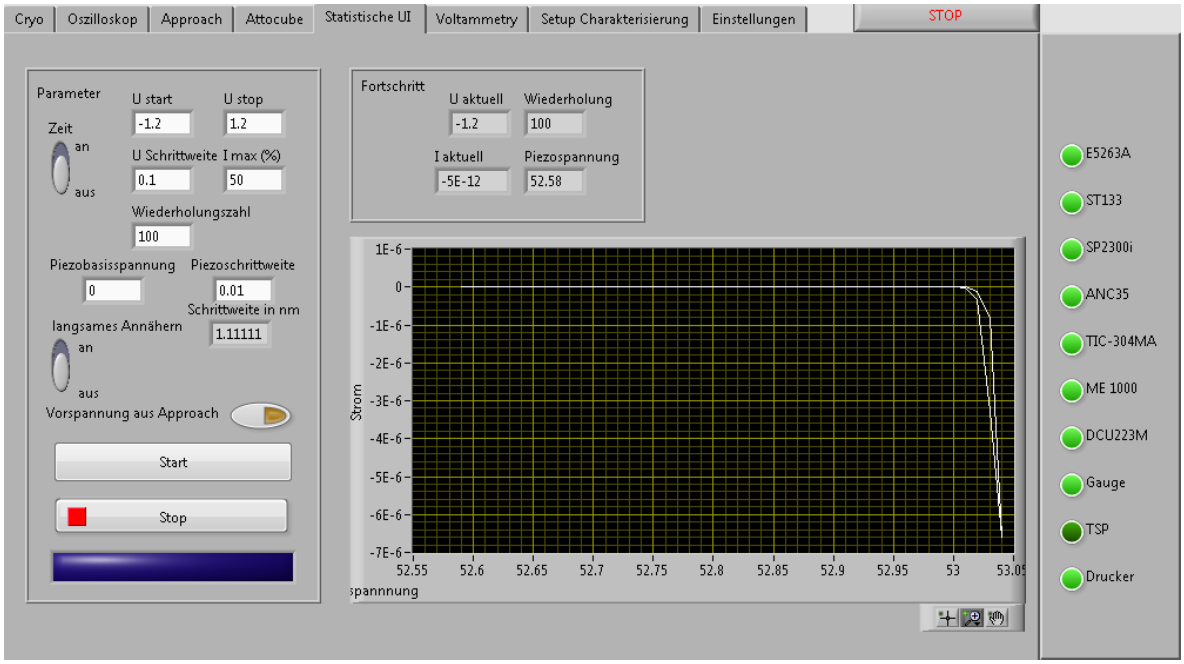

Figure A.7.: Current-distance measurement routine

The current-distance measurement routine was newly designed, in order to reduce the amount on measurements, which needed to be manually performed. This routine approaches and retracts the tip. During this process, the current is recorded as a function of the piezo voltage. Usually, the approaching point from the feedback loop is used as start point. From that on, the tip is approached until a certain current ratio of the full metallic contact is reached. At this point, the tip becomes retracted again. The steps of approaching and retracting can be adjusted, down to the minimum possible level (0.26 Å). This procedure can be automatically repeated (usually 100 times) for a set of different bias voltages. Therefore, it is possible to insert a minimum and maximum voltage and a step size.
This routine automatically saves each single run as own file. When the routine ends, the piezo voltage is retracted to 0 V, in order to ensure enough space between the tip and the substrate.

By running the I-d measurement for a large bias voltage range with a high amount of repeating, statistical current-voltage characteristics of molecule junctions can be acquired.

A.2.3. Oscilloscope Routine

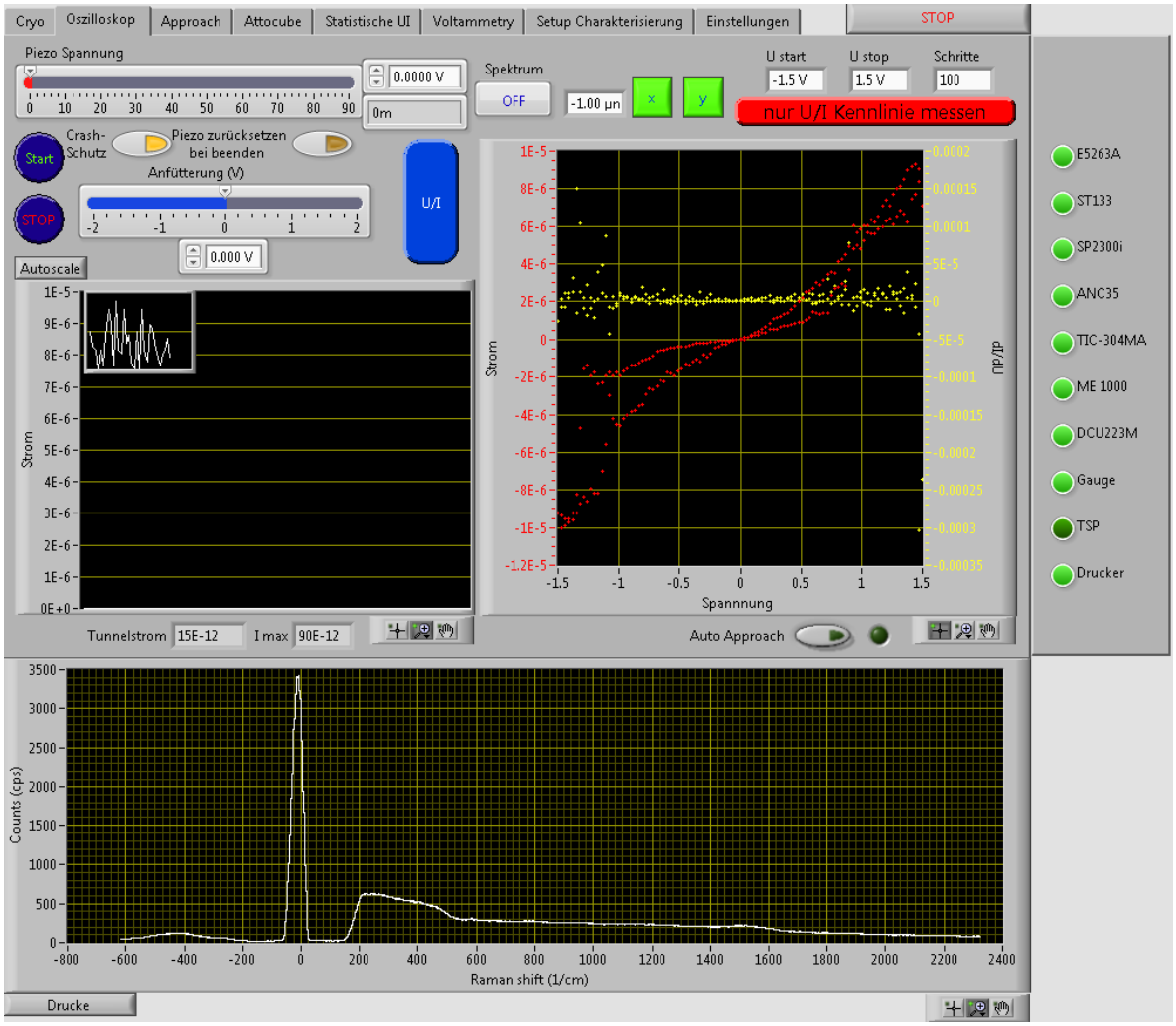

Figure A.8.: User interface of the oscilloscope mode tab

The oscilloscope routine gets its name, because this routine previously existed in Agilent VEE as an oscilloscope routine without further functionalities. Now, the oscilloscope LabVIEW routine is the most important and central part for acquiring measurement data. Therefore, it contains a bunch of newly developed indispensable tools for investigating the electrical and optical properties of single-molecule junctions.

This routine offers the possibility of adjusting the piezo voltage and the junction voltage manually by runtime. Additionally, the Attocube actuators can be precisely moved. Current-voltage measurements, by sweeping the bias voltage and recording the current are the main part, together with the opportunity to acquire Raman spectra.

The basic function is the acquiring of the current as a timeline at a certain bias voltage. This is done in the graph at the left side. At the same time, the piezo voltage, which is recalculated

in the piezo elongation, can be changed by runtime with the large slider at the top. Previously, it was necessary to prevent manually a deep contact between tip and substrate. Now, a crash prevention is implemented, which automatically retracts the tip, by reducing the piezo voltage, if the current level is to high (indicator for a deep contact). The piezo can be stabilized by using the auto-approach feature, which keeps the distance in a range, where the current level is slightly above the noise level. This is useful as long as the piezo is still creeping (∼30 minutes after adjusting a voltage level).
If the junction was established by manual distance control, after the stabilization time, the "U/I" button starts the investigation of a current-voltage curve. The I-V measurements are performed by first reducing the bias voltage from the previous level to 0. Afterwards the voltage is swept from 0 to the lower limit in the half amount of total steps. From the lower level to the upper one a measurement with full amount of steps is performed. At last, from the upper limit to zero, again half amount of steps is used. This results in a I-V curve with two times the amount of steps, but two points per voltage step. If a hysteresis I-V-curve emerges, it is indicated that the setup was not stable during the measurement or the molecule escaped from the junction.
Simultaneously with the current recording, Raman spectroscopy can be performed. Therefore, the "Spektrum" button needs to be switched on. In this case, the routine permanently acquires spectra, displays the data in the graph at the bottom and saves each in a file. The file name contains the actual bias voltage, the date and time and the exposure time. The recorded count rate is re-normalized to counts per second. The acquisition parameters need to be adjusted first in the settings tab. Additionally, the possibility of re-adjusting the position of the objective, by using the Attocube actuators is implemented. For moving the objective, the moving distance (including the algebraic sign) needs to be inserted and the button for the wanted axis (x or y) must be pushed.

The oscilloscope mode is the central routine in terms of molecule junction spectroscopy and allows recording spectra concomitantly with the current in dependence of the applied bias voltage.

A.3. Optical Measurements

The following section shows the routines, which are designed for the optical measurements, including the newly developed three dimensional scan routine, allowing a full mapping of the T-tip.

A.3.1. Sample Imaging and Raman spectroscopy

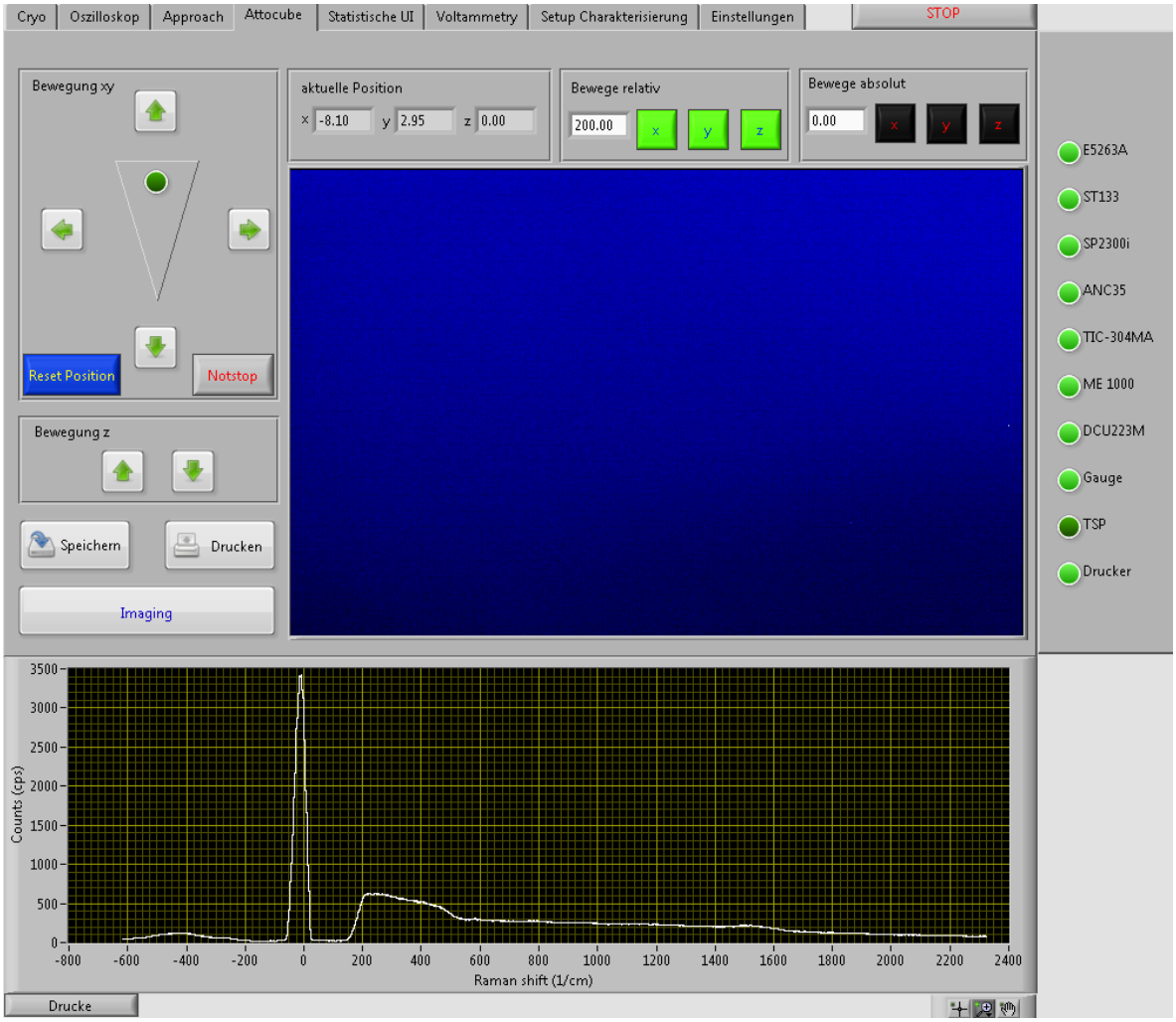

Figure A.9.: Sample imaging and isolated Raman spectroscopy routine

The "Attocube" tab offers the features of moving the Attocube actuators in all three dimensions with the absolute position or relative distance movement mode. By clicking on the arrow buttons on the left side of the panel, the actuators can be moved, using the constant travel mode. Here, the actuator moves, as long as the button remains pushed. The actual positions of the actuators are displayed at the top to Figure A.9. If the laser spot is positioned on the

tip, usually this position is set as origin for the coordinate system (blue button). The large blue colored area displays an optical image of the sample. Consequently, this can be used to position the spot roughly on the apex of the tip. The image can be saved in a file or printed out by using one of these features.
The button on the bottom left changes between imaging and spectrum mode. Here, either sample imaging or Raman spectroscopy can be performed. The spectroscopy mode is not employed anymore, since the oscilloscope routine can perform Raman spectroscopy too.

A.3.2. Three Dimensional Tip Scanning

The most powerful routine in terms of Raman spectroscopy and finding the maximum enhancement point on the T-Tip is the three dimensional scanning routine. The functionality of this routine was previously done by manual movement of the objective and comparing the signal intensities of the different positions. Consequently, this routine makes the positioning of the laser spot more reliable, easier and faster.

This independent LabVIEW tool features three tabs, where the first one is needed for setting up the scan, the second one for analyzing and the third one is responsible for the basic parameters (laser wavelength, exposure time and error messages). The scan tab offers to

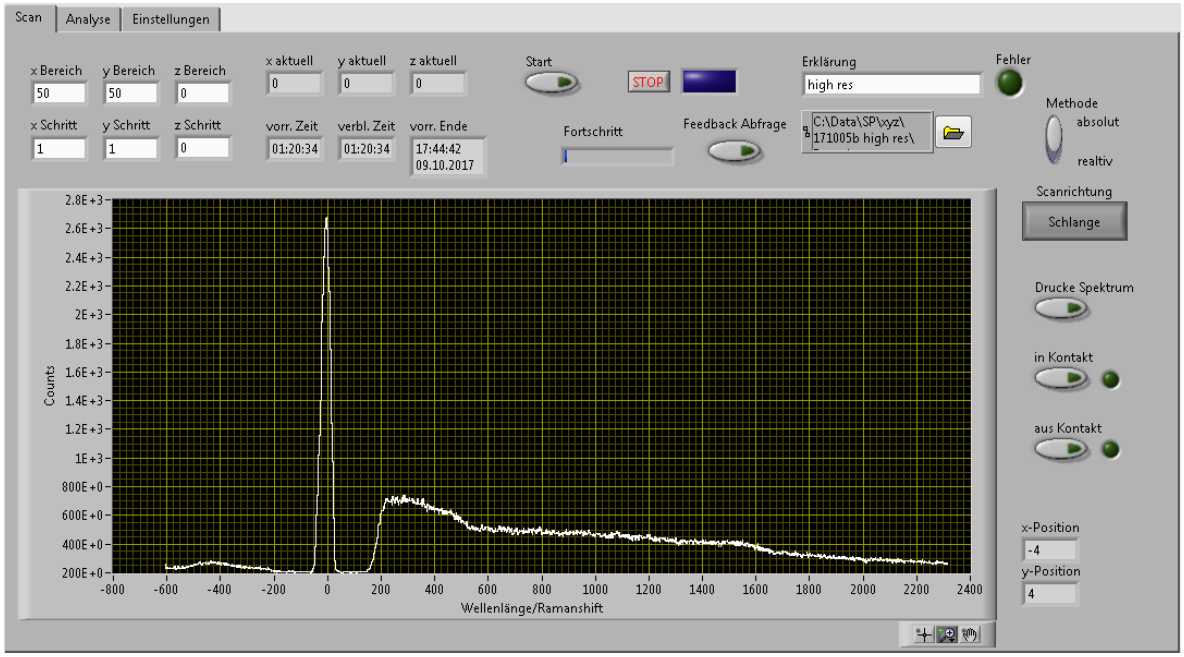

Figure A.10.: User interface of the scan tab

input the scan variables. This means, the x, y, and z range were it should scan as well as the step sizes for the different directions. The scan is always centrically performed around the initial set point of the objective. Therefore, the actuators move at the begin of the scan to the minus range half positions. Furthermore, the scanning mode can be chosen, either scanning line wise with back traveling to the minus half position or moving snake-like, which introduces less vibrations to the setup (no large movement). The minimum possible step size is 1μm, caused by the hardware interface of the Attocube actuators as well as their position read out accuracy. When the travel ranges and step sizes are inputted, the estimated scan time and the estimated end time of the scan is displayed, which simplifies the time management of the experiment. During the scan, the actual position, the elapsed time and the remaining time is shown. At the right white area, a scan description can be written, in order to simplify the

data searching later. At the end, the objective is moved at the initial position, which allows using the scan coordinates as absolute coordinates.

The scan takes at each single step a full Raman spectrum and saves it in an own file. All files are labeled with the x, y, z-position in the file name and saved together in one folder. Additionally, a "data.dat" file is created at the beginning of the scan, which contains the ranges, step sizes, laser wavelength, unique tip number and the sample label (including the used molecule species). This allows to retrieve any old scan with its full parameter set and experimental conditions.

The scans can be analyzed anytime, using the analysis tool (see A.4.4). Practically the scans are analyzed directly when they are finished. For this, an analysis routine, which keeps the investigated data in the memory (no importing from HDD is needed), was added. Figure A.11 displays the user interface of the analysis tab.

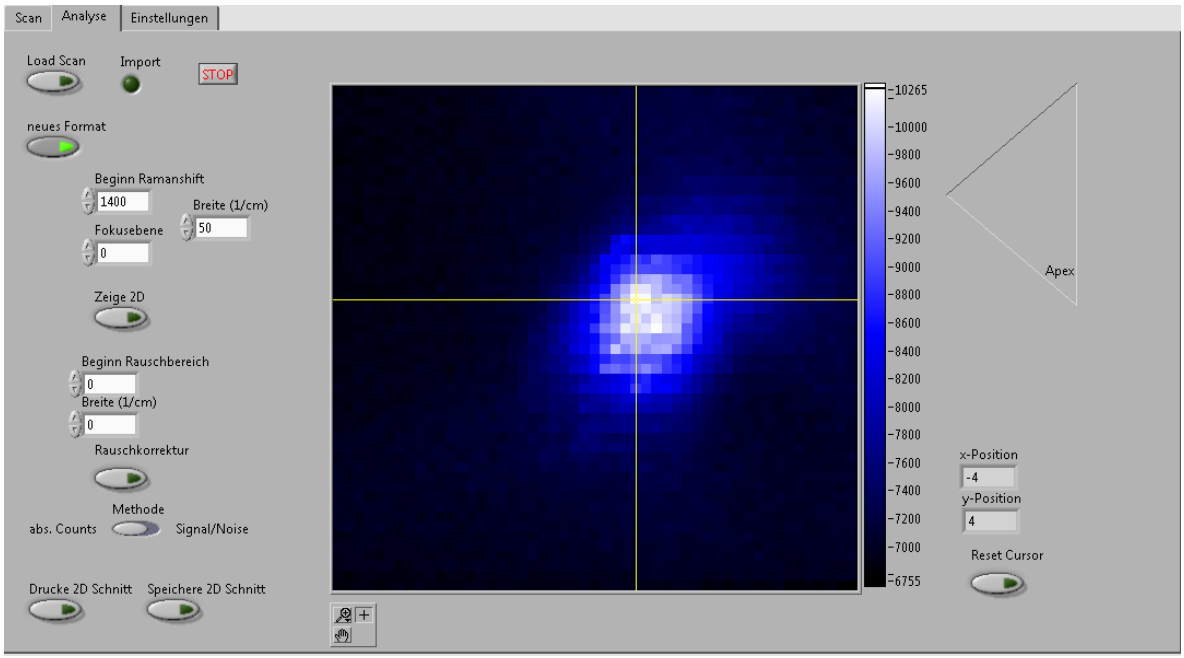

Figure A.11.: User interface of the analysis tab

During a three dimensional scan, a four dimensional array (3D in space and 1D in energy resolved intensity) is created. In terms of Raman shift, a range (center point and width), where the intensity is pointwise cumulated is chosen. In case of a 3D scan, the focal plane (z-coordinate) has to be selected for showing the two dimensional color map plot. The center of Figure A.11 shows the Raman intensity as a function of the excitation/ collection spot position. In the case of a very weak signal, the noise level can be subtracted, meaning at each spatial point, the noise level is determined by cumulating the intensity in the (previously) selected noise region. From that, either the difference or the quotient is plotted.

By selecting the laser line, the shape of the tip can be displayed (see Figure 3.7). The cursor in the graph can be used to display the whole spectrum at this point (shown at the scan tab). From the point of maximum Raman signal or the meeting point of the tip edges (seeable from the laser reflection), the apex of the T-Tip can be doubtless determined. The cursor position is also displayed at the right side, which allows to find the apex by manual position control again (oscilloscope mode).
The shape of the tip as well as the absolute count rate can be conserved by printing the two dimensional intersection with all necessary parameters out.

This scanning routine opens up the ability of determining the apex of the T-Tip in a highly reproducible way, even if no Raman signal from molecules is detectable. Especially, the measurements in section 4.1 were significantly easier using this routine, than trying to find the enhancement point manually.

A.4. Data Analysis

The change from Agilent VEE and WinSpec to LabVIEW increased the amount of investigated data significantly. Consequently, analysis tools for each different kind of acquired data was needed. In the following, the four different LabVIEW scripts will be presented. Each of them has been converted to an independent executable file, which can be used on each Windows computer without installing LabVIEW.

A.4.1. Current-Distance Curves

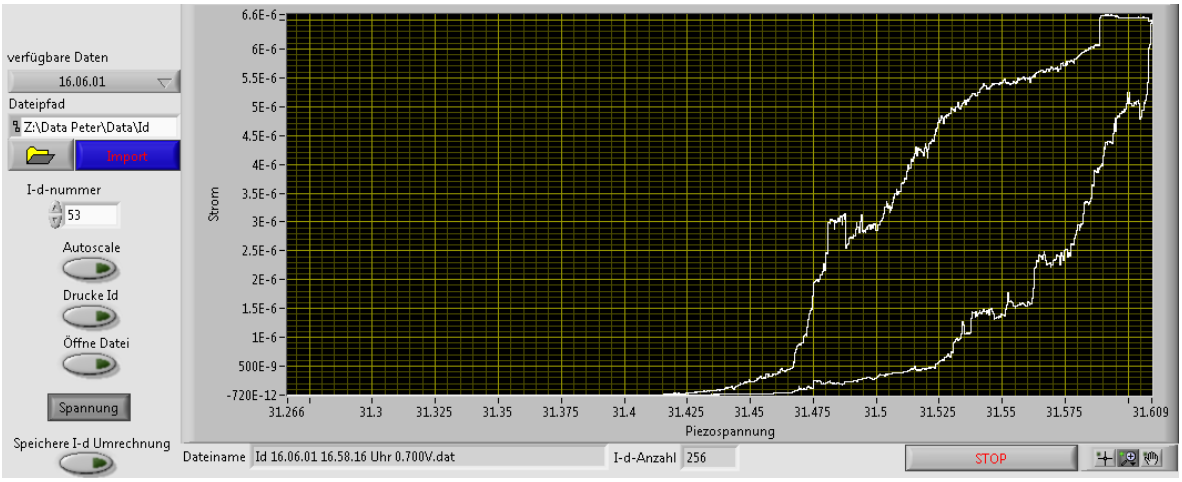

Figure A.12.: Current-distance curve analysis tool

Due to the automatized acquiring of current distance curves (∼500 per hour) a data viewer and analysis tool was necessary. Using the tool, whose user interface is depicted in Figure A.12, it is possible to display subsequently all the investigated I-d curves, measured at one day. Thereby, the piezo voltage can be directly recalculated to a tip-sample distance. At the bottom, the name of the actually displayed I-d curve is shown. The selection of reliable and suitable curves occurs by manual determination. This means, if a I-d curve with a plateau is discovered, the file can be opened directly from this routine. A statistical analysis has to be performed in a program for interactive scientific graphing and data analysis, like Origin.

A.4.2. Current-Voltage Curves

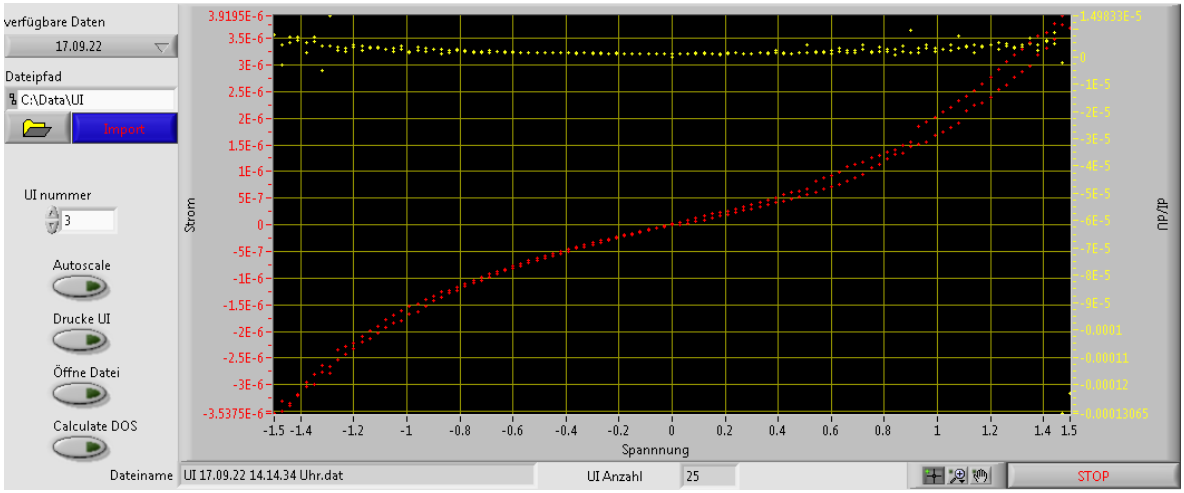

Figure A.13.: User interface of the current-voltage data analysis program

The investigated current-voltage curves can be displayed and analyzed with this program. Again, the I-V curves can be imported day wise, which means there can be several hundreds of curves loaded in one step. The red points in the graph in Figure A.13 display the investigated current as a function of the bias voltage. The yellow points show the corresponding differential conductance, which is automatically calculated. By changing the value of the "UI number", all imported files can be successively displayed. The file corresponding to the displayed curve (name is shown at the bottom) can be directly opened from this routine.
For some purpose, the feature of calculating the density of states out of the current-voltage data was programmed too. This is done, by point wise dividing of the derivative of the current by the conductance value at this point. The emerging density of states curve can be displayed in a similar way (different tool) than the current-voltage characteristics.

A.4.3. Raman Spectra

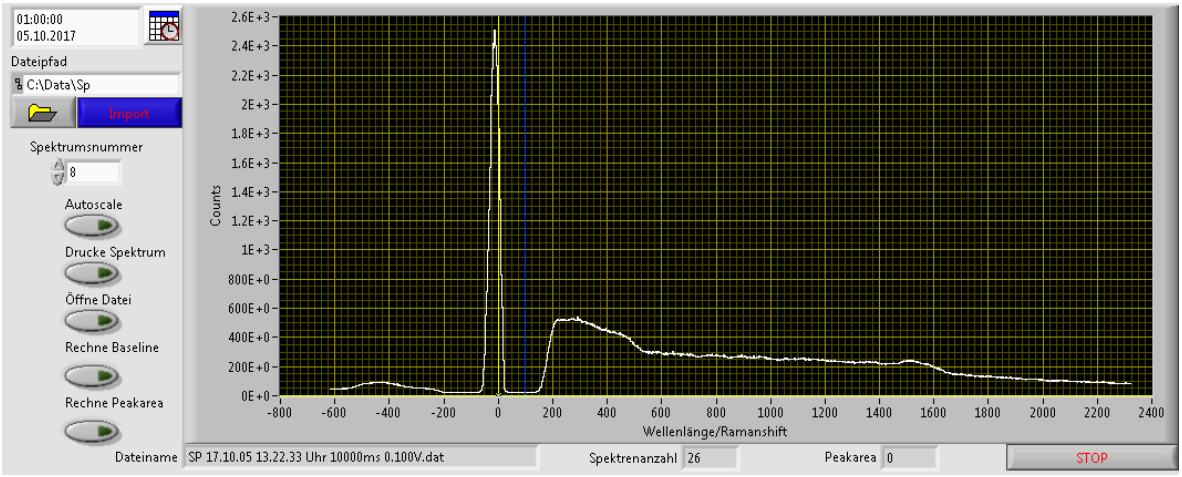

Figure A.14.: Analysis tool for investigated Raman spectra

The analysis tool for the investigated spectra imports the spectra, in a similar way than the other tools, day wise. The actual displayed spectrum is again chosen by the running number as well as its file name is displayed at the bottom and the file can be directly opened from the user interface.
The special features of this tool is the ability of computing and subtracting a baseline. Additionally, the peak area of a selected peak in the spectrum can be calculated. For the baseline subtraction, several anchor points are selected by cursors in the graph. From these points, by cubic spline interpolation a baseline is calculated. The subtracted spectrum is displayed together with the initial one, in order to determine, if the baseline is accurate and the anchor points were appropriate. The subtracted spectrum can be saved for further data processing. The second feature of calculating the peak area works on raw as well as baseline subtracted spectra. For the calculation an area is selected in the spectrum by two cursors. Between the two markers, a Gaussian peak is fitted to this spectral range. The out coming peak area of the fit is displayed below the spectrum.

A.4.4. Tip Scan Analysis

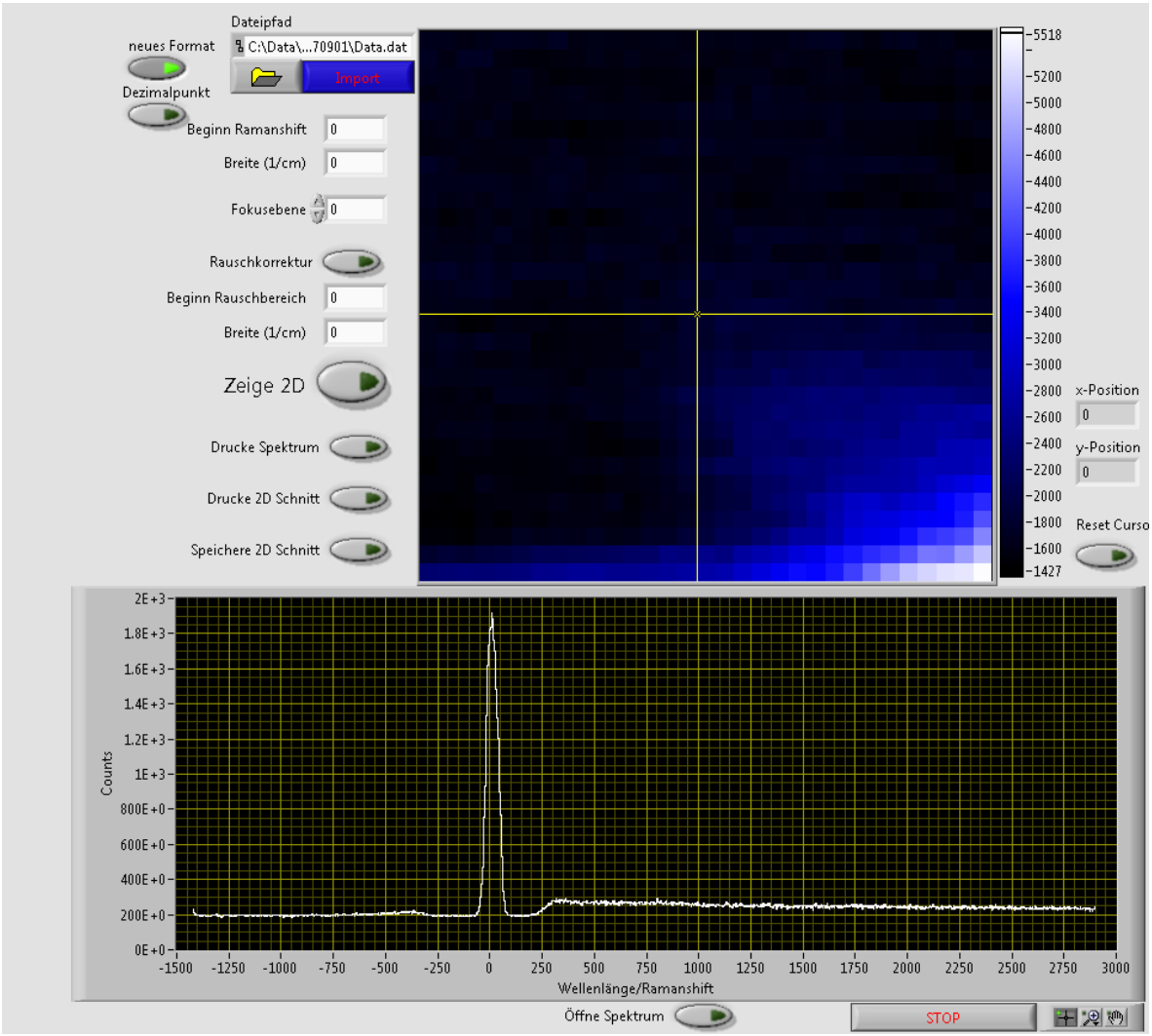

Figure A.15.: User interface of the 3D scan analysis tool

The last data analysis tool is the independent analysis tool for the three dimensional scans, as displayed in Figure A.15. This tool features the same routines as the analysis part of the 3D scanning script (see A.3.2). This means, independently from the computer in the laboratory, the 3D scans can be analyzed on each Windows computer. Therefore, the "data.dat" file in the particular folder of the scan needs to be selected by the import routine of this tool. The imported scan can be displayed again in two-dimensional intersections, where the cumulated intensity of a certain energy range is displayed in dependence of the position. The same noise reduction routine (cf. A.3.2) is employed to calculate either the absolute intensity above noise level or the signal to noise ratio. A point in the 2D map, whose spectrum is shown below the map, is selected using the cursor. The 2D intersection can be saved in a file or printed

out. Similarly, it is possible to print the spectrum out or open the file of the actual displayed spectrum.

Bibliography

[1] Bardeen, J. & Brattain, W. H. The transistor, a semi-conductor triode. *Physical Review* **74**, 230–231 (1948).

[2] Kilby, J., Miniaturized electronic circuits, USA patentus US3 138 743 A, Jun. 23, 1964.

[3] Samsung. Samsung starts industry's first mass production of system-on-chip with 10-nanometer finfet technology. https://news.samsung.com/global/samsung-starts-industrys-first-mass-production-of-system-on-chip-with-10-nanometer-finfet-technology (2016).

[4] Felix, N. Seven advancements for beyond 7nm chips. https://www.ibm.com/blogs/research/2017/02/ibm-spie-seven-advancements-beyond-7nm-chips/ (2017).

[5] Liang, W., Shores, M. P., Bockrath, M., Long, J. R. & Park, H. Kondo resonance in a single-molecule transistor. *Nature* **417**, 725–729 (2002).

[6] Xu, B., Xiao, X., Yang, X., Zang, L. & Tao, N. Large gate modulation in the current of a room temperature single molecule transistor. *Journal of the American Chemical Society* **127**, 2386–2387 (2005).

[7] Kouwenhoven, L. Single-molecule transistors. *Science* **275**, 1896–1897 (1997).

[8] Chen, Z.-Z., Lü, R. & Zhu, B.-f. Effects of electron-phonon interaction on nonequilibrium transport through a single-molecule transistor. *Physical Review B* **71** (2005).

[9] Yu, L. *et al.* Inelastic electron tunneling via molecular vibrations in single-molecule transistors. *Physical Review Letters* **93**, 266802 (2004).

[10] Heilemann, M., Margeat, E., Kasper, R., Sauer, M. & Tinnefeld, P. Carbocyanine dyes as efficient reversible single-molecule optical switch. *Journal of the American Chemical Society* **127**, 3801–3806 (2005).

[11] Quek, S. Y. *et al.* Mechanically controlled binary conductance switching of a single-molecule junction. *Nature Nanotechnology* **4**, 230–234 (2009).

[12] Choi, P. J., Cai, L., Frieda, K. & Xie, X. S. A stochastic single-molecule event triggers phenotype switching of a bacterial cell. *Science* **322**, 442–446 (2008).

[13] Bates, M., Blosser, T. R. & Zhuang, X. Short-range spectroscopic ruler based on a single-molecule optical switch. *Physical Review Letters* **94** (2005).

[14] Moerner, W. E. *et al.* Optical probing of single molecules of terrylene in a shpol'kii matrix: A two-state single-molecule switch. *The Journal of Physical Chemistry* **98**, 7382–7389 (1994).

[15] Joachim, C. & Gimzewski, J. An electromechanical amplifier using a single molecule. *Chemical Physics Letters* **265**, 353–357 (1997).

[16] Joachim, C. & Gimzewski, J. A nanoscale single-molecule amplifier and its consequences. *Proceedings of the IEEE* **86**, 184–190 (1998).

[17] Ami, S., Hliwa, M. & Joachim, C. Molecular OR and AND logic gates integrated in a single molecule. *Chemical Physics Letters* **367**, 662–668 (2003).

[18] Collier, C. P. *et al.* Electronically configurable molecular-based logic gates. *Science* **285**, 391–394 (1999).

[19] Stadler, R., Ami, S., Joachim, C. & Forshaw, M. Integrating logic functions inside a single molecule. *Nanotechnology* **15**, 5115 (2004).

[20] Osorio, E. A., Bjørnholm, T., Lehn, J.-M., Ruben, M. & van der Zant, H. S. J. Single-molecule transport in three-terminal devices. *Journal of Physics: Condensed Matter* **20**, 374121 (2008).

[21] Chen, Y. *et al.* Nanoscale molecular-switch crossbar circuits. *Nanotechnology* **14**, 462 (2003).

[22] Aviram, A. & Ratner, M. A. Molecular rectifiers. *Chemical Physics Letters* **29**, 277–283 (1974).

[23] Kornyshev, A. A. & Kuznetsov, A. M. A new type of in situ single-molecule rectifier. *ChemPhysChem* **7**, 1036–1040 (2006).

[24] Zhao, J. *et al.* Single $C_{59}N$ molecule as a molecular rectifier. *Physical Review Letters* **95** (2005).

[25] Elbing, M. *et al.* A single-molecule diode. *Proceedings of the National Academy of Sciences of the United States of America* **102**, 8815–8820 (2005).

[26] Heurich, J., Cuevas, J. C., Wenzel, W. & Schön, G. Electrical transport through single-molecule junctions: From molecular orbitals to conduction channels. *Physical Review Letters* **88** (2002).

[27] Jo, M.-H. *et al.* Signatures of molecular magnetism in single-molecule transport spectroscopy. *Nano Letters* **6**, 2014–2020 (2006).

[28] Loppacher, C. *et al.* Direct determination of the energy required to operate a single molecule switch. *Physical Review Letters* **90** (2003).

[29] Aradhya, S. V. & Venkataraman, L. Single-molecule junctions beyond electronic transport. *Nature Nanotechnology* **8**, 399–410 (2013).

[30] Palma, C.-A. & Samori, P. Blueprinting macromolecular electronics. *Nature Chemistry* **3**, 431–436 (2011).

[31] Seldenthuis, J. S., van der Zant, H. S. J., Ratner, M. A. & Thijssen, J. M. Vibrational excitations in weakly coupled single-molecule junctions: A computational analysis. *ACS Nano* **2**, 1445–1451 (2008).

[32] McCarthy, K. D., Prokofev, N. & Tuominen, M. T. Incoherent dynamics of vibrating single-molecule transistors. *Physical Review B* **67**, 245415 (2003).

[33] Scheer, E. *Molecular Electronics: An Introduction to Theory and Experiment.* EBSCO ebook academic collection (World Scientific Publishing Company Pte Limited, 2010).

[34] Mousolou, V. A., Canali, C. M. & Sjöqvist, E. Universal non-adiabatic holonomic gates in quantum dots and single-molecule magnets. *New Journal of Physics* **16**, 013029 (2014).

[35] Wernsdorfer, W., Sessoli, R., Caneschi, A., Gatteschi, D. & Cornia, A. Nonadiabatic Landau-Zener tunneling in Fe_8 molecular nanomagnets. *EPL (Europhysics Letters)* **50**, 552 (2000).

[36] Gupta, A. N. *et al.* Experimental validation of free-energy-landscape reconstruction from non-equilibrium single-molecule force spectroscopy measurements. *Nature Physics* **7**, 631–634 (2011).

[37] Meded, V. *et al.* Electrical control over the Fe(II) spin crossover in a single molecule: Theory and experiment. *Physical Review B* **83** (2011).

[38] Lorente, N. & Persson, M. Theory of single molecule vibrational spectroscopy and microscopy. *Physical Review Letters* **85**, 2997–3000 (2000).

[39] Dudko, O. K., Hummer, G. & Szabo, A. Theory, analysis, and interpretation of single-molecule force spectroscopy experiments. *Proceedings of the National Academy of Sciences of the United States of America* **105**, 15755–15760 (2008).

[40] Galperin, M., Ratner, M. A., Nitzan, A. & Troisi, A. Nuclear coupling and polarization in molecular transport junctions: Beyond tunneling to function. *Science* **319**, 1056–1060 (2008).

[41] Osorio, E. *et al.* Addition energies and vibrational fine structure measured in electromigrated single-molecule junctions based on an oligophenylenevinylene derivative. *Advanced Materials* **19**, 281–285 (2007).

[42] Park, J. *et al.* Coulomb blockade and the Kondo effect in single-atom transistors. *Nature* **417**, 722–725 (2002).

[43] Stipe, B. C., Rezaei, M. A. & Ho, W. Single-molecule vibrational spectroscopy and microscopy. *Science* **280**, 1732–1735 (1998).

[44] Yang, H. *et al.* Protein conformational dynamics probed by single-molecule electron transfer. *Science* **302**, 262–266 (2003).

[45] Holman, M. W., Liu, R. & Adams, D. M. Single-molecule spectroscopy of interfacial electron transfer. *Journal of the American Chemical Society* **125**, 12649–12654 (2003).

[46] Bi, H. *Raman Spectroscopy on Single-Molecule Junctions.* Dissertation, Technische Universität München, München (2014).

[47] Gerster, D. F. *Light-induced electron motion in nanojunctions.* Dissertation, Technische Universität München, München (2012).

[48] Bi, H. *et al.* Voltage-driven conformational switching in a single-molecule junction (2017). Submitted to JACS.

[49] Bi, H. *et al.* Single molecules in strong optical fields: A variable temperature molecular junction spectroscopy set-up (2017). In preparation.

[50] Hasch, P., Gong, Y., Jing, C., Reichert, J. & Barth, J. V. Negative differential conductance in single-molecule junctions with ferromagnetic electrodes (2017). In preparation.

[51] Hasch, P. *et al.* Strain induced shifts in vibrational frequencies of 1,7-dithiol-7-helicene (2017). In preparation.

[52] Reichert, J. *et al.* Driving current through single organic molecules. *Physical Review Letters* **88**, 176804 (2002).

[53] Zhitenev, N., Meng, H. & Bao, Z. Conductance of small molecular junctions. *Physical Review Letters* **88**, 226801 (2002).

[54] Xiao, X., Xu, B. & Tao, N. J. Measurement of single molecule conductance: Benzenedithiol and benzenedimethanethiol. *Nano Letters* **4**, 267–271 (2004).

[55] Huang, Chen, F., Bennett, P. A. & Tao. Single molecule junctions formed via Au-thiol contact: Stability and breakdown mechanism. *Journal of the American Chemical Society* **129**, 13225–13231 (2007).

[56] Venkataraman, L., Klare, J. E., Nuckolls, C., Hybertsen, M. S. & Steigerwald, M. L. Dependence of single-molecule junction conductance on molecular conformation. *Nature* **442**, 904–907 (2006).

[57] Lörtscher, E., Weber, H. B. & Riel, H. Statistical approach to investigating transport through single molecules. *Physical Review Letters* **98** (2007).

[58] Bhushan, B. *Springer Handbook of Nanotechnology.* Springer Handbook of Nanotechnology (Springer Berlin Heidelberg, 2010).

[59] Chen, F., Li, X., Hihath, J., Huang, Z. & Tao, N. Effect of anchoring groups on single-molecule conductance: Comparative study of thiol-, amine-, and carboxylic-acid-terminated molecules. *Journal of the American Chemical Society* **128**, 15874–15881 (2006).

[60] Hens, Z., Tallapin, D. V., Weller, H. & Vanmaekelbergh, D. Breaking and restoring a molecularly bridged metal|quantum dot junction. *Applied Physics Letters* **81**, 4245–4247 (2002).

[61] Ahn, S. *et al.* Electronic transport and mechanical stability of carboxyl linked single-molecule junctions. *Physical Chemistry Chemical Physics* **14**, 13841 (2012).

[62] Zhou, X.-S., Liang, J.-H., Chen, Z.-B. & Mao, B.-W. An electrochemical jump-to-contact STM-break junction approach to construct single molecular junctions with different metallic electrodes. *Electrochemistry Communications* **13**, 407–410 (2011).

[63] Selzer, Y. & Allara, D. L. Single-molecule electrical junctions. *Annual Review of Physical Chemistry* **57**, 593–623 (2006).

[64] Perrin, M. L. *et al.* Large tunable image-charge effects in single-molecule junctions. *Nature Nanotechnology* **8**, 282–287 (2013).

[65] Tian, J.-H. *et al.* The fabrication and characterization of adjustable nanogaps between gold electrodes on chip for electrical measurement of single molecules. *Nanotechnology* **21**, 274012 (2010).

[66] Du, W. *et al.* On-chip molecular electronic plasmon sources based on self-assembled monolayer tunnel junctions. *Nature Photonics* **10**, 274–280 (2016).

[67] Tsutsui, M. & Taniguchi, M. Single molecule electronics and devices. *Sensors* **12**, 7259–7298 (2012).

[68] Keane, Z. K., Yu, L. H. & Natelson, D. Magnetoresistance of atomic-scale electromigrated nickel nanocontacts. *Applied Physics Letters* **88**, – (2006).

[69] Park, H., Lim, A. K. L., Alivisatos, A. P., Park, J. & McEuen, P. L. Fabrication of metallic electrodes with nanometer separation by electromigration. *Applied Physics Letters* **75**, 301–303 (1999).

[70] Reed, M. A., Zhou, C., Muller, C., Burgin, T. & Tour, J. Conductance of a molecular junction. *Science* **278**, 252–254 (1997).

[71] Nitzan, A. & Ratner, M. A. Electron transport in molecular wire junctions. *Science* **300**, 1384–1389 (2003).

[72] Tian, J.-H. *et al.* Study of molecular junctions with a combined surface-enhanced Raman and mechanically controllable break junction method. *Journal of the American Chemical Society* **128**, 14748–14749 (2006).

[73] Kiguchi, M., Sekiguchi, N. & Murakoshi, K. Electric conductance of metal nanowires at mechanically controllable break junctions under electrochemical potential control. *Surface Science* **601**, 5262–5265 (2007).

[74] Baillin, X., Joachim, C. & Poupon, G. *Nanopackaging: From Nanomaterials to the Atomic Scale: Proceedings of the 1st International Workshop on Nanopackaging, Grenoble 27-28 June 2013*. Advances in Atom and Single Molecule Machines (Springer International Publishing, 2015).

[75] Xu, B. & Tao, N. J. Measurement of single-molecule resistance by repeated formation of molecular junctions. *Science* **301**, 1221–1223 (2003).

[76] Xiao, X., Xu, B. & Tao, N. Conductance titration of single-peptide molecules. *Journal of the American Chemical Society* **126**, 5370–5371 (2004).

[77] Tao, N. J. Electron transport in molecular junctions. *Nature Nanotechnology* **1**, 173–181 (2006).

[78] Joachim, C., Gimzewski, J., Aviram, A. *et al.* Electronics using hybrid-molecular and mono-molecular devices. *Nature* **408**, 541–548 (2000).

[79] Drude, P. Zur Elektronentheorie der Metalle. *Annalen der Physik* **306**, 566–613 (1900).

[80] Landauer, R. Can a length of perfect conductor have a resistance? *Physics Letters A* **85**, 91–93 (1981).

[81] Homoth, J. *et al.* Electronic transport on the nanoscale: Ballistic transmission and Ohm′s law. *Nano Letters* **9**, 1588–1592 (2009).

[82] Bergmann, L., Schaefer, C., Kassing, R. & Blügel, S. *Lehrbuch der Experimentalphysik 6. Festkörper*. Lehrbuch Der Experimentalphysik (de Gruyter, 2005).

[83] Butcher, P., March, N. & Tosi, M. *Physics of Low-Dimensional Semiconductor Structures.* Physics of Solids and Liquids (Springer US, 2013).

[84] Gross, R. & Marx, A. *Festkörperphysik* (Oldenbourg Wissenschaftsverlag, 2012).

[85] Ohnishi, H., Kondo, Y. & Takayanagi, K. Quantized conductance through individual rows of suspended gold atoms. *Nature* **395**, 780–783 (1998).

[86] Hornyak, G., Tibbals, H., Dutta, J. & Moore, J. *Introduction to Nanoscience and Nanotechnology* (CRC Press, 2008).

[87] Di Ventra, M., Pantelides, S. & Lang, N. First-principles calculation of transport properties of a molecular device. *Physical Review Letters* **84**, 979–982 (2000).

[88] Joachim, C. & Ratner, M. Molecular wires: Guiding the super-exchange interactions between two electrodes. *Nanotechnology* **15**, 1065 (2004).

[89] Berlin, Y. A. & Ratner, M. A. Intra-molecular electron transfer and electric conductance via sequential hopping: Unified theoretical description. *Radiation Physics and Chemistry* **74**, 124–131 (2005).

[90] Petrov, E., Shevchenko, Y. V. & May, V. On the length dependence of bridge-mediated electron transfer reactions. *Chemical Physics* **288**, 269–279 (2003).

[91] Akkerman, H. B. & de Boer, B. Electrical conduction through single molecules and self-assembled monolayers. *Journal of Physics: Condensed Matter* **20**, 013001 (2007).

[92] Joachim, C. & Ratner, M. A. Molecular electronics: Some views on transport junctions and beyond. *Proceedings of the National Academy of Sciences of the United States of America* **102**, 8801–8808 (2005).

[93] Sato, T. & Ahmed, H. Observation of a coulomb staircase in electron transport through a molecularly linked chain of gold colloidal particles. *Applied Physics Letters* **70**, 2759–2761 (1997).

[94] Mangold, M. A., Calame, M., Mayor, M. & Holleitner, A. W. Negative differential photoconductance in gold nanoparticle arrays in the coulomb blockade regime. *ACS Nano* **6**, 4181–4189 (2012).

[95] Raman, C. V. & Krishnan, K. S. A new type of secondary radiation. *Nature* **121**, 501–502 (1928).

[96] Smith, E. & Dent, G. *Modern Raman spectroscopy: A practical approach* (John Wiley & Sons, 2013).

[97] Tkachenko, N. *Optical Spectroscopy: Methods and Instrumentations* (Elsevier Science, 2006).

[98] Günzler, H. & Gremlich, H. *IR-Spektroskopie: Eine Einführung* (Wiley, 2012).

[99] Larkin, P. *Infrared and Raman Spectroscopy: Principles and Spectral Interpretation* (Elsevier Science, 2011).

[100] Kneipp, K. & Kneipp, H. Single molecule raman scattering. *Appl. Spectrosc.* **60**, 322A–334A (2006).

[101] Nie, S. & Emory, S. R. Probing single molecules and single nanoparticles by surface-enhanced raman scattering. *Science* **275**, 1102–1106 (1997).

[102] Kneipp, K. *et al.* Single molecule detection using surface-enhanced raman scattering (SERS). *Physical Review Letters* **78**, 1667–1670 (1997).

[103] Zhang, W., Yeo, B. S., Schmid, T. & Zenobi, R. Single molecule tip-enhanced raman spectroscopy with silver tips. *The Journal of Physical Chemistry C* **111**, 1733–1738 (2007).

[104] Benson, O. Assembly of hybrid photonic architectures from nanophotonic constituents. *Nature* **480**, 193–199 (2011).

[105] Willets, K. A. & Van Duyne, R. P. Localized surface plasmon resonance spectroscopy and sensing. *Annual Review of Physical Chemistry* **58**, 267–297 (2007).

[106] Courjon, D. & Bainier, C. *Near field microscopy and near field optics*, vol. 57 of *10* (IOP Publishing, 1999).

[107] Pettinger, B., Ren, B., Picardi, G., Schuster, R. & Ertl, G. Tip-enhanced Raman spectroscopy (TERS) of malachite green isothiocyanate at Au (111): Bleaching behavior under the influence of high electromagnetic fields. *Journal of Raman Spectroscopy* **36**, 541–550 (2005).

[108] Calafiore, G. *et al.* Campanile near-field probes fabricated by nanoimprint lithography on the facet of an optical fiber. *Scientific Reports* **7** (2017).

[109] Zhang, J., Zhang, L. & Xu, W. Surface plasmon polaritons: physics and applications. *Journal of Physics D: Applied Physics* **45**, 113001 (2012).

[110] Fischer, U. C. *The Tetrahedral Tip as a Probe for Scanning Near-Field Optical Microscopy*, 255–262 (Springer Netherlands, Dordrecht, 1993).

[111] Tanaka, K., Burr, G. W., Grosjean, T., Maletzky, T. & Fischer, U. C. Superfocussing in a metal-coated tetrahedral tip by dimensional reduction of surface-to edge-plasmon modes. *Applied Physics B* **93**, 257–266 (2008).

[112] Hohenberg, P. & Kohn, W. Inhomogeneous electron gas. *Physical Review* **136**, B864–B871 (1964).

[113] Kohn, W. & Sham, L. J. Self-consistent equations including exchange and correlation effects. *Physical Review* **140**, A1133–A1138 (1965).

[114] Gong, Y. *Electron-Phonon Interaction in Current Driven Single Molecule Junctions.* Master's thesis, Technische Universität München, München (2013).

[115] Frisch, M. J. *et al.* Gaussian∼09 Revision A.02. Gaussian Inc. Wallingford CT 2009.

[116] Lee, C., Yang, W. & Parr, R. G. Development of the Colle-Salvetti correlation-energy formula into a functional of the electron density. *Physical Review B* **37**, 785–789 (1988).

[117] Vosko, S. H., Wilk, L. & Nusair, M. Accurate spin-dependent electron liquid correlation energies for local spin density calculations: A critical analysis. *Canadian Journal of Physics* **58**, 1200–1211 (1980).

[118] Frisch, M. J. *et al.* Gaussian 09 users reference (2009). Gaussian Inc. Wallingford CT 2009.

[119] Harsha, P. *Principles of Vapor Deposition of Thin Films* (Elsevier Science, 2005).

[120] Love, J. C., Estroff, L. A., Kriebel, J. K., Nuzzo, R. G. & Whitesides, G. M. Self-assembled monolayers of thiolates on metals as a form of nanotechnology. *Chemical Reviews* **105**, 1103–1170 (2005).

[121] Tour, J. M. *et al.* Self-assembled monolayers and multilayers of conjugated thiols, α, ω-dithiols, and thioacetyl-containing adsorbates. Understanding attachments between potential molecular wires and gold surfaces. *Journal of the American Chemical Society* **117**, 9529–9534 (1995).

[122] Reed, M. & Kirk, W. *Nanostructure Physics and Fabrication: Proceedings of the International Symposium, College Station, Texas, March 13*b115, 1989.* (Elsevier Science, 2012).

[123] Ulman, A. *An Introduction to Ultrathin Organic Films: From Langmuir–Blodgett to Self–Assembly* (Elsevier Science, 2013).

[124] Sabatani, E., Cohen-Boulakia, J., Bruening, M. & Rubinstein, I. Thioaromatic monolayers on gold: a new family of self-assembling monolayers. *Langmuir* **9**, 2974–2981 (1993).

[125] Hara, M., Sasabe, H., Yamada, A. & Garito, A. F. Epitaxial growth of organic thin films by organic molecular beam epitaxy. *Japanese Journal of Applied Physics* **28**, L306 (1989).

[126] Forrest, S. R. Ultrathin organic films grown by organic molecular beam deposition and related techniques. *Chemical Reviews* **97**, 1793–1896 (1997).

[127] Schreiber, F. Organic molecular beam deposition: Growth studies beyond the first monolayer. *Physica Status Solidi (A)* **201**, 1037–1054 (2004).

[128] Kowarik, S. *et al.* Real-time observation of structural and orientational transitions during growth of organic thin films. *Physical Review Letters* **96**, 125504 (2006).

[129] Hüfner, S. *Photoelectron Spectroscopy: Principles and Applications.* Springer Series in Solid-State Sciences (Springer Berlin Heidelberg, 2013).

[130] van der Heide, P. *X-ray Photoelectron Spectroscopy: An introduction to Principles and Practices* (Wiley, 2011).

[131] Moulder, J. F. *et al. Handbook of X-ray Photoelectron Spectroscopy* (Physical Electronics Inc., 1992).

[132] Hollas, J. M. *Moderne Methoden in der Spektroskopie* (Springer, 1995).

[133] Ertl, G. & Küppers, J. *Low Energy Electrons and Surface Chemistry* (VCH, 1985).

[134] Perkins, C. L. Molecular anchors for self-assembled monolayers on ZnO: A direct comparison of the thiol and phosphonic acid moieties. *The Journal of Physical Chemistry C* **113**, 18276–18286 (2009).

[135] Betzig, E., Trautman, J. K. *et al.* Near-field optics: Microscopy, spectroscopy and surface modification beyond the diffraction limit. *Science* **257**, 189 (1992).

[136] Girard, C. & Dereux, A. Near-field optics theories. *Reports on Progress in Physics* **59**, 657 (1999).

[137] Heimel, J., Fischer, U. & Fuchs, H. SNOM/STM using a tetrahedral tip and a sensitive current-to-voltage converter. *Journal of Microscopy* **202**, 53–59 (2001).

[138] Lewis, A., Isaacson, M., Harootunian, A. & Muray, A. Development of a 50 nm spatial resolution light microscope: I. light is efficiently transmitted through $\lambda/16$ diameter apertures. *Ultramicroscopy* **13**, 227–231 (1984).

[139] Pohl, D., Denk, W. & Lanz, M. Optical stethoscopy: Image recording with resolution $\lambda/20$. *Applied Physics Letters* **44**, 651–653 (1984).

[140] Ramos, R. & Gordon, M. Reflection-mode, confocal, tip-enhanced Raman spectroscopy system for scanning chemical microscopy of surfaces. *Review of Scientific Instruments* **83**, 093706–093706 (2012).

[141] Ren, B., Picardi, G. & Pettinger, B. Preparation of gold tips suitable for tip-enhanced Raman spectroscopy and light emission by electrochemical etching. *Review of Scientific Instruments* **75**, 837–841 (2004).

[142] Steidtner, J. & Pettinger, B. Tip-enhanced Raman spectroscopy and microscopy on single dye molecules with 15 nm resolution. *Physical Review Letters* **100**, 236101 (2008).

[143] Yeo, B.-S., Stadler, J., Schmid, T., Zenobi, R. & Zhang, W. Tip-enhanced Raman spectroscopy: Its status, challenges and future directions. *Chemical Physics Letters* **472**, 1–13 (2009).

[144] Domke, K. F. & Dai Zhang, B., and Pettinger. Enhanced Raman spectroscopy: Single molecules or carbon? *The Journal of Physical Chemistry C* **111**, 8611–8616 (2007).

[145] Pettinger, B., Ren, B., Picardi, G., Schuster, R. & Ertl, G. Nanoscale probing of adsorbed species by tip-enhanced Raman spectroscopy. *Physical Review Letters* **92** (2004).

[146] Lee, S. *et al.* Fast and sensitive trace analysis of malachite green using a surface-enhanced Raman microfluidic sensor. *Analytica Chimica Acta* **590**, 139–144 (2007).

[147] Chesnoy, J. & Mokhtari, A. Resonant impulsive-stimulated Raman scattering on malachite green. *Physical Review A* **38**, 3566–3576 (1988).

[148] Berlin, Y. A., Burin, A. L. & Ratner, M. A. Charge hopping in DNA. *Journal of the American Chemical Society* **123**, 260–268 (2001).

[149] Burin, A. L. & Ratner, M. A. Charge injection into disordered molecular films. *Journal of Polymer Science Part B: Polymer Physics* **41**, 2601–2621 (2003).

[150] Cui, X. *et al.* Reproducible measurement of single-molecule conductivity. *Science* **294**, 571–574 (2001).

[151] Datta, S. Electrical resistance: An atomistic view. *Nanotechnology* **15**, S433–S451 (2004).

[152] Frank, S., Poncharal, P., Wang, Z. & de Heer, W. A. Carbon nanotube quantum resistors. *Science* **280**, 1744–1746 (1998).

[153] Gerster, D. *et al.* Photocurrent of a single photosynthetic protein. *Nature Nanotechnology* **7**, 673–676 (2012).

[154] Lam, H. Y. & Natelson, D. Transport in single-molecule transistors: Kondo physics and negative differential resistance. *Nanotechnology* **15**, S517 (2004).

[155] Lang, N. & Avouris, P. Electrical conductance of individual molecules. *Physical Review B* **64**, 125323 (2001).

[156] Lindsay, S. M. & Ratner, M. A. Molecular transport junctions: Clearing mists. *Advanced Materials* **19**, 23–31 (2007).

[157] Nitzan, A. Electron transmission through molecules and molecular interfaces. *Annual Review of Physical Chemistry* **52**, 681–694 (2001).

[158] de Silva, Prasanna, A. & Uchiyama, S. Molecular logic and computing. *Nature Nanotechnology* **2**, 399–410 (2007).

[159] Ruben, M. *et al.* Charge transport through a cardan-joint molecule. *Small* **4**, 2229–2235 (2008).

[160] Bi, H. *et al.* Vibrational excitations in current-driven single molecule junctions (2017). Accepted by JACS.

[161] Ordal, M. *et al.* Optical properties of the metals Al, Co, Cu, Au, Fe, Pb, Ni, Pd, Pt, Ag, Ti, and W in the infrared and far infrared. *Applied Optics* **22**, 1099–1119 (1983).

[162] Pasupathy, A. N. *et al.* The Kondo effect in the presence of ferromagnetism. *Science* **306**, 86–89 (2004).

[163] Schuster, G. B. Long-range charge transfer in DNA: transient structural distortions control the distance dependence. *Accounts of Chemical Research* **33**, 253–260 (2000).

[164] Shulaker, M. M. *et al.* Carbon nanotube computer. *Nature* **501**, 526–530 (2013).

[165] Smit, R. *et al.* Measurement of the conductance of a hydrogen molecule. *Nature* **419**, 906–909 (2002).

[166] Céspedes, O. *et al.* I-V asymmetry and magnetoresistance in nickel nanoconstrictions. *Journal of Magnetism and Magnetic Materials* **272-276, Part 2**, 1571 – 1572 (2004).

[167] Hobbs, P. C. D., Laibowitz, R. B. & Libsch, F. R. Ni–NiO–Ni tunnel junctions for terahertz and infrared detection. *Appied Optics* **44**, 6813–6822 (2005).

[168] Moodera, J. S., Kinder, L. R., Wong, T. M. & Meservey, R. Large magnetoresistance at room temperature in ferromagnetic thin film tunnel junctions. *Physical Review Letters* **74**, 3273–3276 (1995).

[169] Makrlík, E. *et al.* Experimental and theoretical study on cation-π interaction of the univalent silver cation with [7]helicene in the gas phase and in the solid state. *Chemical Physics Letters* **635**, 355 – 359 (2015).

[170] Kampshoff, E., Hahn, E. & Kern, K. Correlation between surface stress and the vibrational shift of CO chemisorbed on cu surfaces. *Physical Review Letters* **73**, 704–707 (1994).

[171] Mitra, V. K., Risen, W. M. & Baughman, R. H. A laser Raman study of the stress dependence of vibrational frequencies of a monocrystalline polydiacetylene. *The Journal of Chemical Physics* **66**, 2731–2736 (1977).

[172] Wool, R. P. Mechanisms of frequency shifting in the infrared spectrum of stressed polymer. *Journal of Polymer Science: Polymer Physics Edition* **13**, 1795–1808 (1975).

[173] Huang, Xu, Chen, Ventra, M. D. & Tao. Measurement of current-induced local heating in a single molecule junction. *Nano Letters* **6**, 1240–1244 (2006).

[174] Krüger, D., Rousseau, R., Fuchs, H. & Marx, D. Towards "mechanochemistry": Mechanically induced isomerizations of thiolate-gold clusters. *Angewandte Chemie International Edition* **42**, 2251–2253 (2003).

[175] Rubio, G., Agraït, N. & Vieira, S. Atomic-sized metallic contacts: Mechanical properties and electronic transport. *Physical Review Letters* **76**, 2302–2305 (1996).

[176] van Ruitenbeek, J. M. *et al.* Adjustable nanofabricated atomic size contacts. *Review of Scientific Instruments* **67**, 108–111 (1996).

[177] Yanson, A., Bollinger, G. R., Van den Brom, H., Agrait, N. & Van Ruitenbeek, J. Formation and manipulation of a metallic wire of single gold atoms. *Nature* **395**, 783–785 (1998).

[178] Hutchison, G. & Quan, X., Flexible molecular piezoelectric device, USA patentus 2014/0 375 172, Dec. 25, 2014.

[179] Quan, X., Marvin, C. W., Seebald, L. & Hutchison, G. R. Single-molecule piezoelectric deformation: Rational design from first-principles calculations. *The Journal of Physical Chemistry C* **117**, 16783–16790 (2013).

[180] Oshima, H. & Miyano, K. Spin-dependent conductance quantization in nickel point contacts. *Applied Physics Letters* **73**, 2203–2205 (1998).

[181] Shang, C. H., Berera, G. P. & Moodera, J. S. Exchange-biased ferromagnetic tunnel junctions via reactive evaporation of nickel oxide films. *Applied Physics Letters* **72**, 605–607 (1998).

[182] Sullivan, M. R., Boehm, D. A., Ateya, D. A., Hua, S. Z. & Chopra, H. D. Ballistic magnetoresistance in nickel single-atom conductors without magnetostriction. *Physical Review B* **71**, 024412 (2005).

[183] Tedrow, P. M. & Meservey, R. Spin polarization of electrons tunneling from films of Fe, Co, Ni, and Gd. *Physical Review B* **7**, 318–326 (1973).

[184] Rocha, A. R. & Sanvito, S. Asymmetric I-V characteristics and magnetoresistance in magnetic point contacts. *Physical Review B* **70**, 094406 (2004).

[185] Rocha, A. R. & Sanvito, S. Resonant magnetoresistance in organic spin valves (invited). *Journal of Applied Physics* **101**, – (2007).

[186] Rocha, A. R., Archer, T. & Sanvito, S. Search for magnetoresistance in excess of 1000% in Ni point contacts: Density functional calculations. *Physical Review B* **76**, 054435 (2007).

[187] Qu, Q. *et al.* Chemically binding carboxylic acids onto TiO_2 nanoparticles with adjustable coverage by solvothermal strategy. *Langmuir* **26**, 9539–9546 (2010).

[188] Yu, F. *et al.* Various crystal structures based on 4,4'-(diethynylanthracene-9,10-diyl) dibenzoic acid: from 0D dimer to 3D net framework. *CrystEngComm* **15**, 8273–8279 (2013).

[189] Kwan, Y. C. G., Ng, G. M. & Huan, C. H. A. Identification of functional groups and determination of carboxyl formation temperature in graphene oxide using the XPS O1s spectrum. *Thin Solid Films* **590**, 40 – 48 (2015).

[190] Stearns, M. B. Simple explanation of tunneling spin-polarization of Fe, Co, Ni and its alloys. *Journal of Magnetism and Magnetic Materials* **5**, 167–171 (1977).

[191] Eastman, D. E., Himpsel, F. J. & Knapp, J. A. Experimental band structure and temperature-dependent magnetic exchange splitting of nickel using angle-resolved photoemission. *Physical Review Letters* **40**, 1514–1517 (1978).

[192] Koster, G. F. Density of states curve for nickel. *Physical Review* **98**, 901–902 (1955).

[193] Sanvito, S. Molecular spintronics. *Chemical Society Reviews* **40**, 3336–3355 (2011).

[194] Naaman, R. & Waldeck, D. H. Chiral-induced spin selectivity effect. *The Journal of Physical Chemistry Letters* **3**, 2178–2187 (2012).

[195] Bogani, L. & Wernsdorfer, W. Molecular spintronics using single-molecule magnets. *Nature Materials* **7**, 179–186 (2008).

[196] Roblin, P. & Rohdin, H. *High-Speed Heterostructure Devices: From Device Concepts to Circuit Modeling* (Cambridge University Press, 2002).

[197] Takatsu, M., Logic circuit using element having negative differential conductance, USA patentus 5,153,461, Oct. 6, 1992.

[198] Linn, E., Rosezin, R., Kügeler, C. & Waser, R. Complementary resistive switches for passive nanocrossbar memories. *Nature Materials* **9**, 403–406 (2010).

[199] Xue, Y. *et al.* Negative differential resistance in the scanning-tunneling spectroscopy of organic molecules. *Physical Review B* **59**, R7852–R7855 (1999).

[200] Perrin, M. L. *et al.* Large negative differential conductance in single-molecule break junctions. *Nat Nano* **9**, 830–834 (2014).

[201] Heersche, H. B. *et al.* Electron transport through single mn_{12} molecular magnets. *Physical Review Letters* **96**, 206801 (2006).

[202] Tu, X. W., Mikaelian, G. & Ho, W. Controlling single-molecule negative differential resistance in a double-barrier tunnel junction. *Physical Review Letters* **100**, 126807 (2008).

[203] Chen, J., Reed, M. A., Rawlett, A. M. & Tour, J. M. Large on-off ratios and negative differential resistance in a molecular electronic device. *Science* **286**, 1550–1552 (1999).

[204] Chen, J. *et al.* Room-temperature negative differential resistance in nanoscale molecular junctions. *Applied Physics Letters* **77**, 1224–1226 (2000).

[205] Zazunov, A., Feinberg, D. & Martin, T. Phonon-mediated negative differential conductance in molecular quantum dots. *Physical Review B* **73**, 115405 (2006).

[206] Thielmann, A., Hettler, M. H., König, J. & Schön, G. Super-poissonian noise, negative differential conductance, and relaxation effects in transport through molecules, quantum dots, and nanotubes. *Physical Review B* **71**, 045341 (2005).

[207] Halbritter, A., Makk, P., Csonka, S. & Mihály, G. Huge negative differential conductance in Au−h_2 molecular nanojunctions. *Physical Review B* **77**, 075402 (2008).

[208] Koga, J. & Toriumi, A. Negative differential conductance at room temperature in three-terminal silicon surface junction tunneling device. *Applied Physics Letters* **70**, 2138–2140 (1997).

[209] Pop, E. *et al.* Negative differential conductance and hot phonons in suspended nanotube molecular wires. *Physical Review Letters* **95**, 155505 (2005).

[210] Tsuchiya, M., Sakaki, H. & Yoshino, J. Room temperature observation of differential negative resistance in an alas/gaas/alas resonant tunneling diode. *Japanese Journal of Applied Physics* **24**, L466 (1985).

[211] Elste, F. & Timm, C. Transport through anisotropic magnetic molecules with partially ferromagnetic leads: Spin-charge conversion and negative differential conductance. *Physical Review B* **73**, 235305 (2006).

[212] Xie, H., Wang, Q., Xue, H.-B., Jiao, H. & Liang, J.-Q. Intrinsic spin-relaxation induced negative tunnel magnetoresistance in a single-molecule magnet. *Journal of Applied Physics* **113**, 213708 (2013).

[213] Wei, L., Rui-Qiang, W., Liang-Bin, H. & Mou, Y. Spin-dependent negative differential conductance in transport through single-molecule magnets. *Chinese Physics B* **22**, 047201 (2013).

[214] Blobner, F. *et al.* Thiolate-bonded self-assembled monolayers on Ni(111): Bonding strength, structure, and stability. *The Journal of Physical Chemistry C* **119**, 15455–15468 (2015).

[215] Mekhalif, Z., Laffineur, F., Couturier, N. & Delhalle, J. Elaboration of self-assembled monolayers of n -alkanethiols on nickel polycrystalline substrates: Time, concentration, and solvent effects. *Langmuir* **19**, 637–645 (2003).

[216] Mekhalif, Z., Lazarescu, A., Hevesi, L., Pireaux, J.-J. & Delhalle, J. Self-assembled monolayers of n-hexanethiol and 6-[2',5'-di(2"-thienyl)pyrrol-1'-yl]hexanethiol on polycrystalline nickel substrates. *Journal of Materials Chemistry* **8**, 545–551 (1998).

[217] Fontanesi, C. *et al.* New one-step thiol functionalization procedure for ni by self-assembled monolayers. *Langmuir* **31**, 3546–3552 (2015).

[218] Hoertz, P. G., Niskala, J. R., Dai, P., Black, H. T. & You, W. Comprehensive investigation of self-assembled monolayer formation on ferromagnetic thin film surfaces. *Journal of the American Chemical Society* **130**, 9763–9772 (2008).

[219] Han, R. *et al.* Toward interfacing organic semiconductors with ferromagnetic transition metal substrates: enhanced stability via carboxylate anchoring. *Chemical Communication* **52**, 9805–9808 (2016).

[220] Johansson, E. & Nyborg, L. XPS study of carboxylic acid layers on oxidized metals with reference to particulate materials. *Surface and Interface Analysis* **35**, 375–381 (2003).

[221] Wang, Z., Chan, C. T., Zhang, W., Ming, N. & Sheng, P. Three-dimensional self-assembly of metal nanoparticles: Possible photonic crystal with a complete gap below the plasma frequency. *Physical Review B* **64** (2001).

[222] Räther, H. *Surface plasmons on smooth surfaces* (Springer, 1988).

[223] Islam, M. S., Kouzani, A. Z., Dai, X. J. & Michalski, W. P. Parameter sensitivity analysis of surface plasmon resonance biosensor through numerical simulation. In *IEEE/ICME International Conference on Complex Medical Engineering*, 171–176 (2010).

[224] Chen, C. *Introduction to Scanning Tunneling Microscopy.* Oxford series in optical and imaging sciences (Oxford University Press, 1993).

[225] Salomon, A. *et al.* Comparison of electronic transport measurements on organic molecules. *Advanced Materials* **15**, 1881–1890 (2003).

[226] Demtröder, W. *Experimentalphysik 3: Atome, Moleküle und Festkörper.* Springer-Lehrbuch (Springer Berlin Heidelberg, 2010).

[227] Emberly, E. G. & Kirczenow, G. Molecular spintronics: spin-dependent electron transport in molecular wires. *Chemical Physics* **281**, 311 – 324 (2002).

[228] Yagi, S., Kawamori, M. & Matsubara, E. Electrochemical study on the synthesis process of Co–Ni alloy nanoparticles via electroless deposition. *Journal of The Electrochemical Society* **157**, E92 (2010).

[229] Rocha, A. R. *et al.* Towards molecular spintronics. *Nature Materials* **4**, 335–339 (2005).

[230] Bernien, M. *et al.* Tailoring the nature of magnetic coupling of Fe-porphyrin molecules to ferromagnetic substrates. *Physical Review Letters* **102**, 047202 (2009).

[231] Kollmar, C. & Kahn, O. Ferromagnetic spin alignment in molecular systems: An orbital approach. *Accounts of Chemical Research* **26**, 259–265 (1993).

[232] Christou, G., Gatteschi, D., Hendrickson, D. N. & Sessoli, R. Single-molecule magnets. *MRS Bulletin* **25**, 66–71 (2000).

[233] Wende, H. *et al.* Substrate-induced magnetic ordering and switching of iron porphyrin molecules. *Nature Materials* **6**, 516–520 (2007).

[234] Pauli, W. Über den zusammenhang des abschlusses der elektronengruppen im atom mit der komplexstruktur der spektren. *Zeitschrift für Physik* **31**, 765–783 (1925).

[235] Pati, R., Senapati, L., Ajayan, P. M. & Nayak, S. K. First-principles calculations of spin-polarized electron transport in a molecular wire: Molecular spin valve. *Physical Review B* **68**, 100407 (2003).

List of Figures

List of Acronyms

ADC Analog Digital Converter

AFM Atomic Force Microscopy

CCD Charge-Coupled Device

CVD Chemical Vapor Deposition

DAC Digital Analog Converter

DFT Density Functional Theory

DHE 1,7-dithiol-7-helicene

EBPVD Electron Beam Physical Vapor Deposition

EDA 4,4'-(1,2-ethynediyl)dibenzoic acid

FWHM Full Width Half Maximum

GMR Giant Magneto Resistance

GPIB General Purpose Interface Bus

HDD Hard Disk Drive

HF High Frequency

HOMO Highest Occupied Molecular Orbital

HV High Voltage

HWHM Half Width Half Maximum

IPT InterPhenyl Torsion angle

I-d Current-Distance

I-V Current-Voltage

LUMO Lowest Unoccupied Molecular Orbital

LT Low Temperature

MCBJ Mechanically Controlled Break Junction

MGIC Malachite Green IsoCyanate

MJS Molecular Junction Spectroscopy

ML Monolayer

NDC Negative Differential Conductance

NDL Negative Differentielle Leitfähigkeit

NA Numerical Aperture

PC Personal Computer

PLC Power Line Cycle

PVD Physical Vapor Deposition

RT Room Temperature

SAM Self Assembled Monolayer

SERS Surface Enhanced Raman Spectroscopy

SNOM Scanning Nearfield Optical Microscopy

SP Surface Plasmon

SPM Scanning Probe Microscopy

SPS Scanning Probe Spectroscopy

SPP Surface Plasmon Polariton

T-Tip Tetrahedral-Tip

TERS Tip Enhanced Raman Spectroscopy

THF TetraHydroFuran

TMR Tunneling Magneto Resistance

TM-TPD [2,2',2",5'-tetramethyl-[1,1':4',1"-terphenyl]-4,4"-dithiol]

TPD [1,1':4',1"-terphenyl]-4,4"-dithiol]

TSP Titanium Sublimation Pump

UHV Ultra High Vacuum

UPS Ultraviolet Photoelectron Spectroscopy

XPS X-ray Photoelectron Spectroscopy

Acknowledgements

Am Ende meiner Arbeit möchte ich gerne einigen Personen, die meinen Weg am E20 begleitet haben und mich unterstützt haben danken.

Zuerst danke ich **Prof. Dr. Johannes V. Barth** für die Chance meine Dissertation in seiner Arbeitsgruppe durchzuführen. Das Arbeitsklima war zu jeder Zeit hervorragend und inspirierend. Es war mir eine Ehre.
Weiterhin hat mich **Dr. Joachim Reichert** durchgehend mit viel Geduld und experimenteller Expertise betreut. Zudem waren die gemeinsamen Mittagessen, bei denen wir stets über die weitergehenden Experimente diskutiert haben, eine Konstante während meiner Zeit am E20. Ich wünsche dir weiterhin viel Erfolg und ein glückliches Händchen für deine Forschungen und deinen Lebensweg.

Hai Bi hat mich exzellent in das MJS Experiment eingelernt und wir hatten während unserer Kaffeepausen bei Gesprächen über Physik, Politik und Fußball viel Spaß.
Einen wesentlichen Teil zu meiner Arbeit hat **Yuxiang Gong** beigetragen. Die Simulationen, die professionellen Auswerttools sowie die experimentelle Hilfe haben mir das Forschen sehr erleichtert. Das tägliche gemeinsame Kaffeetrinken hat mir stets geholfen das Nachmittagstief erfolgreich zu überwinden. Unsere Diskussionen über weitere Experimente, physikalische Prinzipien, Technik und Autos haben mich bei meiner Dissertation und auch persönlich bereichert. Der gemeinsame Besuch der DPG-Tagung in Dresden ist und bleibt ein unvergessliches Erlebnis.

Großer Dank gebührt dem Universalgelehrten des Lehrstuhls **Dr. Hartmut Schlichting**, welcher zu jedem Thema eine dezidierte und fundierte Meinung hat. Deine permanente Bereitschaft mir mit einem guten Rat zur Seite zu stehen hat mir sehr geholfen. Dabei hast du mich bei meiner Dissertation sehr unterstützt aber auch im privaten Bereich hast du mir sehr weitergeholfen mit deinen Erfahrungen. Ich hoffe, du bleibst bei guter Gesundheit, weit über deine baldige Verrentung hinaus.

Meine Bürokollegen **Yiqi Zhang**, **Peter Weber** und **Rafael Hellwig** haben eine durchgehend lockere und sehr produktive Arbeitsatmosphäre geschaffen. Eure aufbauenden Worte und eure Expertise waren sehr wertvoll für mich.

Den E20 Kollegen möchte ich für das angenehme und freundschaftliche Klima danken. Allen voran **Karl Kölbl**, aber auch **Reinhold Schneider** und **Karl Eberle** leisten hervorragende Arbeit und waren immer zur Stelle wenn ihre Unterstützung und ihr Beistand benötigt wurde. Deshalb seid ihr für mich das Rückgrat des Lehrstuhls.

Weiterhin haben **Martin Zeitlmair**, **Tobias Saule** und **Dragosh Otto** beim Korrekturlesen dieser Arbeit hervorragende Arbeit geleistet.

Christina, dir gebührt der meiste Dank, du hast mich ausdauernd und andauernd in die richtige Bahn gelenkt und mich auf meinem Weg von Anfang an unterstützt. Deshalb verdanke ich dir diese Dissertation.